ISSN: 2588-5596

JGT

Journal of Gas Technology

Volume 5 . Issue 1 . Summer 2020 . www.jgt.irangi.org

Journal of Gas Technology, JGT

Volume 5, Issue 1, Summer 2020

Publisher
Iranian Gas Institute

Contact Information
http://jgt.irangi.org
Email: ijgt.igi@gmail.com

EISSN: 2588-5596

Open Access Journal
Journal of Gas Technology is a peer reviewed, open access journal.

Table of Contents

JOURNAL OF GAS TECHNOLOGY

Volume 5 / Issue 1 / Summer 2020 / Pages 04-21

Journal Homepage: http://jgt.irangi.org

Control Structure Design and Dynamic Simulation of Mixed Fluid Cascade Natural Gas Liquefaction Process

Talieh Ramezani[1], Zahra Nargessi[1], Ali Palizdar[1], Ali Vatani[1*]

1. Institute of Liquefied Natural Gas (I-LNG), School of Chemical Engineering, College of Engineering, University of Tehran, Tehran, Iran

ARTICLE INFO

ORIGINAL RESEARCH ARTICLE

Article History:
Received: 13 February 2020
Revised: 17 May 2020
Accepted: 8 June 2020

Keywords:
LNG
MFC Process
Process Control
Dynamic Simulation

ABSTRACT

Mixed fluid cascade natural gas liquefaction process control system is designed and analyzed in this study. The specific energy consumption (SEC) of this process is 0.2647 kWh/kg LNG. After steady state simulation and sizing the process components, a control structure is designed to control the whole process. In addition, dynamic simulation is carried out and performance of the controllers is investigated. By dynamic simulation, specific energy consumption is reduced to 0.2574 kWh/kg LNG, which means the designed control structure can stably and accurately control the process. To validate the performance and stability of the control structure, changes in the flow rate and temperature of the feed gas are inflicted as a disturbance to the process.

DOR: 20.1001.1.25885596.2020.5.1.1.1

How to cite this article
T. Ramezani, Z. Nargessi, A. Palizdar, A. Vatani. Control Structure Design and Dynamic Simulation of Mixed Fluid Cascade Natural Gas Liquefaction Process. Journal of Gas Technology. 2020; 5(1): 04 -21. (http://www.jgt.irangi.org/article_251656.html)

*Corresponding author.
E-mail address: avatani@ut.ac.ir (A. Vatani)

Available online 20 September 2020

1. Introduction

Over the last five decades the global energy demand has been inclined towards fuels with lower carbon content, e.g. natural gas, due to environmental concerns [1]. Today the share of natural gas in primary energy is about 24% and it is predicted that this share will rise to about 27% by 2040 [1]. Generally, there are various methods for natural gas transportation such as pipelines, liquefied natural gas (LNG), compressed natural gas (CNG) and so on. According to the BP Energy Outlook, it is expected that the share of LNG in the worldwide gas trade will grow from 35% in 2017 to above 46% by 2035, and its share of consumption will increase from 10% to 15% [1]. There are several cryogenic processes available for LNG production that the basis of all them is cooling of natural gas to approximately -162 °C at atmospheric pressure. Thus, natural gas becomes an odorless, colorless and noncorrosive liquid and its volume is reduced by about 600 times [2]. In this paper, the Mixed Fluid Cascade (MFC) process is considered for studying.

In the MFC process, three cascade refrigeration cycles are used. In fact, purified natural gas is precooled, liquefied and subcooled by means of three different mixed refrigerants in these cycles [3]. This technology is capable of producing up to 12 million tons per annum LNG in a single train [4]. Despite the complexity of the MFC process (due to the high number of the required equipment) and high investment costs, this process has higher thermodynamic efficiency, lower energy consumption and higher exergy efficiency compared to the other LNG processes [5].

Generally, the liquefaction processes of natural gas consume considerable amounts of energy, making it crucial for the processes to operate efficiently, reliably and safely [6]. In order to achieve these aims and maximize the profit, these processes should be kept well under control [7] hence necessitating the design of a control structure. The main goals of this study include designing an optimized control structure and perform a dynamic simulation of the MFC process. These studies have not been performed up to now because most of the previous studies on the LNG production processes cover their operation in the steady state. For example, in [5, 8], energy, exergy and advanced exergetic analyses of the five conventional LNG processes were carried out. These analyses were performed by simulation of these processes in steady state mode and their results show that the MFC process has better performance compared to the other LNG processes, i.e. it has lower energy consumption (0.2545 kWh/kg LNG), higher coefficient of performance (4.812 for precooling cycle) and higher exergy efficiency (51.82 %). Only in recent years, dynamic simulation and process control of the common C3MR process have been performed by different groups which reported in the literature [7, 9-11]. Husnil *et* al. (2014) [12] developed a control structure for the MSMR process for a floating LNG plant and optimized the cost function by adjusting the controlled variable, i.e. the flow rate ratio of liquid (heavy) and vapor (light) mixed refrigerant. Also, the dynamic modeling and control structure design of the LNG process patented by SINTEF was carried out by Singh *et* al. [13].

In this work, the MFC process is simulated in steady state mode using a conventional commercial chemical simulator (available from Aspen Technologies Inc.). Then, a control structure is designed and analyzed. Followed, dynamic simulation of the MFC process is carried out to test the proposed control structure.

2. Process Description

The number of refrigeration cycles and the required power in the refrigeration systems are effective parameters in the performance of the liquefaction processes. However increasing the number of cycles improves process efficiency and production capacity, but it increases the fixed costs and process complexity [5]. It increases the operating costs as well. The most economical situation can be achieved when the

process capacity is increased without adding to the number of cycles [5]. In this regard, Linde AG and Statoil introduced a new LNG process, called Mixed Fluid Cascade or MFC process.

(Figure 1) shows the process flow diagram of MFC process. Treated natural gas (NG) enters the process at 13 °C and 60 bar. Through passing four heat exchangers, E-1-A, E-1-B, E-2 and E-3, the natural gas is completely converted to LNG after being pressure relieved to about atmospheric pressure by J-T valve (V-5). As mentioned, three mixed refrigerant cycles are used to supply the required refrigeration. These cycles are discussed in the next sections.

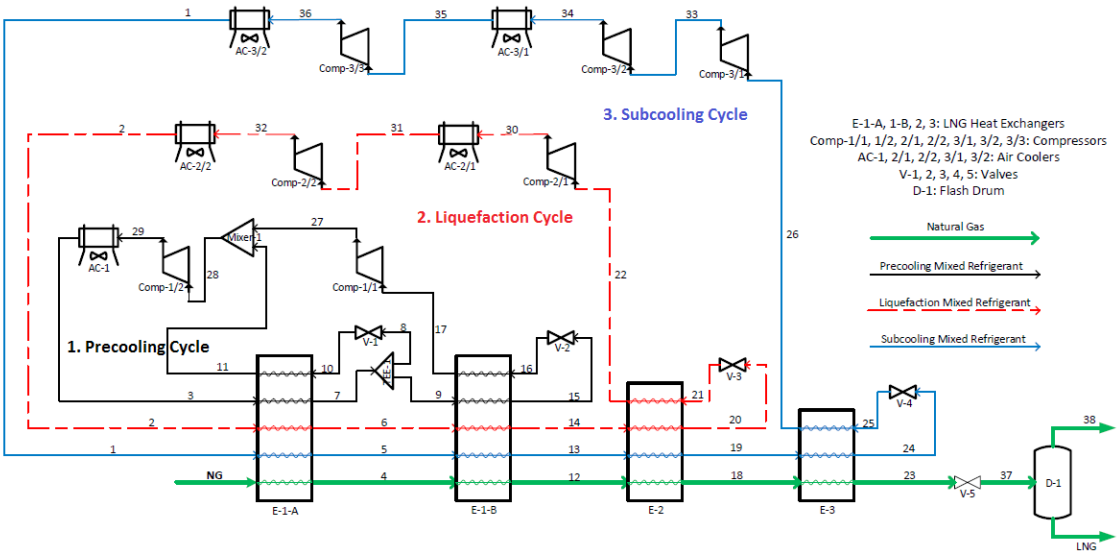

Figure 1: Process flow diagram of MFC process.

2.1. Precooling Cycle

Natural gas enters the precooling cycle (via state points NG⟶4⟶12) and is cooled to approximately the dew point temperature (about -27 °C: stream 12). This cycle consists of two plate fin heat exchangers (PFHEs) (E-1-A and E-1-B) [4]. A mixture of ethylene, ethane, propane and n-butane is used as the mixed refrigerant (MR) in this cycle [8].

The mixed refrigerant (stream 3), after passing through the E-1-A (3⟶7), is divided into two fractions and is used at two pressure levels. Stream 8 enters a J-T valve (V-1) and used as a cooling agent in E-1-A. Another fraction, stream 9, is used in the second heat exchanger, E-1-B, to provide the required cooling. The outlet refrigerant from E-1-B, stream 17, after passing through the Comp-1/1 compressor (17⟶27) is mixed with the outlet refrigerant from E-1-A, stream 11, and follows to another compression section (Comp-1/2: 28⟶29). Next, mixed refrigerant is cooled in an air cooler (AC-1) and re-enters the E-1-A at 36 °C and 16.89 bar (29⟶3).

2.2. Liquefaction Cycle

The liquefaction cycle consists of the E-1-A, E-1-B and E-2 heat exchangers. The E-2 is a spiral wound heat exchanger (SWHE) [4]. The natural gas enters at the dew point temperature and is condensed after leaving E-2 with the temperature of -85.20 °C (12⟶18). In this cycle, the mixed refrigerant (stream 2) is a mixture of methane, ethylene, ethane and propane [8]. The refrigerant is cooled in E-1-A, E-1-B and E-2 before following to V-3 J-T valve and is used again in E-2 but now as a cooling agent (2⟶6⟶14⟶20⟶21⟶22).

The compression of mixed refrigerant is done in two stages (Comp-2/1 & Comp-2/2) with an intermediate air cooler (AC-2/1). The refrigerant is also cooled in another air cooler (AC-2/2) before entering E-1-A. After passing through the compressors and air coolers, the refrigerant operating condition reaches to 36 °C and 27.89 bar (22⟶30⟶31⟶32⟶2).

2.3. Subcooling Cycle

The subcooling cycle consists of E-3 spiral wound heat exchanger in addition to the prenominated heat exchangers [4]. The condensed natural gas is sub-cooled in this heat exchanger and leaves it at -158 °C (18⟶23). The pressure is reduced to atmospheric pressure after passing through V-5 expansion valve. Finally, LNG is produced at -163.4 °C and 1 bar. Here, the mixed refrigerant (stream 1) is a mixture of methane, ethylene and nitrogen [8]. It is cooled in E-1-A, E-1-B, E-2 and E-3 (1⟶5⟶13⟶19⟶24). After following to V-4 expansion valve (24⟶25), the MR (stream 25) is used again in E-3 as a cooling agent. Then it is compressed in the same procedure as the liquefying refrigerant (26⟶33⟶34⟶35⟶36⟶1).

3. Steady State Simulation of MFC Process

3.1. Process Simulation

In this paper, simulation of the entire process is carried out using Aspen HYSYS 7.2 software. Cryogenic processes are somewhat different from the general chemical processes [14]. Some of the characteristics of the cryogenic processes include multi-stream heat exchangers, low temperature, and high operating pressure. For performing thermodynamic calculations and process simulation, an equation of state (EOS) is required. For the cryogenic natural gas processes, PR (Peng-Robinson) and PRSV (Peng-Robinson-Stryjek-Vera) equations of state are suggested [15]. Thermodynamic fluid package of PRSV is used for the simulation in this study. Specifications and operating conditions of feed gas, mixed refrigerants and LNG product that were used as a basis for the simulation model are given in Table 1.

Table 1. (a) Feed gas and mixed refrigerants specifications of MFC process

Stream Name	NG	LNG	1	2	3
	Natural Gas Feed	Liquid Product	Sub cooling Mixed Refrigerant	Liquefaction Mixed Refrigerant	Precooling Mixed Refrigerant
Molar Flow (kmol/h)	25120.00	23653.26	18100.00	25700.00	34390.00
Temperature (°C)	13.00	-163.40	36.00	36.00	36.00
Pressure (bar)	60.00	1.01	33.89	27.89	16.89
Components (mol %)					
CH_4	89.00	89.65	42.45	12.65	0.00
C_2H_6	5.50	5.84	0.00	32.92	0.01
C_2H_4	0.00	0.00	40.24	27.77	11.29
C_3H_8	2.50	2.66	0.00	26.66	73.57
$n\text{-}C_4H_{10}$	1.00	1.06	0.00	0.00	15.13
N_2	2.00	0.79	17.31	0.00	0.00

3.2. Simulation Results

The MFC process is simulated in the steady-state mode and is validated against literature data which can be found in [8]. Tables 2-5 present results of the simulation. These results include performance of the equipment in the process and overall performance of the process.

Table 2. Performance of the heat exchangers of MFC process.

LNG HE Name	Number of Sides	Duty (kW)	Min. Approach Temp. (°C)	LMTD* (°C)
E-1-A	5	100553.99	2.919	4.219
E-1-B	5	73339.21	2.321	3.796
E-2	4	118416.28	2.119	3.342
E-3	3	59060.57	4.254	5.541

* Log Mean Temperature Difference

Table 3. Performance of the air coolers of MFC process.

Air Cooler Name	Number of Fans*	Working Fluid Duty (kW)	Total Mass Air Flow×10^{-7} (kg/h)	Total Fan Power (kW)*	Air Outlet Temp. (°C)
AC -1	51	-164817.11	2.0670	977.991	53.33
AC-2/1	23	-12640.03	0.9689	690.471	29.64
AC-2/1	37	-21112.41	1.5580	1064.946	29.82
AC-3/1	13	-5589.24	0.5486	354.407	28.62
AC-3/2	13	-3919.00	0.5496	355.863	27.53

* These results are obtained from the air coolers simulation with EDR software.

Table 4. Performance of the compressors of MFC process.

Compressor Name	Power Consumed (kW)	Pressure Ratio	Outlet Temp. (°C)
Comp-1/1	9123.90	2.233	36.19
Comp-1/2	27438.88	2.522	78.75
Comp-2/1	32902.32	4.839	64.64
Comp-2/2	14120.01	1.861	78.78
Comp-3/1	16778.12	4.286	5.94
Comp-3/2	10076.55	1.867	62.08
Comp-3/3	3202.66	1.211	53.96

Table 5. Overall performance of MFC process.

Total Power Consumed in Compressors (kW)	113642.44
Total Power Consumed in Air Coolers (kW)	3443.678
Overall Required Power (kW)	117086.118
Mass Flow of LNG Product (kg/h)	429267
Specific Energy Consumption (kWh/kg LNG)	0.2647*

* For calculating of the SEC, energy consumption of the air coolers is neglected because its value is negligible compared to the energy consumption of the compressors.

As can be seen in Table 5, the specific energy consumption or SEC of the process is equal 0.2647 kWh/kg LNG. Here, SEC is defined by the ratio of the total required power (energy) in the process to the mass flow rate of produced LNG:

$$\text{SEC (kWh/kg LNG)} = \frac{\text{total required power in the process (kW)}}{\text{mass flow rate of produced LNG (kg/h)}} \quad (1)$$

Low SEC value means the energy efficiency of the process is high and vice versa. Different values for this index in different processes can be found in the related references [16, 17]. For example, value of the SEC for multi-stage processes should be less than 0.3 kWh/kg LNG [17]. In this study, the specific energy consumption is less than 0.3 kWh/kg LNG which corroborates that the process model simulated is valid when compared to the real world scenario.

The composite curve of the MFC process is illustrated in (Figure 2). Totally a composite curve shows the overall heating and cooling of a process and the quality of thermal design through the process. So (Figure 2) also validates that the process is thermally efficient and the LNG heat exchangers have appropriate performance due to using mixed refrigerants and three refrigeration cycles.

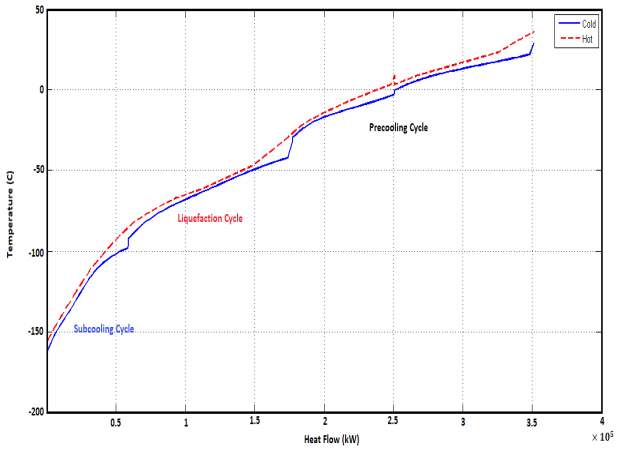

Figure 2: Composite curve of MFC process.

3.3. Equipment Sizing

After static simulation, all components in the process should be sized as it is necessary for entering the dynamic environment of the simulator. The equipment used in the MFC process includes centrifugal compressors, LNG heat exchangers, air coolers, expansion valves and a vertical separator. In following sections, the main equipment (heat exchangers and compressors) and their required sizing parameters are explained. It is worth noting that there is no need to size all of the equipment in detail and only parameters which are required to run the dynamic simulation should be determined.

3.3.1. Heat Exchangers

Multi-stream LNG heat exchangers are the most important equipment of the gas liquefaction processes and are considered as the heart of the process. As mentioned before, PFHEs are used in the precooling cycle and SWHEs are used for liquefaction and subcooling cycles in the MFC process. Since these heat exchangers are proprietary equipment, so sizing information is unavailable in the open literature. Dynamic modeling of such heat exchangers has been discussed for simple processes in a few publications [6, 10, 18].

In this paper, PFHEs and SWHEs are modeled as shell and tube heat exchangers for the purpose of simplification so that the total heat load generated by shell and tube heat exchangers is equal to the heat load of a LNG heat exchanger and the main specifications of the streams are not changed. As a result, there is no change in the overall performance of the MFC process and SEC. Shell and tube heat exchangers have several calculation models that can be used. Generally, the simulator models shell & tube Heat Exchangers based on the following equations (Eqs. 2 & 3) [19]:

$$1)\ \text{Balance Error} = (\dot{m}_{cold}[h_{out}-h_{in}]_{cold}-Q_{leak})-(\dot{m}_{hot}[h_{in}-h_{out}]_{hot}-Q_{loss}) \quad (2)$$

where: $\dot{m}$ = fluid mass flow rate, h = specific enthalpy, Q leak = heat leak (the loss of cold side duty to leakage), Q loss = heat loss (the loss of hot side duty to leakage), Balance Error= a

heat exchanger specification that equals zero for most applications.

$$2)\ Q_{transferred} = U.A.CMTD \quad (3)$$

where Q transferred is the total heat transferred between the tube and shell sides (heat exchanger duty), U is the overall heat transfer coefficient, A is the surface area available for heat transfer, and CMTD is the corrected log mean temperature difference. Here, the EDR-Shell & Tube model is selected for simulation of these heat exchangers and the heat leak and heat loss are neglected. By using this model, the heat transfer coefficients and areas are calculated from the geometric data (EDR results) and feed streams.

3.3.2. Compressors

Compressors can be modelled with a determined constant efficiency or by supplying compressor performance curves (head versus volumetric flow curves) where in fact the efficiency is calculated as a function of volumetric flow for various compressor speeds. Fan Laws are used to model speed dependent variations in performance, so that a single performance curve is enough to describe the compressor behavior at any speed and simulates it more precisely. These laws reveal the fundamental operating principles of compressors that volume capacity (actual volume flow) is proportional to the compressor speed and head is proportional to the square of compressor speed and power to cube (Eqs. 4,5 and 6) [20]:

$$\frac{V_2}{V_1} = \frac{N_2}{N_1} \quad (4)$$

$$\frac{H_2}{H_1} = \left(\frac{N_2}{N_1}\right)^2 \quad (5)$$

$$\frac{W_2}{W_1} = \left(\frac{N_2}{N_1}\right)^3 \quad (6)$$

In these equations, V is the volume flow, H is the head, W is the power (work) and N is the compressor speed. The fan laws generate approximate results which are reasonable in the 80 to 105% speed range [20]. And the adiabatic efficiency of the compressor is calculated as Eq. 7 [19]:

$$\text{Head} = \frac{\text{Work Required}_{(\text{actual})}}{\text{Mass Flow Rate}} \times \text{Adiabatic Efficiency} \times \frac{1}{g} \quad (7)$$

where g is the acceleration of gravity. In the MFC process, performance curves combined with the simulator are used for simulation of compressors. For example, the performance curve of comp-1/1 is illustrated in (Figure3). These curves are obtained based on the fan laws.

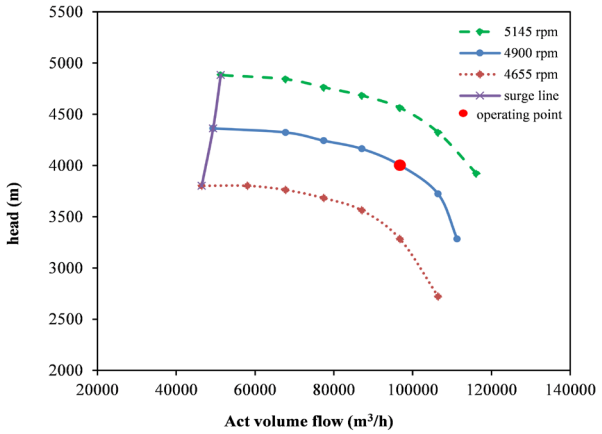

Figure 3. Performance curve of Comp-1/1 at different compressor speeds.

4. Control Structure Design of MFC Process

4.1. Process Control

In general, process control refers to the techniques which are used to control process variables when manufacturing a product. A control system is based on the following demands [21]: to eliminate the effect of external disturbances and reduce variability, to ensure the stability and safety, to optimize the performance of chemical processes and increase their efficiency. According to Skogestad [22], control structure design for complete chemical plants is known as plant-wide control which deals with the control philosophy of the overall plant and it is defined as the structural decisions involved in control system design, such as:

- Selection of controlled variables (CVs) and set points (SPs)
- Selection of manipulated variables (MVs)
- Selection of measurements
- Selection of control configuration
- Selection of controller type (control law specification, e.g. PID, etc.).

In the remainder of section 4, the tasks listed above will be discussed to achieve purpose of this paper.

4.2. Selection of Controlled Variables

The issue of selecting controlled variables or process variables (PVs) is the first and main decision in the control structure design problems. While selecting process variables, these four requirements should be observed [22]:

- The optimal value of the PV should be insensitive to disturbances
- The PV should be easy to measure and control
- The PV should be sensitive to changes in the manipulated variables
- In case of multiple PVs, the selected PVs should be independent.

Also, there are different criteria that contribute to this decision, such as product quality requirements, energy consumption, equipment capacity, and limitations due to safety. It should be said that the focus of this study is on the specific energy consumption (SEC) of the whole process, i.e. this parameter is the objective function and the selected process variables must be controlled in a way that the SEC remains lower than 0.3 kWh/kg LNG.

In the discussed process (MFC), flow rate of refrigerants, outlet temperature of heat exchangers, outlet temperature of air coolers, outlet pressure of compressors, and liquid level of vertical separator must be controlled. These are selected controlled variables. Each of these PVs except liquid level of separator can affect the SEC.

4.3. Selection of Manipulated Variables and Degrees of Freedom (DOF) Analysis

After selection of process (controlled) variables, it should be decided which manipulated variable has to be linked with which process variable. Variables (MV & PV) should be paired in such a way that the MV has a considerable effect on the PV and any time lag from a change in the MV should be short in PV response [9]. Selection of the manipulated variables is usually not an individual decision of control structure design problem, since these variables are the direct consequence of the "selection of controlled variables" step [23].

According to [22], the number of dynamic or control degrees of freedom is equal to the number of manipulated variables. In most cases, the MVs are obtained by the design, and a DOF analysis should be used to check that there is enough DOF to meet the operational objectives [22]. If the DOF analysis and/or the subsequent design indicates that there are not enough degrees of freedom, then DOF should be added with the addition of equipment like control valves [22]. The variables that can be manipulated in the MFC process are 18 in total including:

- Molar flow of mixed refrigerants (steams: 10, 16, 21 and 25), using the V-1, V-2, V-3 and V-4 control valves
- Speed of air coolers' driving motor, using the "Control OP Port" option for these variables
- Compressor powers, using the "Control Valve" option for these energy streams
- LNG molar flow rate, using the V-6 control valve
- NG molar flow rate (can also be considered as a disturbance)

So DOF equals 18.

4.4. Selection of Control Configuration and Equipment Control Structure

The control configuration is the structure of a controller that interconnects the process variables, manipulated variables and measured variables [23]. Here, feedback and cascade control configurations are selected for controlling the PVs. These two types are the most conventional in plant-wide control. In the following, the selected control structures and methods for controlling the selected PVs will be discussed:

- *Control of flow rate of mixed refrigerants*:

Since the flow rate of refrigerants has a great impact on the SEC, flow controllers for all MR streams must be added. For control of these variables, cascade control structure can be used. In cascade control structure, natural gas temperature controllers (primary or master controllers) send their output as set point to flow controllers (secondary or slave controllers) that manipulates the control valves.

- *Control of outlet temperature of heat exchangers and air coolers*:

Feedback control systems are used to control temperatures. In the MFC process, outlet temperatures on the tube side of all heat exchangers are controlled by manipulating the flow rates of the cooling fluids (mixed refrigerants). And outlet temperatures of all air coolers are controlled by manipulating the speed of the air coolers' driving motor.

- *Control of discharge pressure of compressors*:

Compressors are critical equipment in ensuring the stable and safe operation of the LNG plants. Improper operation of compressors increases the value of the SEC, so it is essential to design control systems for these equipment. The control structure of compressors is selected based on their type and size. Because of using centrifugal compressors in the MFC process, discharge pressures are controlled by varying the energy input to the compressors (in fact, work of the turbines).

- *Control of liquid level in the vertical separator*:

Basically, change of liquid level in a separator depends on the volume and shape and the flow rate of the input and output streams of the separator. Here, the liquid level is controlled by using a feedback configuration which is very common. In this system, the level controller controls the PV by manipulating a control valve which is located on the outlet stream of the separator vessel. According to the above explanations, the control structure is designed for the MFC process which is shown in (Figure 4).

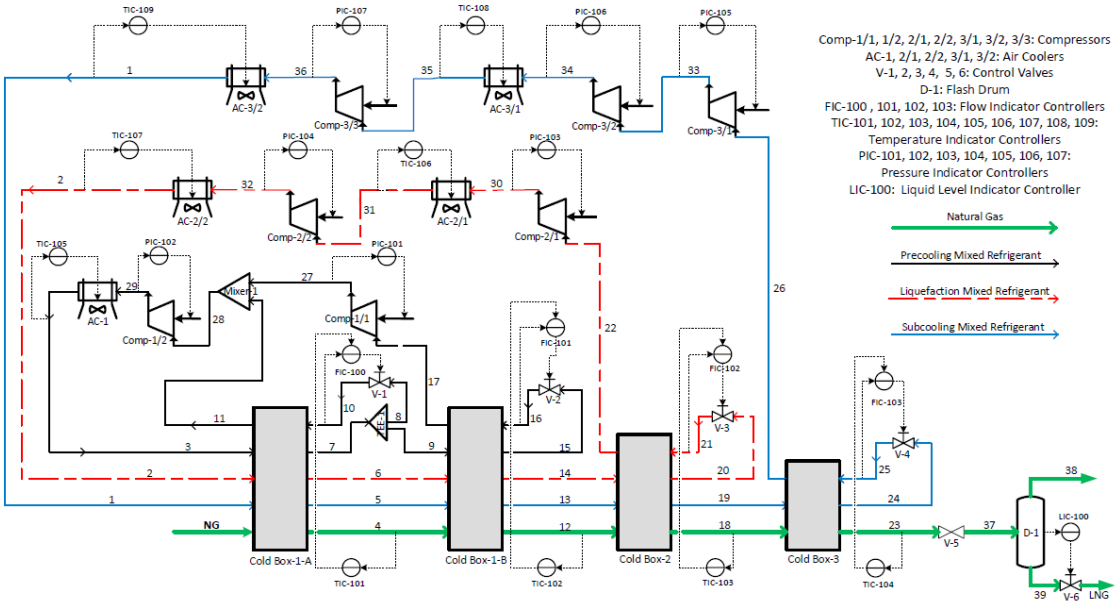

Figure 4. Designed control structure for MFC process.

4.5. Selection of Controller Type

One of the important issues in simulation and process control is the selection of the appropriate controller and tuning of its parameters. The most widely used control technology in the plants is the PID controller. The PID controller algorithm utilizes proportional (P), integral (I) and derivative (D) action to maintain the process variable at a set point. One or more of these actions can be selectively employed, according to what process variables that are being controlled. The output of the PID controller is defined as [24]:

$$OP(t) = K_c\,\varepsilon(t) + \frac{K_c}{T_i}\int \varepsilon(t) + K_c T_d \frac{d\varepsilon(t)}{dt} \qquad (8)$$

where ε is the error or deviation from set point, Kc is the controller gain, T_i and T_d are two constants called the integral time and derivative time, respectively. The value of these parameters depends on the type of controller and to a lesser extent the process features, and there are various methodologies for deciding these values and the PID controller tuning. Here, for controller tuning, approximate values of controller parameters suggested in reference [24] are used. Appropriate controller according to the process variables and the range of values used for each controller parameter are given in Table 6. In general, K_c is the most principal parameter of controller equation, and T_i and T_d are auxiliary parameters that are used to trim the proportional response. Therefore, the controller gain has to be tuned first and the response of the controller should be close to the desired response before any changes in integral and derivative parameters. If the controller does not work well and instability occurs, the controller gain should be adjusted first and T_i and T_d should be adjusted afterwards.

Table 6. Appropriate controller according to process variables and its parameters [24].

Process Variable	Controller	K_c	T_i (min)	T_d (min)
Flow	PI	0.40-0.65	0.05-0.25	---
Temperature	PID	2-10	2-10	0-5
Gas Pressure	PI	2-10	2-10	---
Liquid Level	P	2	---	---

5. Dynamic Simulation of MFC Process

5.1. Dynamic Simulation

Design and optimization of chemical processes requires the study of both steady state and dynamic behavior. Dynamic simulation shows the behavior of the process over time to reach a new steady state and ensures that the plant produces the desired product in a way that is safe and easy to operate.

The dynamic mode of the simulator calculates the pressure and flow profile of a simulation by utilization of pressure flow solver (P-F solver). In this mode, all equations of equipment are solved simultaneously at any time, and calculations at any interval of time are transferred from an earlier time to a later time and this procedure continues until the final time that the user determines. For dynamic simulation, specifications or dynamic characteristics of equipment and boundary streams should be determined. The pressure-flow specifications must be chosen so that the degrees of freedom of the process equal zero in order for the software to run the simulation successfully. These specifications (Spec) are discussed in the following:

- A dynamic specification- pressure or flow- should be selected for each boundary stream (feed and product). In the MFC process, pressure is specified for the NG and 38 streams, and flow is specified for the LNG stream.
- In resistance equipment, such as compressors, heat exchangers, air coolers and control valves, the required parameters must be imported to the simulator in order to determine the relationship between pressure drop and flow rate. This relationship is known as the resistance equation (Eq. 9). The resistance equation calculates flow rates from the pressure differences of the equipment.

$$\text{Flow} = k\,\sqrt{\rho.\Delta P} \qquad (9)$$

According to the equation 9, in these equipment the flow rate is directly related to

the square of the pressure drop and if the flow rate through the equipment increases, the pressure drop will also increase. k is the density and k is a constant that depends on mechanical properties of the equipment and represents the reciprocal of resistance to flow. So the k value should be selected as a Spec in heat exchangers and air coolers. In valves, the pressure-flow relation option should be selected as a dynamic Spec so that the pressure drop across the valve at any moment is calculated based on the basic valve operation equation. And in compressors, performance curves at different speeds, such as that in (Figure 3), should be used and the compressor speed should be considered as a dynamic Spec.

5.2. Simulation Results and Discussion

Dynamic simulation of the MFC process is run to check the performance of the designed control structure. Results from the simulations are shown in (Figures 5-9) as plots of set points (SP), process variables (PV) and operating variables (OP). In fact, OP is the manipulated variable which the controller controls the PV by changing it. Here, the output of the controller is a control valve, i.e. OP is the percent opening (OP %) of the control valve. In addition, the OP can be specified as a physical valve in the plant, a material stream, or an energy stream [24]. In all figures, the red dotted line represents the set point, the black solid line represents the process variable and the blue dashed line denotes the valve opening. As can be seen in the figures, all the controllers do well and the PVs will reach the desired SPs with the least amount of offset. It should be noted that controller parameters are tuned so that the controllers have stability, the amount of their offset is as small as possible, have shorter response times and can also eliminate any disturbances.

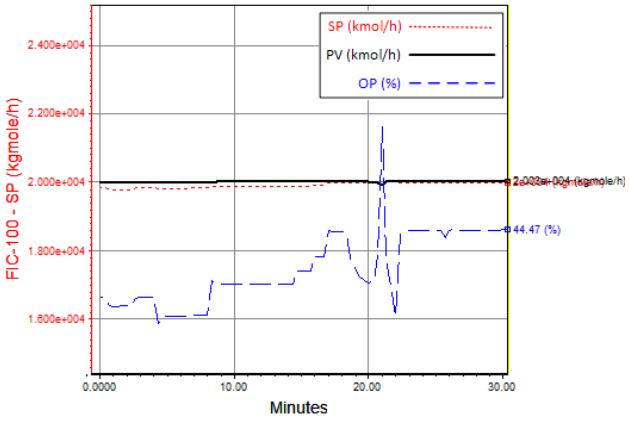

a. FIC-100 controller
(with Remote SP= 2.000×10^4 kmol/h)

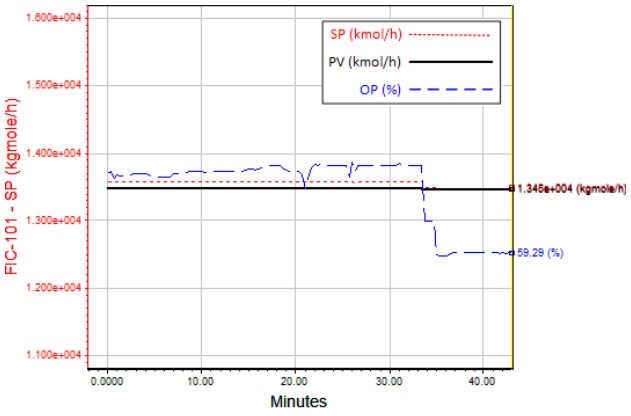

b. FIC-101 controller
(with Remote SP= 1.348×10^4 kmol/h)

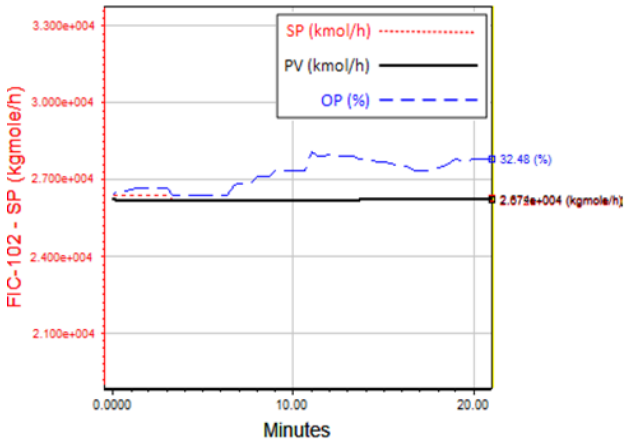

c. FIC-102 controller
(with Remote SP= 2.672×10^4 kmol/h)

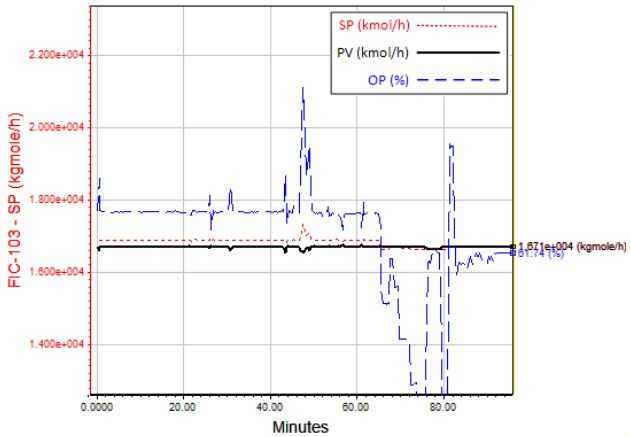

d. FIC-103 controller
(with Remote SP= 1.671×10^4 kmol/h)

Figure 5. (a-d). Response of flow controllers.

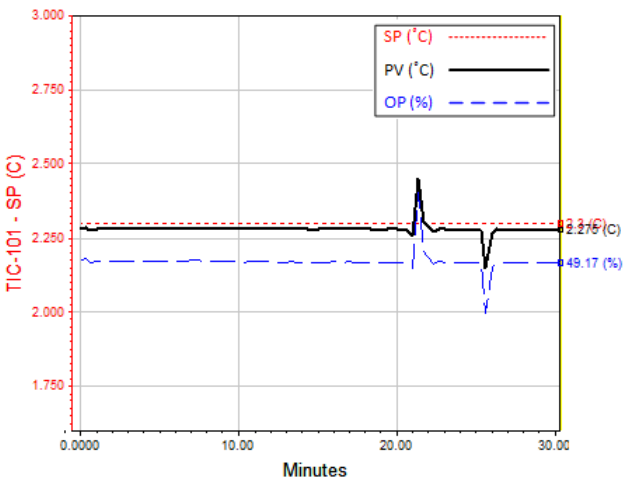

a. TIC-101 controller (with SP= 2.3 °C)

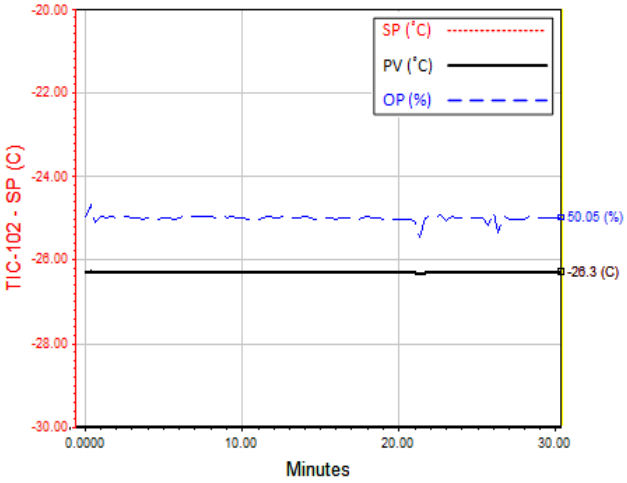

b. TIC-102 controller (with SP= -26.3 °C)

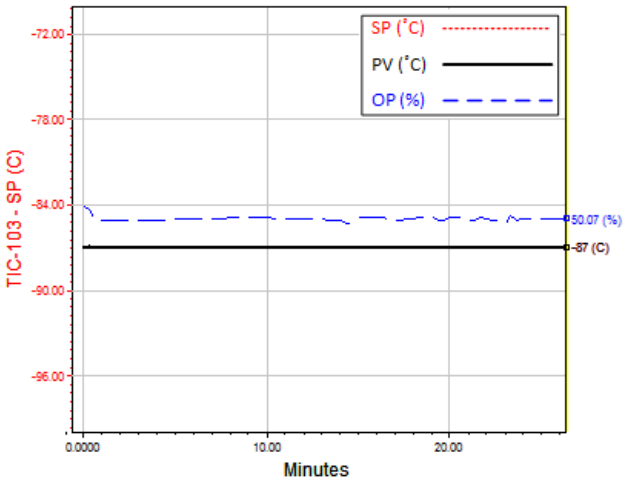

c. TIC-103 controller (with SP= -87 °C)

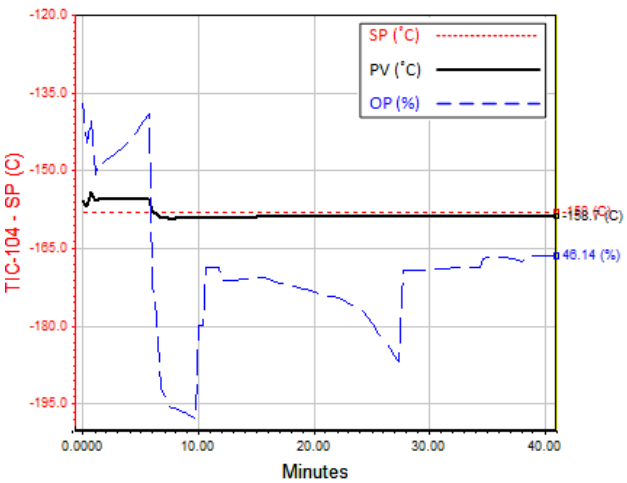

d. TIC-104 controller (with SP= -158 °C)

Figure 6. (a-d). Response of temperature controllers for heat exchangers.

(Figure 5) illustrates the responses of the flow controllers. These controllers are slave controllers and get their SPs from related temperature controllers (master controllers), i.e. their SPs are remote. The action of FICs: 100-104 is reverse which means that when the PV rises above the SP, the OP decreases, and when the PV falls below the SP, the OP increases. The responses of the temperature controllers (TICs: 101-104) are shown in (Figure 6). These controllers are set to control the temperatures at the tube outlet of heat exchangers and they have direct action. In direct action, if the PV rises above the SP, the OP increases and vice versa. From the figures, it can be found that if there is little MR in the heat exchangers, this will mean there is less heat transfer than necessary and it causes a rise in the temperature at the tube outlet. Of course, this will lead to an increase in the flow rate of MR to the heat exchangers, and the temperatures or PVs will reach the desired SPs. (Figure 7) shows the responses of the temperature controllers (TICs: 105-109) for air coolers. The action of such controllers is direct, i.e. if the outlet temperature of air coolers is higher than the desired SPs, the rotational speed of the driving motors increases in order for the PVs to reach the SPs. As can be seen, these controllers do not show much oscillation and the PV was kept close to the SP throughout most of the simulation. (Figure 8). (a-g) shows how the discharge pressure varies with time

in the compressors. These pressure controllers have reverse action, meaning that more power (energy) will be required if the PV is less than the SP. One can see that these compressors never need to go to full power (OP=100 %) in order to maintain the desired pressure and have approximately stable behavior. Finally, (Figure 9) indicates the level controller (LIC-100) response. The level controller acts directly and keeps the liquid level in the separator close to the SP.

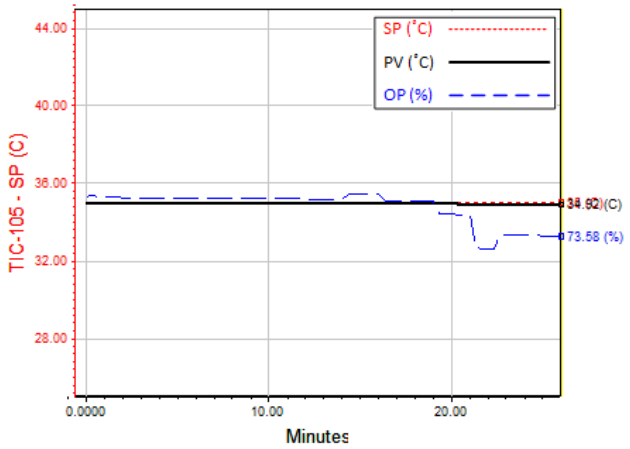

a. TIC-105 controller (with SP= 35 °C)

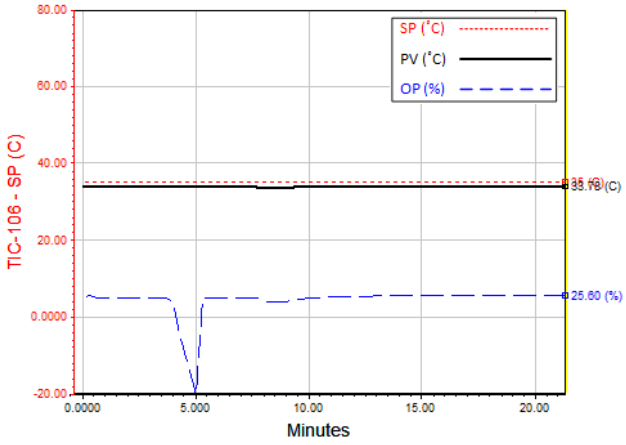

b. TIC-106 controller (with SP= 35 °C)

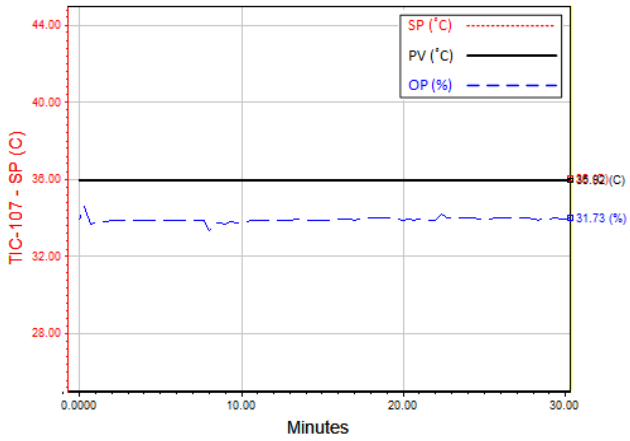

c. TIC-107 controller (with SP= 36 °C)

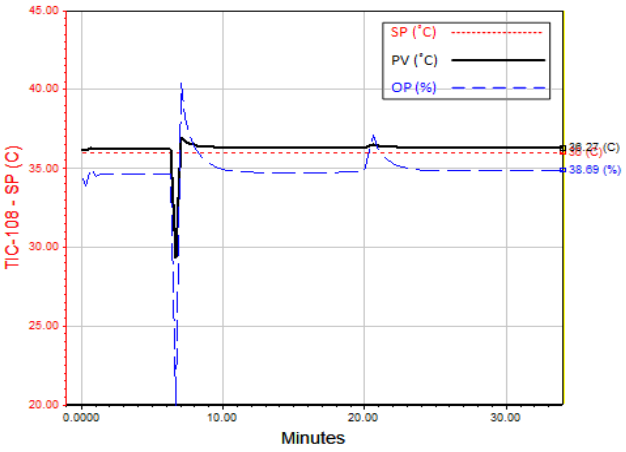

d. TIC-108 controller (with SP= 36 °C)

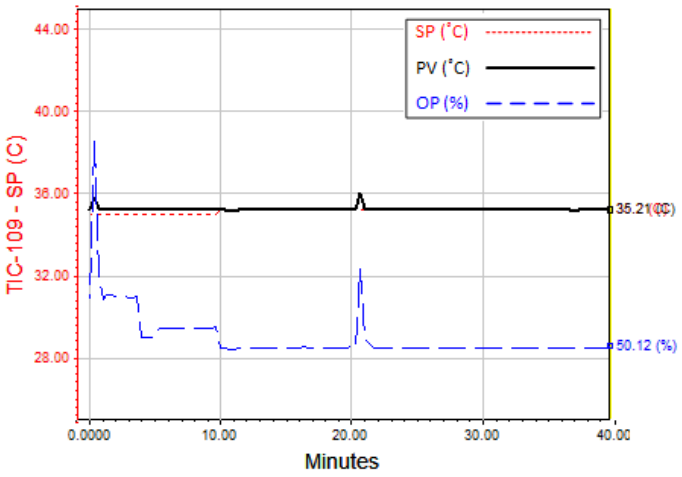

e. TIC-109 controller (with SP= 35.2 °C)

Figure 7. (a-e). Response of temperature controllers for air coolers.

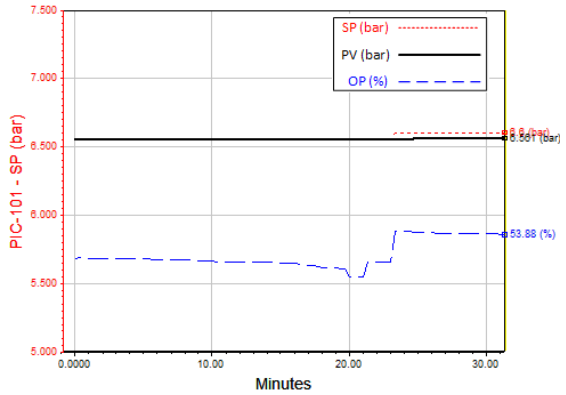

a. PIC-101 controller (with SP= 6.6 bar)

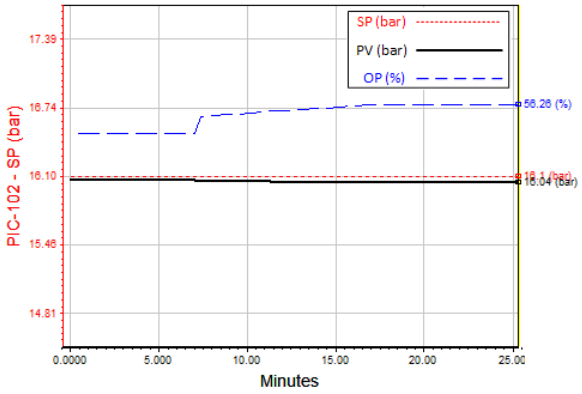

b. PIC-102 controller (with SP= 16.1 bar)

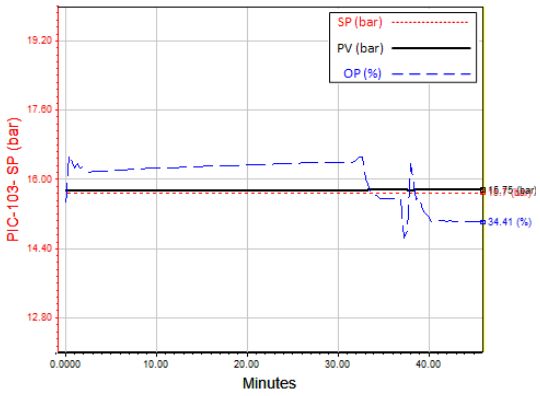

c. PIC-103 controller (with SP= 15.7 bar)

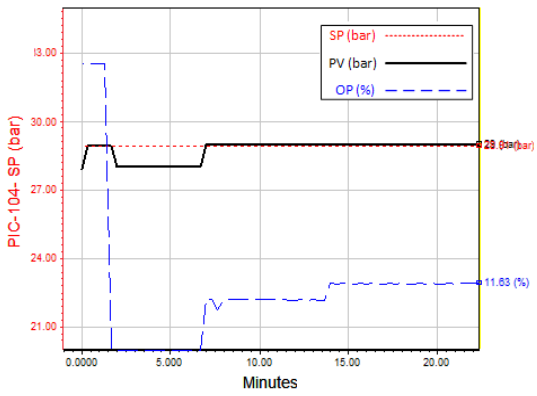

d. PIC-104 controller (with SP= 29 bar)

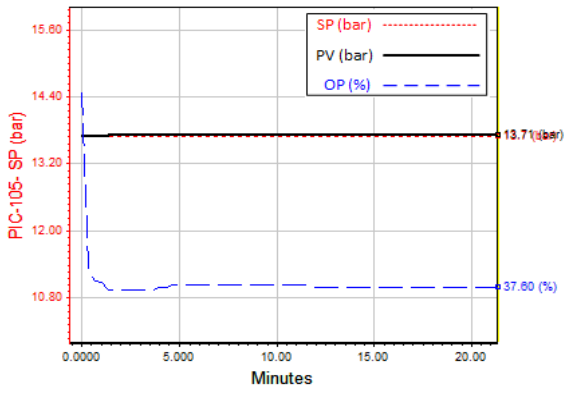

e. PIC-105 controller (with SP= 13.7 bar)

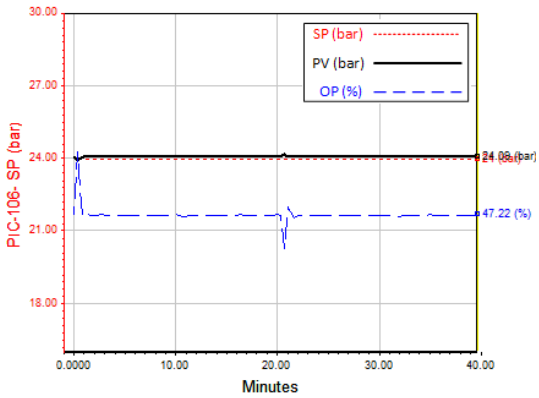

f. PIC-106 controller (with SP= 24 bar)

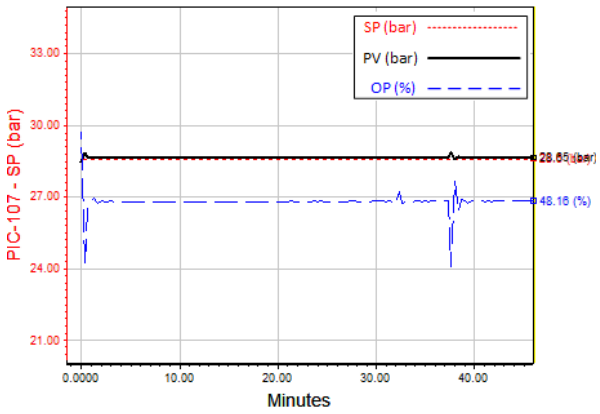

g. PIC-107 controller (with SP= 28.6 bar)

Figure 8. (a-g). Response of pressure controllers.

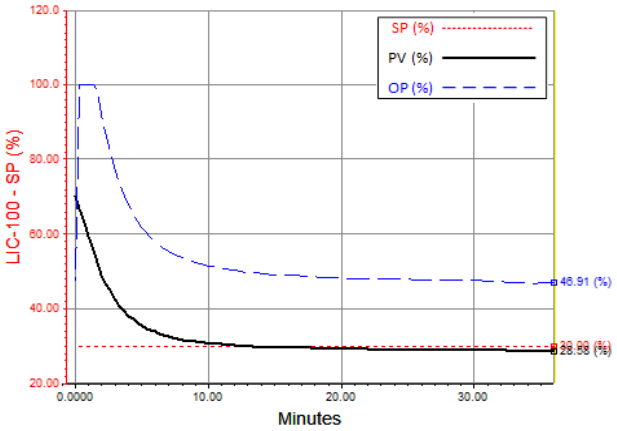

Figure 9. Response of level controller (LIC-100 with SP= 30%).

In the end, it should be mentioned that for all the simulations, there is some deviation from steady state before any disturbances are introduced, i.e. the desired value (SP) of process variables is different from the ones which they have in the steady state mode. The reason is that the controllers have different operation points from which was initially defined and also there is unphysical initial values for liquid hold ups in the heat exchangers, hence the controllers cannot bring the PVs up to the desired values. As mentioned before, the main control objective is, of course, to maintain the value of SEC less than 0.3 kWh/kg LNG. In this regard, after dynamic simulation the amount of SEC in the designed control structure equals 0.2574 kWh/kg LNG and it indicates that this structure controls the process variables desirably.

5.3. Validation of Designed Control Structure

After designing a control structure, it is necessary to validate the designed structure. In fact, a control structure has an appropriate and stable performance when be able to overcome the imposed disturbances in the process. Disturbances upset the process and cause the PVs to deviate from their desired SPs. These disturbances may be caused by the external factors (such as flow rate, temperature or pressure fluctuations in the inlet streams of the process) or internal ones (like defects in the instrumentation).

In the under consideration process, two potential sources of disturbance are identified which include variation of the NG feed stream molar flow rate and temperature. These disturbances can be imposed on the MFC process by means of Transfer Function block provided in the simulator, and thus the performance and responses of the controllers can be studied. For investigating the effect of both increase and decrease of the inlet NG flow rate and temperature on the process, the disturbances are introduced to the process as sinusoidal. (Figure 10.a) shows the disturbance in feed molar flow rate and the disturbance in feed temperature is shown in (Figure 10.b). Here, it is assumed that the disturbances in the process will take 40 minutes (with period= 20 min, i.e. the disturbances are started at 10 minutes and terminated at 50 minutes).

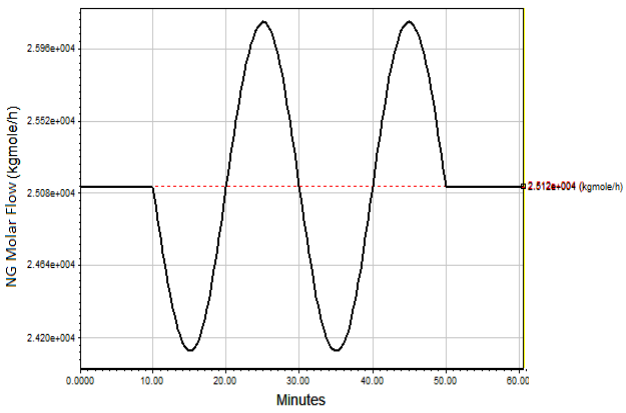

a. NG molar flow rate oscillation

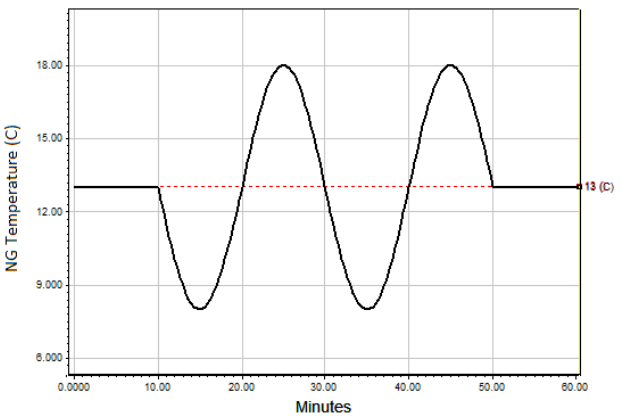

b. NG temperature oscillation

Figure 10. Disturbances of MFC process: a. NG molar flow rate oscillation & b. NG temperature oscillation.

Due to the high number of controllers in the process, only the results of the responses of FIC-100 and TIC-101 controllers are shown in (Figure 11). These figures illustrate how the controllers responded to disturbances. Because these controllers are at the beginning of the process, they eliminate most of the imposed disturbances and prevent them from upsetting the remainder of the process. After introducing the disturbances, all of the controllers try to eliminate these disturbances by sending signals to the control valves to open or close. This indicates that the designed control structure has good stable performance.

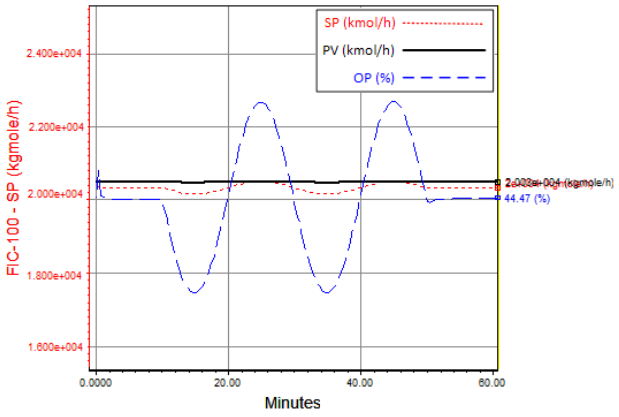

a. FIC-100 controller after flow disturbance

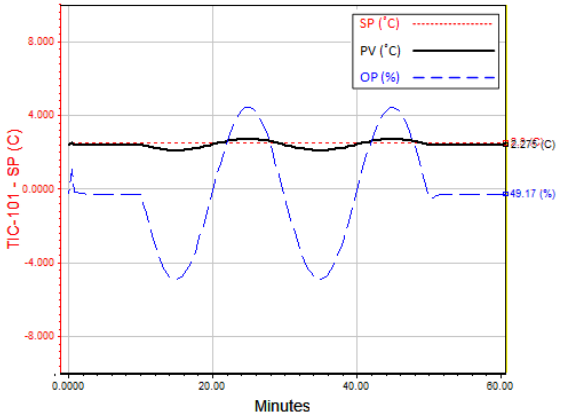

b. TIC- 101 controller after flow disturbance

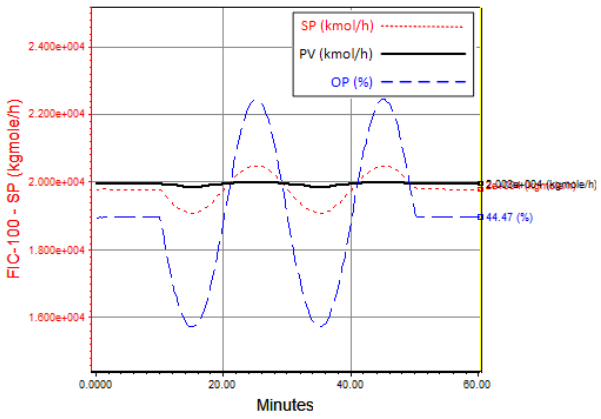

c. FIC-100 controller after temperature disturbance

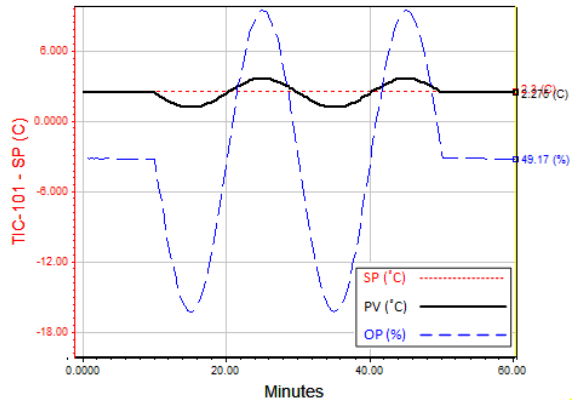

d. TIC-101 controller after temperature disturbance

Figure 11. (a-d). Response of controllers after introducing disturbances.

6. Conclusions

In this paper, static and dynamic simulation of the MFC process is done. Results of steady state simulation shows that the specific energy consumption (SEC) of the process is 0.2647 kWh/kg LNG. By dynamic simulation, different control strategies are examined in order to select the best controllers and control structure. The process can produce LNG product safely and stably by using the proposed control structure. These control systems are able to sufficiently eliminate the imposed disturbances in the process. Also the amount of SEC of the process is 0.2574 kWh/kg LNG in the designed control structure. These results show that this structure perform accurately.

Nomenclature

$\dot{m}$	fluid mass flow rate (kg/s)
h	specific enthalpy (J/kg)
Q_{leak}	heat leak (W)
Q_{loss}	heat loss (W)
$Q_{transferred}$	heat exchanger duty (W)
U	overall heat transfer coefficient ($W/m^2.°C$)
A	surface area (m^2)
CMTD	corrected log mean temperature difference (°C)
V	volume flow (m^3/s)
H	head (m)
W	power (work) (W)
N	compressor speed (rpm)
g	acceleration of gravity (m/s^2)
K_c	controller gain (dimensionless)
T_i	integral time (min)
T_d	derivative time (min)
k	specification constant $((kg/s)/(pa.kg/m^3)^{0.5})$
ρ	density (kg/m^3)
ΔP	pressure drop (Pa)

Abbreviations

C3MR	Propane Pre-Cooled Mixed Refrigerant
CV	Controlled Variable
DOF	Degrees of Freedom
EDR	Exchanger Design & Rating
EOS	Equation of State
J-T Valve	Joule-Thomson Valve
LNG	Liquefied Natural Gas
MFC	Mixed Fluid Cascade
MR	Mixed Refrigerant
MSMR	Modified Single Mixed Refrigerant
NG	Natural Gas
OP	Operating Variable
PFHE	Plate Fin Heat Exchanger
PR	Peng-Robinson
PRSV	Peng-Robinson-Stryjek-Vera
PV	Process Variable
SEC	Specific Energy Consumption
SP	Set Point
Spec	Specification
SWHE	Spiral Wound Heat Exchanger

7. References

[1]. Petroleum, B., 2018 BP Energy Outlook. 2018, BP London, UK.

[2]. Mokhatab, S., et al., Handbook of liquefied natural gas. 2013: Gulf Professional Publishing.

[3]. Shukri, T., LNG technology selection. Hydrocarbon engineering, 2004. 9(2): p. 71-76.

[4]. LNG Technology, The Linde. Group: "http://www.linde-engineering.com/internet.global.lindeengineering.global/en/images/LNG_1_1_e_13_150dpi19_4577.pdf".

[5]. Vatani, A., M. Mehrpooya, and A. Palizdar, Energy and exergy analyses of five conventional liquefied natural gas processes. International Journal of Energy Research, 2014. 38(14): p. 1843-1863.

[6]. Song, K., et al. Dynamic simulation of natural gas liquefaction process. in 22nd European Symposium on Computer Aided Process Engineering. 2012. Elsevier.

[7]. Khan, M.S., et al. Robust control of Propane Pre-cooled mixed refrigerant process for natural gas liquefaction. in Control Automation and Systems (ICCAS), 2010 International Conference on. 2010. IEEE.

[8]. Vatani, A., M. Mehrpooya, and A. Palizdar, Advanced exergetic analysis of five natural gas liquefaction processes. Energy Conversion and Management, 2014. 78: p. 720-737.

[9]. Jacobsen, M.G., Optimal Operation of Cooling Cycle/LNG Process. 2007, Norwegian University of Science and Technology.

[10]. Stephenson, G. and L. Wang, Dynamic simulation of liquefied natural gas processes. Hydrocarbon Processing, 2010.

[11]. Husnil, Y.A., C. Park, and M. Lee. Simulation

based Heuristics Approach for Plantwide Control of Propane Precooled Mixed Refrigerant in Natural Gas Liquefaction Process. in 11th International Symposium on Process Systems Engineering-PSE2012. 2012. Elsevier.

[12]. Husnil, Y.A., G. Yeo, and M. Lee, Plant-wide control for the economic operation of modified single mixed refrigerant process for an offshore natural gas liquefaction plant. Chemical Engineering Research and Design, 2014. 92(4): p. 679-691.

[13]. Singh, A. and M. Hovd. Dynamic modeling and control structure design for a liquefied natural gas process. in American Control Conference, 2007. ACC'07. 2007. IEEE.

[14]. Venkatarathnam, G. and K.D. Timmerhaus, Cryogenic mixed refrigerant processes. 2008: Springer.

[15]. "Aspen HYSYS Simulation Basis" manual. 2010. Aspen Technology, Inc.

[16]. Alabdulkarem, A., et al., Optimization of propane pre-cooled mixed refrigerant LNG plant. Applied Thermal Engineering, 2011. 31(6-7): p. 1091-1098.

[17]. Waldmann, I. Evaluation of process systems for floating LNG production units. in Tekna conference. 2008.

[18]. Mandler, J.A., Modelling for control analysis and design in complex industrial separation and liquefaction processes. Journal of process control, 2000. 10(2): p. 167-175.

[19]. "Aspen HYSYS Unit Operations Guide" manual. 2010. Aspen Technology, Inc.

[20]. GPSA Engineering Data Book. 2004: GPSA.

[21]. Stephanopoulos, G., Chemical process control: An Introduction to Theory and Practice. 1984: Prentice-Hall.

[22]. Skogestad, S., Control structure design for complete chemical plants. Computers & Chemical Engineering, 2004. 28(1): p. 219-234.

[23]. Larsson, T. and S. Skogestad, Plantwide control-A review and a new design procedure. Modeling, Identification and Control, 2000. 21(4): p. 209-240.

[24]. "Aspen HYSYS Dynamics" manual. 2010. Aspen Technology, Inc.

[25]. Mehrpooya, M., A. Vatani, and S. Mousavian, Optimum design of integrated liquid recovery plants by variable population size genetic algorithm. The Canadian Journal of Chemical Engineering, 2010. 88(6): p. 1054-1064.

JOURNAL OF GAS TECHNOLOGY

Volume 5 / Issue 1 / Summer 2020 / Pages 22-31

Journal Homepage: http://jgt.irangi.org

Application of Hydraulic Flow Unit Technique for Permeability Prediction in one Iranian Gas Reservoirs, Case Study

Asghar Gandomkari*

- Chemical and Petroleum Engineering Dept., School of Chemical and Material Eng., Shiraz Branch, Islamic Azad University, Shiraz, Iran

ARTICLE INFO

ORIGINAL RESEARCH ARTICLE

Article History:
Received: 10 February 2020
Revised: 5 May 2020
Accepted: 22 June 2020

Keywords:
Flow Zone Indicator
HFU
Gas Reservoir
Histogram Analysis
Probability Plot
SSE

ABSTRACT

Estimating reservoir permeability in un-cored intervals-wells are a generic problem common for all reservoir engineers. In this paper, routine core analysis and well log data of an actual existing gas reservoir, from southwest west of IRAN, were used to develop a model of matrix permeability in un-cored well by using Hydraulic Flow Unit Approach (HFU). The Graphical Clustering Methods such as histogram analysis and probability plot are used to identify the number of hydraulic flow units. Also, the sum of square errors (SSE) method was used as criterion for confirming the optimal number of HFU's. Permeability data can be obtained from well tests, cores or logs. Normally, using well log data to derive estimates of permeability is the lowest cost method. Formation permeability controls the strategies involving well completion, stimulation, and reservoir management.

Results showed that six HFUs were identified from core data and each unit has its own mean Flow Zone Indicator (FZI). In addition, a correlation between FZI calculated from core data and that obtained from well log data was developed for estimating permeability in un-cored intervals-wells with R-Squared Value of 0.60. Also, Lorenz plot shows that the flow units 3 and 6 have a good porosity and high permeability.

DOR: 20.1001.1.25885596.2020.5.1.2.2

How to cite this article
A. Gandomkari. Application of Hydraulic Flow Unit Technique for Permeability Prediction in one Iranian Gas Reservoirs, Case Study. Journal of Gas Technology. 2020; 5(1): 22 -31. (http://jgt.irangi.org/article_251657.html)

*Corresponding author.
E-mail address: agandomkar@shirazu.ac.ir (A. Gandomkari)

Available online 20 September 2020

1. Introduction

Permeability is one of rock properties whose quantity is essential to know, in order to measure the flowing capability of a rock (Kadkhodaie et. al., 2013; Susilo, 2010). Permeability data can be obtained from well tests, cores or logs. However, because the costs to cut and analyze cores are so high, few core measurements are routinely available. Normally, one of the methods to calculate permeability, especially in the zone, which does not have any core data is through using the empirical relationship with rock porosity (Figure 1), (Hatampour et. al., 2015; Shenawi and White, 2007, and Elarouci and Mokrani, 2010).

Rock permeability is an extremely important parameter in reservoir characterization and simulation, because it influences the hydrocarbon rate of production, ultimate recovery, optimal placement of wells, pressure and fluid contacts evolution (Nelson, 1994 and 2005). Thus, the proper determination of the permeability is of paramount importance because it affects the economy of the whole venture of development and operation of a field. Therefore, permeability is a key parameter in any reservoir characterization that governs in great extension its handling and development (Iravani et. al., 2018; Soto and Torres, 2001).

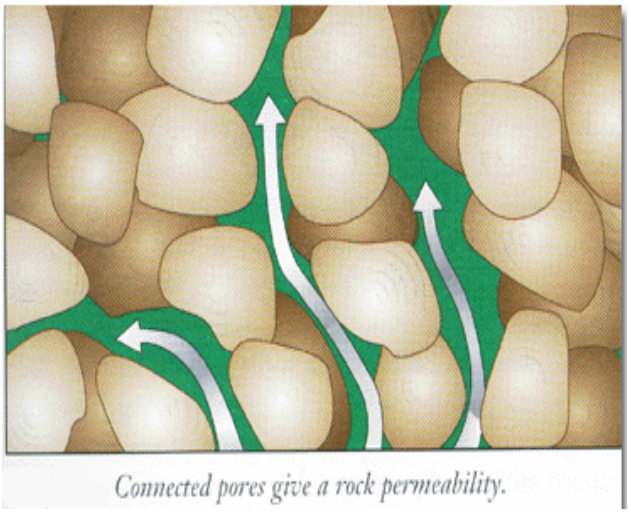

Figure 1: Permeability and Pore Size Distribution

Although permeability values are best determined from core data, most wells are not cored. Consequently, permeability values in un-cored wells are usually estimated from porosity and permeability relationships developed from core data (Oliveira et. al. 2016; Maghsood and Fujimoto, 1995).

The regression models assume that a linear relationship between logarithmic permeability and porosity exists. This method is an empirical method that does not have any basic theory which is applicable for homogeneous reservoir.

$$\text{Log } K = a\ (Ø) + b \qquad (1)$$

This method proposed by Canas and Malik, (2000) but ignores the scatter of the data around the fitted line and attributes any scatter to measurement errors. The routine core analysis data of an actual existing gas reservoir were used and show in (Figure 2).

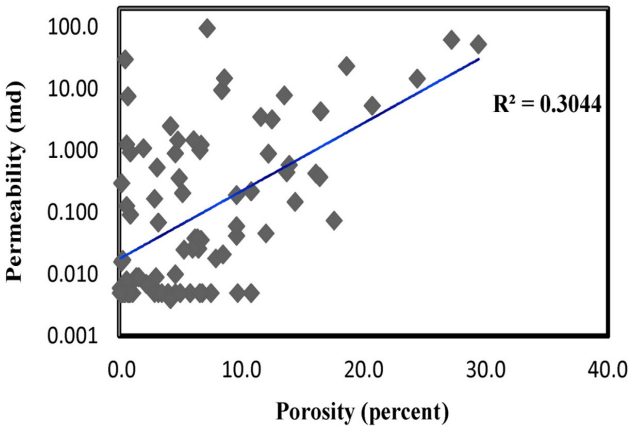

Figure 2: Conventional Porosity - permeability Relationship

Thus, the best correlation between porosity and permeability can be obtained if rocks with similar fluid flow properties are identified and grouped together. Each group is referred to as a hydraulic flow unit.

The objective of this work is to develop a model of matrix permeability by using the Flow Zone Indicator for permeability prediction in un-cored well. All the datasets are gained from routine core analyses and well log data

performed in the gas reservoir. Three approaches, such as Histogram analysis, probability plot and sum of square error method are used to identify the number of hydraulic flow units. Predicted permeability was compared with core measured permeability achieved from the core lab database.

2. Application of Hydraulic Flow Unit (HFU) in Reservoir Characterization

Flow unit is defined by Ebanks (1990) as the mappable portion of the reservoir rock within which geological and petrophysical properties that affect fluid flow are internally consistent and predictably different from properties other rock volumes.

There is no unique way to determine rock flow characteristics. This results from the fact that the flow characteristics depend on a variety of parameters such as porosity, permeability, wettability and to some extent on fluid properties. Typically rock typing is accomplished based on several methods each of them has its own engineering basis. The most commonly used methods are porosity-permeability cross plot, Archie's formula based method, capillary pressure, Leverett J-function and flow zone indicator (Saboorian and Mowazi, 2010) .However, none of the above techniques except The FZI method gives rise to a right way to develop a permeability model for this reservoir.

3. Flow Zone Indicator (FZI) Concept

Amaefule and Altunbay, (1993) considered the role of the mean hydraulic radius in defining hydraulic flow units and correlating permeability from core data. Their approach was essentially based on a modified Kozeny-Carmen (1958) equation coupled with the concept of mean hydraulic radius. The equation indicates that for any hydraulic flow unit, a log-log plot of a "Reservoir Quality Index" (RQI) versus "Normalized porosity index" that is the pore volume to grain volume ratio ($Ø_z$) should yield a straight line with a unit slope. The intercept of unit slops with $Ø_z = 1$, designate as "The Flow Zone Indicator", and is a unique parameter for each hydraulic flow unit. The computations are as follows: (Abbaszadeh and Fujimoto, 1996, Kozeny, 1927)

Normalized Porosity Index,

$$Ø_z = \frac{Ø}{1 - Ø} \tag{2}$$

Reservoir Quality Index,

$$\mathrm{RQI} = 0.314\sqrt{\frac{k}{Ø}} \tag{3}$$

Flow Zone Indicator,

$$\mathrm{FZI} = \frac{\mathrm{RQI}}{Ø_z} \tag{4}$$

So if Eq. (4) is switched to a logarithm, the equation becomes:

$$\mathrm{Log\ RQI} = \mathrm{Log}\ Ø_z + \mathrm{Log\ FZI} \tag{5}$$

Samples having a similar FZI value will lie on similar lines with similar gradient value as one, in a log-log plot between RQI and $Ø_z$. These samples have similar pore throat attributes and thereby constitute a hydraulic flow unit. On the other hand, samples having a different FZI will lie on other parallel lines (Williams and Batarseh, 2010, Elarouci and Mokrani, 2010).

4. Data analysis

4.1. Core data

All the data sets of permeability and porosity are taken from core samples with a depth range of 2823 to 2873 m (Table 1). The core samples have very wide ranges of porosity (0.1 to 29.4 Percent) and permeability (0.004 to 95.65 md).

Table 1: Routine Core Analysis Data, Permeability and Porosity

Porosity(fraction)	Permeability(md)	$(Ø)_z$	RQI	FZI
0.046	0.906	0.048	0.139	2.890
0.075	0.005	0.081	0.008	0.099
0.058	0.005	0.061	0.009	0.149
0.02	1.095	0.020	0.232	11.38
0.046	0.005	0.048	0.010	0.214
0.029	0.005	0.029	0.013	0.436
0.062	0.038	0.066	0.024	0.371
0.022	0.007	0.022	0.017	0.787
0.066	0.005	0.070	0.008	0.122
0.042	2.512	0.043	0.242	5.538
0.011	0.005	0.011	0.021	1.903
0.032	0.005	0.033	0.012	0.375
0.009	0.092	0.009	0.100	11.05
0.066	1.021	0.070	0.123	1.747
0.04	0.005	0.041	0.011	0.266
0.048	1.48	0.050	0.174	3.458
0.176	0.074	0.213	0.020	0.095
0.161	0.428	0.191	0.051	0.266
0.116	3.51	0.131	0.172	1.316
0.12	0.046	0.136	0.019	0.142
0.084	9.56	0.091	0.334	3.652
0.005	0.005	0.005	0.031	6.248
0.002	0.016	0.002	0.088	44.31
0.003	0.005	0.003	0.040	13.47
0.144	0.148	0.168	0.031	0.189
0.035	0.005	0.036	0.011	0.327
0.067	1.251	0.071	0.135	1.889
0.005	30.13	0.005	2.437	485.0
0.096	0.042	0.106	0.020	0.195
0.029	0.167	0.029	0.075	2.522
0.096	0.193	0.106	0.044	0.419
0.014	0.009	0.014	0.025	1.773
0.067	0.036	0.071	0.023	0.320
0.064	0.038	0.068	0.024	0.353
0.086	14.91	0.094	0.413	4.394
0.244	14.79	0.322	0.244	0.757
0.135	7.87	0.156	0.239	1.536
0.186	23.46	0.228	0.352	1.543
0.125	3.207	0.142	0.159	1.113
0.207	5.35	0.261	0.159	0.611
0.272	62.59	0.373	0.476	1.274

0.294	53.19	0.416	0.422	1.014
0.165	4.35	0.197	0.161	0.815
0.032	0.069	0.033	0.046	1.394
0.031	0.534	0.031	0.130	4.073
0.061	1.489	0.064	0.155	2.388
0.002	0.005	0.002	0.049	24.77
0.065	0.026	0.069	0.019	0.285
0.096	0.06	0.106	0.024	0.233
0.164	0.375	0.196	0.047	0.242
0.139	0.586	0.161	0.064	0.399
0.137	0.448	0.158	0.056	0.357
0.108	0.222	0.121	0.045	0.371
0.009	0.938	0.009	0.320	35.29
0.03	0.009	0.030	0.017	0.556
0.06	0.026	0.063	0.020	0.323
0.108	0.005	0.121	0.006	0.055
0.053	0.025	0.055	0.021	0.385
0.079	0.018	0.085	0.014	0.174
0.122	0.889	0.138	0.084	0.610
0.042	0.004	0.043	0.009	0.221
0.046	0.01	0.048	0.014	0.303
0.052	0.205	0.054	0.062	1.136
0.049	0.358	0.051	0.084	1.647
0.072	95.65	0.077	1.144	14.75
0.068	0.005	0.072	0.008	0.116
0.097	0.005	0.107	0.007	0.066
0.085	0.021	0.092	0.015	0.168
0.066	0.005	0.070	0.008	0.122
0.006	0.128	0.006	0.145	24.02
0.002	0.3	0.002	0.384	191.9
0.006	0.008	0.006	0.036	6.006
0.001	0.006	0.001	0.076	76.83
0.007	7.6	0.007	1.034	146.7
0.006	1.264	0.006	0.455	75.50
0.004	0.005	0.004	0.035	8.741
0.05	0.005	0.052	0.009	0.188
0.007	0.005	0.007	0.026	3.764
0.009	0.005	0.009	0.023	2.577
0.011	0.005	0.011	0.021	1.903
0.016	0.009	0.016	0.023	1.448
0.009	0.005	0.009	0.023	2.577
0.008	0.005	0.008	0.024	3.078
0.001	0.005	0.001	0.070	70.14
0.003	0.017	0.003	0.074	24.84

4.2. Log data

In this study, the well log data, especially primary porosity (Recorded by the sonic log), at the corresponding depth of core data, was used to develop a model of matrix permeability. A combination of porosity logs was used, in order to correct for variable lithology effects in the reservoir. Permeability can be estimated from well log data by using suitable empirical relationship which must be calibrated for each hydraulic flow unit to more direct measurement. Predicted permeability was compared with core measured permeability achieved from the core lab database.

(Figure 3) corresponds to log-log plot of RQI against $Ø_z$ for core data of the gas reservoir. This figure shows a scatter plot of permeability versus porosity for core data from all core samples used in this study. The variability porosity and permeability is an evidence of the existence of microscopic-pore level heterogeneity. The scatter of these plots could be attributed to the existence of more than one rock type, with different fluid flow properties. The regression models using classical RQI-Φ_z plot is the simplest analysis, but it is clearly not sufficient to distinguish between different rocks HFU and estimate their boundaries.

5. Determination of HFU by Using Core Data

5.1. Graphical Clustering Method

In order to investigate the variability and continuity of the hydraulic flow units through a set of gathered data, some of the graphical cluster analysis, such as histogram analysis, and probability plot were used. Graphical clustering methods of histogram analysis and probability plot provide a general visual image of a FZI distribution to determine the number of HFU's.

A histogram of FZI (with the log scale on the x-axis) shown in (Figure 4). This figure shows the number of populations based in the number of normal distributions, thus separating the samples in six HFU. Another Graphical Clustering Method is probability plot. A normal probability plot has a specially arranged coordinate system where a normal distribution forms a distinct straight line. Hence, the number of straight lines identifies the number of HFU's. The cumulative probability plot allows picking out at least 6 HFU and estimate FZI boundaries for these rock types (Figure 5). The probability method is more useful than the histogram method because the scatter in the data is reduced on this plot and it is easier to identify straight lines visually.

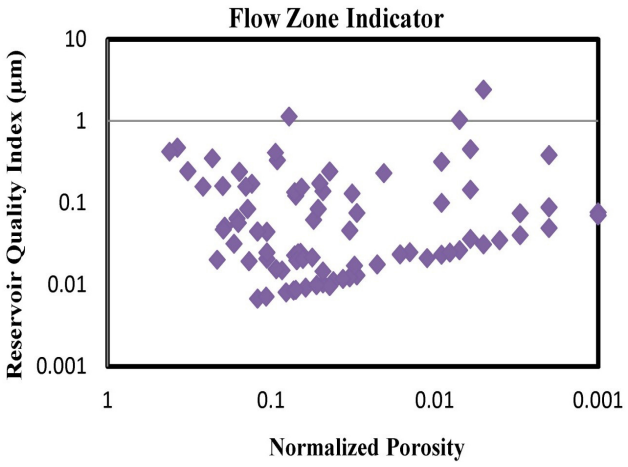

Figure 3: Reservoir Quality Index against Normalized Porosity

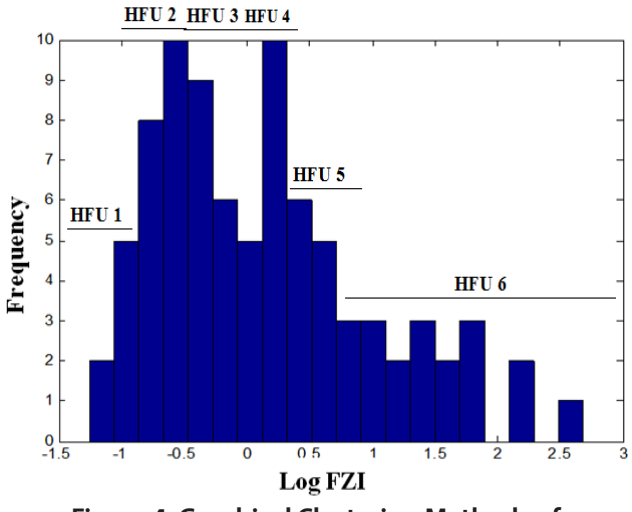

Figure 4: Graphical Clustering Methods of Histogram Analysis

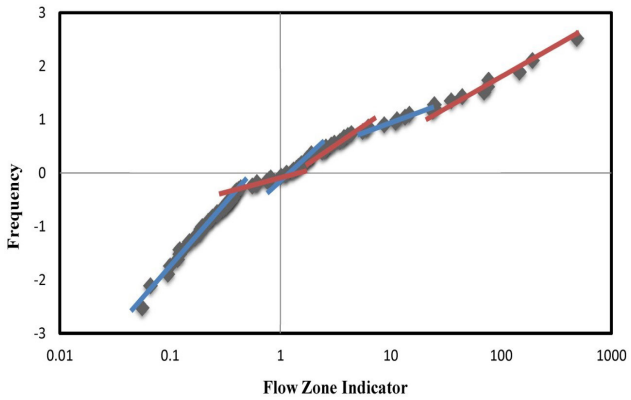

Figure 5: Graphical Clustering Methods of Probability Plot

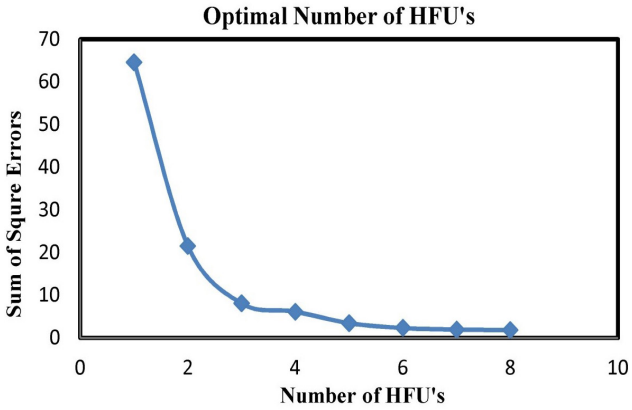

Figure 6: Optimal Number of HFU's by Using SSE

5.2. Graphical Clustering Method

Graphical clustering methods may carry some biased errors because they are based on visual interpretation. Moreover, the overlapped individual distributions and the transition zones between HFU's may cloud the judgment on their identity. The optional number of HFUs that exists in the reservoir can be determined by applying the sum of square method. The proposed method is outlined in the following steps:

1. Compute the values of FZI from equations (4) using the core data.
2. Assume that there exists only one rock type in the reservoir and plot RQI versus $Ø_z$ in logarithmic space and after that calculate the Sum of Square Error.
3. Using K-means clustering analysis for Log (FZI) and decided which data belonged to each unique HFU and consider there are two rock types in the reservoir and computes the SSE's.
4. Increased the number of HFU's in the reservoir by using K-means clustering analysis, until the sum of square error is a minimum for the desired number of HFUs.

By applying the above procedure to core data, the resulting of sum of square error are plotted against number of HFU's in (Figure 6). This figure shows that the optimal number of HFUs is equal to six. This means that six rock types exist in the studied reservoir.

6. Stratigraphic Modified Lorenz Plots

Stratigraphic modified Lorenz plots (Chekani and Kharrat, 2009) is a plot of cumulative flow capacity versus cumulative storage capacity ordered in Stratigraphic sequence. As it is shown in (Figure 7) flow units 1 and 2 have a good porosity and low permeability. Flow units 3 and 6 have a good porosity and high permeability. Flow unit 3 is considered to be the major production zone because of its thickness and permeability while flow unit 2 is a major contribution to the total production. Flow unit 4 and 5 correspond to a very thin and low permeability zones.

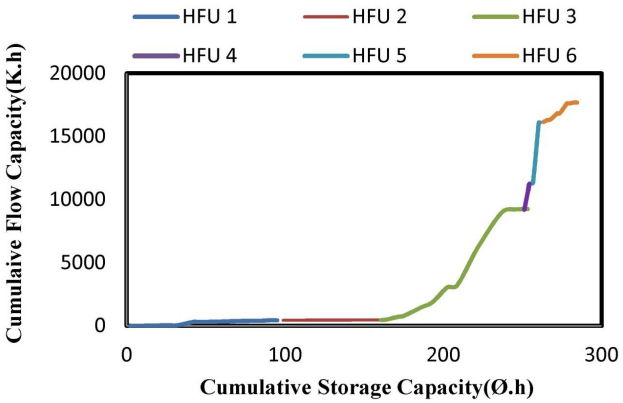

Figure 7: Stratigraphic Modified Lorenz Plots

7. Permeability Modeling

On the basis of the optimal HFU's from the Multi-linear Regression Clustering Technique, a combined RQI versus $Ø_z$ graph is made for all the core data, as shown in (Figure 8). The six

unit slope lines are drawn through segments of data according to mean FZI (Table 2) values calculated for each group of data that belong to the same HFU.

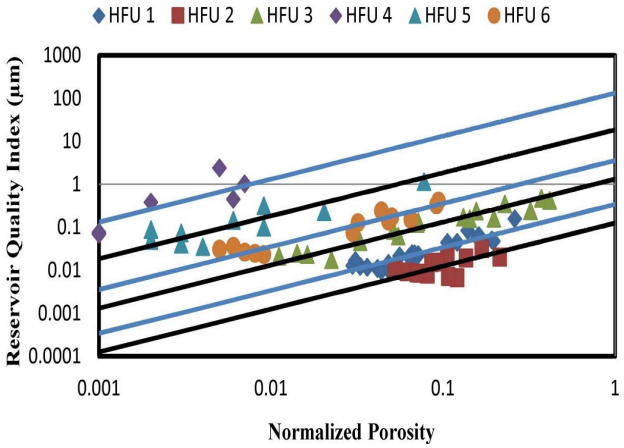

Figure 8: Unit Slope Lines of Six HFU's

Table 2: Mean Flow Zone Indicator for each HFU's

HFU	(FZI) mean
1	0.34
2	0.13
3	1.33
4	133.10
5	18.64
6	3.60

The values of mean FZI (The intercept of unit slops with $Ø_z$ =1) are used to calculate permeability from the following equation (Rearrange Equation 4 with respect to K):

$$K = 1014.(FZI_{mean})^2 \times \frac{\emptyset^3}{(1-\emptyset)^2} \quad (6)$$

To check the permeability model the calculated permeability from core data is plotted against the measured ones in (Figure 9). This cross-plot indicates the closeness of the data to the 45° straight line, and the reliability of the trend and accuracy of the forecast between calculated permeability and the measured ones is equal to 0.933.

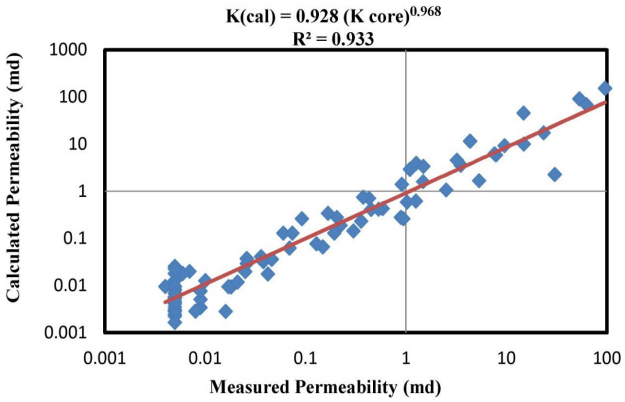

Figure 9: Measured Permeability vs. Calculated Permeability by Using Core Data

8. Predicting Permeability in Un-Cored Wells

The concept of hydraulic flow units must be applied to the wells where only well-log data are available. In this study, the values of mean FZI calculated from core data were correlated with porosity determined from log data, and the evaluation is given in (Figure 10). It indicates a good correlation and the fitted equation is:

$$FZI\ mean = 0.025(Ø_{Log})^{-1.13} \quad (7)$$

Matrix Permeability estimation using the HFU method was extended to un-cored wells by substituting Equation (7) in Equation (6), as follows:

$$K_{Log} = 0.63375 \times \frac{\emptyset_{Log}^{0.74}}{(1-\emptyset_{Log})^2} \quad (8)$$

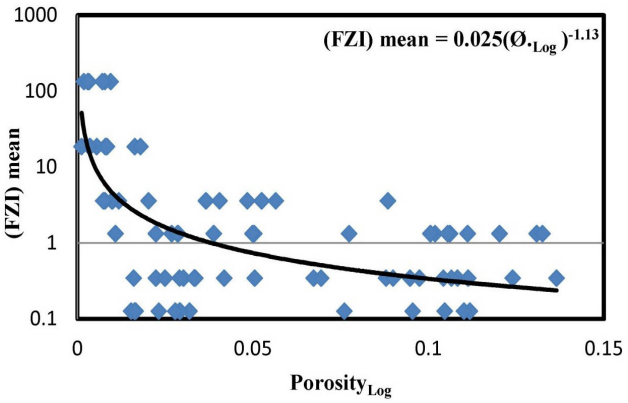

Figure 10: Mean FZI Correlation with Well Log Data

The above equation can be used to estimate the permeability in un-cored wells by using the porosity calculated from well log data at the corresponding depth of core data. To determine the accuracy of Equation (8), it was used to calculate the permeability from well log data and then compared with the corresponding ones of core data. The evaluation is given in (Figure 11). This cross-plot indicates the closeness of the data to the 45° straight line. In addition, the reliability of the trend and accuracy of the forecast between calculated log permeability and the measured ones is equal to 0.589.

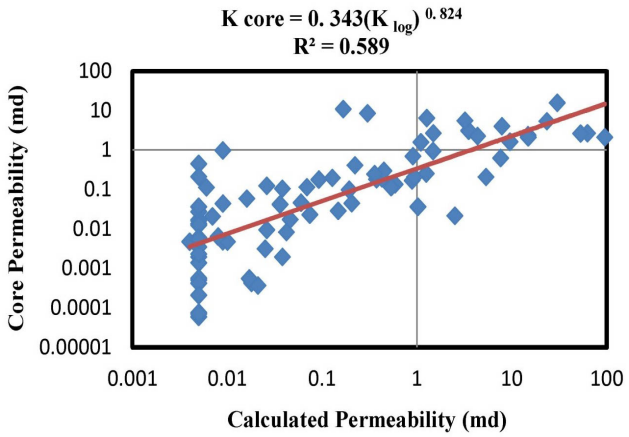

Figure 11: Measured Permeability vs. Calculated Permeability by Using Log Data

9. Conclusion

In this study a technique based on HFU's has been developed that allows for better estimation of permeability in un-cored wells and the following conclusions obtained:

- The results indicate that the permeability profiles of the log-derived HFU agree with core data, and also the R- squared value is 0.59.
- A combination of graphical approaches with regression analysis and analytical clustering methods would be most useful in better delineation of the hydraulic flow units.
- When the number of HFU's increased, the amounts of SSE decreased and by applying an HFU's Approaches to the data of a gas reservoir determine the existence of six flow units.
- Lorenz plot shows that the flow units 3 and 6 have a good porosity and high permeability.

Nomenclature

FZI = Flow Zone Indicator, µm

HFU = Hydraulic Unit, Integer

K = Permeability, mD

RQI = Reservoir Quality Index, µm

Ø = Porosity, Fraction

$Ø_z$ = Pore Volume to Grain Volume Ratio, Fraction

Subscripts

R^2 = Coefficient of Determination

RQI = Reservoir Quality Index

SSE = Sum of Square Errors

Acknowledgment

The authors would like to express their appreciation for the financial support received from the Iranian Central Oil Fields Company.

10. References

1. Abbaszadeh, M.D., Fujimoto, F., 1996 "Permeability Prediction by Hydraulic Flow Units-Theory and Applications", SPE 263-271.
2. Amaefule, J.O., Altunbay, D., Tiab, D., Kersey, D.G., Keelan, D.K., 1993, "Enhanced Reservoir Description: Using Core and Log Data to Identify Hydraulic (Flow) Units and Predict Permeability in Un-cored Intervals/Wells," SPE 26436.
3. Canas, J.A., Malik, Z.A., Wu, C.H., 2000, "Characterization of Flow Units in Sandstone Reservoir: La Cira Field, Colombia, South America; SPE 27732.

4. Chekani, M., Kharrat. R., 2009,"Reservoir Rock Typing in a Carbonate Reservoir-Cooperation of Core and Log Data: Case Study", SPE 123703.
5. Ebanks, W., 1990, "Integrated Approach to Reservoir Description for Engineering Projects, AAPG, Abstract Flow Unit Concept.
6. Elarouci, F., Mokrani, N., 2010, "How to Integrate Wire line Formation Tester, Logs, Core and Well Test Datato Get Hydraulic Flow Unit Permeability's: Application to Algeria Gas Field", SPE 134001.
7. Hatampour, A., Schaffie, M., Jafari, S., 2015, Hydraulic flow units, depositional facies and pore type of Kangan and Dalan Formations, South Pars Gas Field, Iran, Journal of Natural Gas Science and Engineering, 23, 171-183.
8. Iravani, M., Rastegarnia, M., Javani, d., Sanati, A., 2018, Application of Seismic Attribute Technique to estimate the 3D model of Hydraulic Flow Units: A case study of a gas field in Iran, Egyptian Journal of Petroleum, 27, 145-157.
9. Kadkhodaie, R., Rezaee, R., Moussavi, R., 2013, Analysis of the reservoir electrofacies in the framework of hydraulic flow units in the Whicher Range Field, Perth Basin, Western Australia, Journal of Petroleum Science and Engineering, 111, 106-120.
10. Kozeny, J., 1927., UberKapillare Leitung des Wassersim Boden Stizurgsberichte; Royal Academy of Science, Vienna, Proc. Class I, 136, 271-306.
11. Maghsood, A., Fujii, H., Fujimoto, F., 1995, "Permeability Prediction by Hydraulic Units Theory and Application, SPE 30158.
12. Nelson, P.H., 2005. Permeability, porosity, and pore-throat size: a three-dimensional perspective, Petrophysics, v. 46, no. 6, 452-455.
13. Nelson, P.H. 1994. Permeability-porosity relationships in sedimentary rocks, The Log Analyst, v. 3, 38-62.
14. Oliveira, G.P., Roque, W.L., Araújo, E.., 2016, Competitive placement of oil perforation zones in hydraulic flow units from centrality measures, Journal of Petroleum Science and Engineering, 147, 282-291.
15. Saboorian, H., Mowazi, G.H., Jaberi, S.R., 2010, "A New Approach for Rock Typing Used in One of the Iranian Carbonate Reservoir (A Case Study), SPE 131915.
16. Shenawi, Sh., White, J., Elrafie, E., Kilany, KH., 2007, "Permeability and Water Saturation Distribution by Lithologic Facies and Hydraulic Units: A Reservoir Simulation Case Study", SPE 105273.
17. Soto, R., Torres, F., Arango, S., 2001, "Improved Reservoir Permeability Models from Flow Units and Soft Computing Techniques: A Case Study, Suria and Reforma-Libertad Fields", Colombia, SPE 69625.
18. Susilo, A., 2010, "Permeability Prediction Based on Capillary Model", SPE 141122.
19. Williams, S., Batarseh, S., 2010, "Accurate Estimation of in-situ Porosity and Permeability Data Using Cloned Parametric Stressed Models-A Hybrid Approach", SPE 132985.
20. Wyllie, M.R.J., Gardner, G.H.F., 1958 "The Generalized Kozeny-Carmen Equation," World Oil, March and April.

JOURNAL OF GAS TECHNOLOGY

Volume 5 / Issue 1 / Summer 2020 / Pages 32-41

Journal Homepage: http://jgt.irangi.org

General Design Consideration of Cryogenic Air Separation Unit for Esfahan Steel Company

Fereidoon Alikhani Hesari[1*], Abdulla Abdulla[2], Omid Chehregosha[3]

1. Material and Energy Research Center, P. O. Box: 31787/316 Karaj, Iran
2. Acryogenic FZE, P. O. Box: 42271 Sharjah, UAE
3. Electrical Engineering Department, Sharif University of Technology, Tehran, Iran

ARTICLE INFO

ORIGINAL RESEARCH ARTICLE

Article History:
Received: 23 March 2020
Revised: 15 April 2020
Accepted: 19 July 2020

Keywords:
Cryogenic Air Separation
Design Consideration
Purity
Flow Rate

ABSTRACT

Cryogenic air separation unit is integral part of many industrial manufacturing plants like steelmaking, glass, chemical and petrochemicals industries where high purity argon, oxygen and nitrogen are required. Argon, nitrogen and oxygen quality, its production cost and its energy consumption are important parameters in any cryogenic air separation plant design. In this paper, the importance of parameters which used in designing the cryogenic air separation plant are evaluated. Here, in this paper, ESCO, referred to Esfahan steel company in designing cryogenic air separation unit. Products purity is the main issue in every cryogenic air separation plant design. Pressure and temperature variation must be well controlled within cryogenic air separation unit. The annual steel production of ESCO is about 2.5 Mt pre year and it is planned to increase its production to 3.2 Mt by end of 2016. ESCO requires about 300×10^6 Nm^3/y (34300 Nm^3/h) of oxygen for its present steel production. ESCO needs an additional 84×10^6 Nm^3 (9600 Nm^3/h) oxygen for its proposed 0.7 Mt crude steel production increase.

DOR: 20.1001.1.25885596.2020.5.1.3.3

How to cite this article
F. Alikhani Hesari, A. Abdulla, O. Chehregosha. General Design Consideration of Cryogenic Air Separation Unit for Esfahan Steel Company. Journal of Gas Technology. 2020; 5(1): 32 -41. (http://jgt.irangi.org/article_251658.html)

*Corresponding author.
E-mail address: f-a-hesari@merc.ac.ir (F. Alikhani Hesari)

Available online 20 September 2020

1. Introduction

The main constituents of air are nitrogen (78%), oxygen (21%), argon (0.9%) and remaining is carbon dioxide some inert gases. Air impurities are dust, hydrocarbon, water vapor and etc. depend on environmental conditions. Oxygen, nitrogen and argon are used in petrochemical and petroleum refineries, steelmaking, welding, medical treatment, electronic industries, food industries and various other industrial and research applications according to their inherent properties [1]. An air separation unit is an integral part of many industrial manufacturing plants like found in the steelmaking, glass, chemical and petrochemicals industries [2].

Gas purity and flow rate are the main issue in Gas purity and flow rate are the main issue in every air separation plant design for steelmaking plant. For lower volume and purity, the pressure swing absorption and membrane separation (non-cryogenic air separation unit) might be the right choice. Cryogenic air separation units (ASU) are adopted where high purity and large volume of gases are needed. The varying boiling temperatures of the air constituents are the basis for their separation in cryogenic state. The technology of the cryogenic air separation unit has matured during the last 100 years since it is an energy intensive process. Although, an ASU uses air as a raw material but it consumes a tremendous amounts of electrical energy. Therefore, electrical energy is also considered as a raw material. An ASU is operated at cryogenic temperatures of -170 to -195 ºC. Tight energy integration is required for an ASU in order to adjust to changing product demand. The cost of liquid air components is strictly depended on its energy consumption, process design, process operation, manufacturing approach and techniques. All the technical efforts are so far done in reducing plant energy consumption and improving quality of cryogenic ASU products [3].

The cryogenic air separation process has been traditionally adopted for oxygen production in the steel industry. Oxygen purity is one of the key issues. High purity oxygen (above 99.5%) is an essential for basic oxygen steel production application. Purity of oxygen also improves steel quality in electric steel production. Market competition has forced steel authorities to reduce expenses and improve quality. Steel production is an energy intensive industry and needs to improve energy efficient production processes. Steel quality is also improved by improving qualities of raw materials. Cryogenic ASU is a part of an integrated steel plant, which is an energy intensive and product quality management based unit. Therefore, oxygen quality, its production cost and energy use are important in the steel-making industry.

In this paper, the importance of the various parameters that are used in the design of the air separation plant are evaluated. We refer to Esfahan steel company (ESCO) in our discussion in designing air separation unit. Esfahan steel company is the third largest steelmaking plant in Iran, which opened in 1971 with annual capacity of 600,000 Mt. Steel products of ESCO are beams, angles, round bars and channels (constructional steel products) with a production capacity of 3.6Mt. ESCO uses a blast furnace-oxygen convertor method for steel production. ESCO market share of steel production is 95% for iron bars, 20 % for crude steel, 30% for rebar production. ESCO is planning to have new oxygen plant for its steel production [4].

For every ton of steel, on average approximately 120 Nm^3 oxygen is required for the conventional steelmaking procedure [5]. The annual steel production of ESCO is about 2.5 Mt per year and is planned to have production of 3.2 Mt by end of 2016. ESCO requires about $300\times10^6 Nm^3/y$ (34300 Nm^3/h) of oxygen for its current steel production. ESCO needs an additional $84\times10^6 Nm^3$ (9600 Nm^3/h) oxygen for its proposed 0.7 Mt crude steel planned production increase.

For every ton of steel, 80-120 Nm3 of nitrogen (99.99%) is also consumed as a protective gas in various processes involved in steelmaking.

Argon gas is also consumed in steelmaking at about 3 to 4.5 Nm3 per ton of steel as a blowing and protective gas [5].

ESCO has planned to have a cryogenic ASU with 25000 Nm3/h oxygen production capacity for its future plant development. This is about 36 ton/h (864 ton/d). The cryogenic air separation unit is widely used since it is economical in large scale environments and meets the purity requirements of steel plant. This scale of cryogenic ASU is considered to be of medium size and sizes of cryogenic ASU has increased from 100 to 4000 t/d over the years. Basically, ASU is economical for consumption of 100 t/d and above. For a low tonnage consumer, ASU cannot compete due to distillation column scaling down difficulties and small compressor efficiency. Important parameters for technology selection are volume and purities required, customer location, industrial gases usage pattern and infrastructure feasibilities.

2. Process Evaluation

The two main processes for air separation into its components are classified by either cryogenic or non-cryogenic separation systems [6]. The first criteria is to determine the purity and necessary volume of gases. For larger volume gaseous products (above 100t/d), with 95% and above purity, liquid industrial gases and argon recovery, then the process adopted would be cryogenic air separation. ESCO's required volume of oxygen is about 25000 Nm^3/h (864 t/d). The right choice of technology for ESCO is an onsite cryogenic ASU. To design a cryogenic ASU for ESCO, there are various user requirements which has to be known by the vendor. The design of a cryogenic air separation process cycle depends upon users requirements like

How many products are required?

What is the delivery pressure and flow rate of the products?

What should the purities of the products be?

What is cycle load of the products?

What is priorities/ evaluation criteria of the user?

What is the product's flexibility from user point of view?

Appropriate design of cryogenic ASU plant in any industry is required to provide the above information by the user to the designing company. By appropriate adjusting of steps involved in functioning of cryogenic ASU, user's requirements can be maintained.

General steps involved in the functioning of any generic cryogenic ASU are:

1. Compressing air to 5 to 8 bar depending on desired products pressure
2. Cooling of compressed air to remove much of air moisture
3. Further cooling of compressed air below mechanical refrigeration temperature
4. Removal of air impurities like carbon dioxide, residual water vapor, hydrocarbons, dust and etc.
5. Bring air temperature near to cryogenic temperature by use of heat exchanger and waste gas streams
6. Refrigeration of the air by a series of expansion/compression cycles to get to the cryogenic distillation temperature.
7. Separation of the air components in the distillation column at the cryogenic temperature of its components (two high and low pressure distillation columns are used in series, in order to have oxygen as product). Nitrogen is drawn from the top and oxygen drawn from the bottom of each distillation column. Oxygen purity is improved in a second low pressure column. Argon has similar boiling temperature to oxygen and remains as impurity in oxygen. For high purity oxygen, argon is removed at a point in the low pressure column where its concentration is in maximum level in oxygen. Pure argon is produced in an auxiliary unit from crude argon.

8. To produce refrigeration at cryogenic temperatures in streams to compensate for heat leak into the cold box. This is executed by reducing the pressure of streams. This removes energy from gas streams and reduces its temperature more than it would in a simple expansion valve.

Here some design aspects of cryogenic ASU for steelmaking plant are reviewed.

3. Required Products

It is important to know how many gaseous products are needed since the basic technology is decided on the required number gaseous products. If the technology choice is cryogenic separation even though number of products are directly influenced design and cost of ASU plant. Argon generally fractionates between oxygen and nitrogen in an ASU plant and is economically produced as a co-product with oxygen. If it is desired to have argon as a third product then an additional distillation column is added to the ASU to separate argon from nitrogen and oxygen rich streams. The choice is between production of nitrogen and oxygen, where plants for production of nitrogen are less complex and use lower electrical energy than plants with only production of oxygen gas. ESCO uses a blast furnace-oxygen convertor method for steel production therefore all three industrial gases oxygen, nitrogen and argon are required. In a blast furnace-oxygen convertor, oxygen is the main gas used in steelmaking.

In general, only a pure nitrogen producing plant is less complex and low energy consuming than a pure oxygen producing plant. Having both nitrogen and oxygen in a co-production plant requires more capital and operational investment. This type of co-producing plant is more energy intensive than a single component producing plant. Separating air components into their liquid form is also required, which doubles the amount of energy per unit of delivered products [7].

4. Delivery Pressure and Flow Rate of Products

In a steelmaking plant oxygen availability must deliver 120 $Nm^3$for every ton of steel in conventional steelmaking. The rate of delivery should be 200 to 710 (or above) Nm^3 per minute at pressure of above 1.5 to 15 bar. Pressure and the flow rate of oxygen should be varied in order to attain sonic and supersonic velocities in the blast furnace.

Large gaseous volumes are only generated from cryogenic air separation units. The cryogenic air separation process is the most adopted process for medium to large scale steel production unit. There are peak hours, seasons and or shut down periods in a round-the-clock steel plant operations. Variation in the supply of industrial gases in a steel plant must have been considered and hence making and storing gases in liquid form need additional equipment and engineering design sophistication. This doubles the required energy per unit of gas delivery. For 50 t/d delivery and above, the most preferred and economically sound method is cryogenic ASU. An ASU plant is almost exclusively use for 100 t/d delivery of industrial gases.

For every ton of liquid oxygen about 3 tons of liquid nitrogen and smaller amounts of argon (as a byproduct) are produced. The ESCO required volume of oxygen is about 25,000 Nm^3/h (864 t/d). The volume of produce nitrogen is about 75,000 Nm^3/h (2,592 t/d). This amount of liquid nitrogen is certainly more than the requirement of ESCO. A plan should be considered for liquid nitrogen storage and supply to other industries. It is estimated about 282 t/d argon is also produced. It should be planned in such a way to keep a portion as back-up liquid gas storage for 2-4 days.

In a cryogenic ASU plant, excess nitrogen is inevitability produced since there is four times as much as nitrogen than oxygen in air composition. Some of the excess nitrogen is used to cool incoming air but for the rest additional liquefiers at plant need to be considered.

In common ASU's, oxygen is produced slightly above atmospheric pressure in a cryogenic distillation column. In the double column cycle, 6 bar compressed air is cooled to near its dew point and feeds into the bottom of column at high pressure. Nitrogen evaporates first and rises to top of the column. By use of a re-boiler/ condenser the top column vapor nitrogen is condensed against incoming liquid oxygen. Condensed overhead nitrogen is divided into two reflux streams, partially to return to the high pressure column and partially to the top of low pressure column. High pressure column oxygen is sent to an intermediate stage of the low pressure column and oxygen accumulates at the bottom of low pressure column [8].

As the pressure of delivery gases are increased, cost of ASU plants is also increased. It is important to have trade-offs among parameters like capital cost, process simplicity, required gaseous products pressure and so on. Compressing oxygen and nitrogen to the required pressure can be expensive. In a GOX process, oxygen is removed from the bottom of the low pressure column as vapor and used to cool entering air. In a high pressure product, oxygen should further compressed.

It is well understood that low pressure ASU products are less expensive in terms of operating and capital cost. Gaseous oxygen and nitrogen can be produced in different process cycles from above atmospheric pressure at up to 8 bar pressure without using compressor.

In order to meet a steelmaking plant's high pressure oxygen requirement, a pumped LOX cycle is generally utilized to produce oxygen at an elevated pressure directly from the cold box instead of using oxygen compressor. A portion of liquid oxygen is pumped from low pressure column at an elevated pressure and warmed against a high pressure air feed to an ambient temperature.

5. Purities of Products

Purity is also one of the key factors in industrial plant evaluation. For a product purity above 95%, cryogenic ASU is adopted. Non-cryogenic technologies produce oxygen and nitrogen to a maximum of 95% purity and hence non-cryogenic technologies may be economical for gaseous products of 90 to 93% purity. The level of output purity has its own impact on the cost of process energy consumption. At a higher energy consumption, purity of ASU products can be improved. Therefore, purity of ASU products has one of the factors that are considered for cost of energy consumption. For a conventional ASU with a 99.5% oxygen purity about 0.35 kWh energy is consumed per Nm^3 of oxygen. Optimal purity of oxygen is increased as pressure increases. Purity of oxygen is determining factor in power consumption of ASU plant.

From other point of view, argon has boiling point between oxygen and nitrogen with a lesser relative volatility than nitrogen. This makes a major difference in separating pure oxygen (above 97%) from impure oxygen (less than 97%). In other words for 97% and above oxygen purity, all nitrogen should be stripped out of the low pressure column and then argon can separate from oxygen. In a simple double column ASU, the number of separating stages is increased from 35 to 60 to improve purity of oxygen from 95 to 99.6%. Increasing the number of separating stages in the distillation column for oxygen recovery must be compensated by increasing the discharge pressure of the air compressor to the distillation column. Therefore, careful optimization is required for each specific design case.

6. Air Quality

For the safe design of an ASU the quality of air must be known. Air conditions and air trace components should be recorded and provided to ASU supplier. Air impurities can cause process problems like reaction, plugging and corrosion. Carbon dioxide, Sulfur dioxide, water vapor, N_2O and NO_x cause plugging due to liquefaction

in the system. Sulfur dioxide and HCL cause corrosion in system. All hydrocarbons, ozone and NO_x react with system components. A seasonal survey of air condition can give the appropriate air quality information to a supplier for proper ASU design since a four season climate conditions exist in most plant locations. Measuring air impurities and quality should done over a long term period but accurate analysis of air quality and compositions can be difficult. Quality of air may also change due to changes in neighboring areas or changes in wind the condition and direction. A correct estimation of air quality requires long term site survey (considering neighboring areas, any intermittent or normal vents, wind direction and speed). Care must be taken with any direct air measurements. Furthermore, care must be taken to have a long enough test of air quality and compositions with precise and high sensitivity instruments. A site survey may not be practically sound in many cases as it is a time consuming procedure. In this case for design propose, higher values are considered for conservative design basis.

The water vapor content of the inlet air varies with atmospheric temperature and elevation above sea level. In an ASU plant the byproduct streams of oxygen, nitrogen and argon are produced at any purity either in gaseous or liquid form [9].

7. Power Used

The main aim of designing any cryogenic ASU is to minimize operating costs which include cost of electricity and other operating parameters. Cost of electricity is the main issue in ant cryogenic ASU. One possible way is to go for oversize plant of the required production capacity in order to meet major customer demand by producing only during off peak hours since electricity cost in off peak hours is reduced to one third of its price during peak hours.

In this case, we should consider an ASU plant with capacity of 864 t/d oxygen with above 99% purity. The average kWh electrical energy cost is considered to be about 6 cents ($0.06) based on a peak hour's tariff rate including tax and other expenses.

The most important performance parameter in design and operation of any cryogenic ASU is the overall oxygen specific energy which is the ratio of total power consumption in kW to total oxygen production Nm^3/hr.

Practically, it may vary from unit to unit of same capacity. Castel [10] forecasted the oxygen specific energy for cryogenic ASU based on technological forecasting reach of 0.28 ~ 0.3 kWh/Nm^3 in 2010 using extraplotted method. Castel's forecast was later confirmed by Pafaffand Kather [11] and proposed 0.25 to 0.28 kWh/Nm^3 oxygen specific energy for any up to date ASU plant.

According to the Linde engineering group, the energy consumption in a conventional ASU plant is about 0.35 kWh/ Nm^3 (245 kWh/t) of liquid oxygen with 99% purity. This number in an advanced optimized ASU plant is about 0.25 kWh/ Nm^3 (175 kWh/t) of liquid oxygen with 95% purity. According to Air Liquid group improved ASU plant, oxygen specific energy consumption is about 0.23 kWh/ Nm^3 (160 kWh/t). Oxygen specific energy consumption (kWh/Nm^3) has been improved from 0.65 to 0.25 kWh/Nm^3 since 1960 as production capacity of plants have also been increased.

According to our calculation, it is logical to consider oxygen specific energy consumption (kWh/Nm^3) as 0.38 since it is planned to have a stock or second hand refurbish cryogenic ASU after 2003. If ASU technology is taken from the Linde group, Air Liquid Co. and Air Products group, it is possible to have an oxygen specific energy consumption below 0.3 (kWh/Nm^3). On the other hand, fixed capital investment will be higher and most important point is that it may not possible to have direct deal with these leading ASU manufacture.

Based on 0.38 kWh/Nm^3 oxygen specific power (0.38 kWh energy is required for every 1 Nm^3 of oxygen production), 9500 kWh of energy

is required for 25000 Nm^3 oxygen.

A total of 228,000 kWh energy will be consumed for 864 t of oxygen per day. The total energy consumption per year will be 83,220,000 kWh. Total energy required and estimated cost of energy required are given in Table 1.

Table1: Energy consumption based on theoretical (0.38 kW/Nm^3) oxygen specific power

Required capacity of oxygen	Energy consumption for oxygen production based on theoretical 0.38 kWh/Nm^3)oxygen specific energy consumption	Cost of energy $0.06/kWhr
25,000 Nm^3	9500 kWh	$570
36 t/h	9500 kWh	$570
864 t/d	228,000 kWh per day	$13680
315,360 t/y	83,220,000 kWh per year	$4,993,200

It is estimated the oxygen production cost per ton will turn up to be about $15.83. Most of the energy is consumed by the compressor and the expander in a cryogenic ASU plant.

The estimated energy cost for one ton of oxygen is about $15.8. In reality, these values can be checked against real values which are obtained from a working plant to find out the power loss. Comparison of theoretical oxygen specific power consumption with obtained oxygen specific power consumption from any plant gives a degree of cost effectiveness. By utilizing a proper controlling system in an ASU plant, one can push the ASU plant oxygen specific power consumption to the theoretical value.

Liquids production should be planned to operate at hours that electricity price is lowest (overnight, weekends, not in peak hours). A close cooperation should be arrange between the ASU plant management and the electricity supplier during peak hours in summer months. Improving the expander efficiency of any cryogenic ASU unit can be directly linked to oxygen production efficiency. It is estimated that every expander refrigeration kW decrease there can be a saving of 5 kW of electricity.

Using a type of predictive control model, one can maximize high pressure product production in high pressure distillation column and total product recovery while reducing operating cost. A suitable predictive control model can keep the right balance among operating parameters of an ASU plant to minimize power consumption (90% of operating cost) at maximum product rate [12]. Therefore, correct evaluation of plant parameters can help to maximize plant life and asset profit potential.

Power consumption can be minimize in basic double column cryogenic ASU by

1. To reduce pressure drop in heat exchanger by increasing its size
2. To reduce temperature difference between boiling oxygen and condensing nitrogen by increasing reboiler condenser size
3. Reducing pressure drop in two distillation column by using structured packing
4. Less pure oxygen to reduce number of separating stages in distillation column
5. Appropriate design of basic components ASU like compressor, air purifier, heat exchanger, distillation column.

8. Cost Estimation

All improvements made to the cryogenic air separation unit were, so far, to reduce cost and improve reliability and flexibility [8]. From the point of view, the challenge for any industry is to manage peaks and drops of the macro-economic situation in order to make right investment decision. It is globally understood

that to make an investment at the bottom of an economic cycle is better than those at top if done in a carefully conceived, developed and well-executed manner.

For an operating cost estimation, direct costs should be calculated first. Items that come under the direct cost is power cost, cooling water cost, payroll overhead cost (20 -27% of payroll cost), supervision cost (15% of direct labor cost), plant maintenance cost (3-7 % of investment), operating supplies (20 -25% of plant maintenance cost).

Indirect cost should be taken as 40% of direct labor, plant maintenance and the operating supplies cost.

Fixed cost are taxes and insurance (2-3% of investment cost) and depreciation cost (6-10% of investment cost).

Total annual operating cost is the sum of the direct cost, indirect cost and fixed cost. The production cost of oxygen ($/ton of oxygen) is the ratio of the total annual operating cost to annual production of oxygen.

Production cost of oxygen ($/ton of oxygen) = (total annual operating cost) / (annual production of oxygen)

A discounted cash flow (DCF) is used as a valuation method to estimate the attractiveness of an investment opportunity. DCF analysis uses future free cash flow projections and discounts them to arrive at a present value estimate, which is used to evaluate the potential for investment.

The profit return of total capital investment of a plant is calculated by taking the ratio of capital investment (P) to return profit (R) from giving relation (1) where n is the life of plant and the interest rate total investment per year

$$P/R = [(1+i)^n - 1] / [i(1+i)^n] \quad (1)$$

Return profit (R) is then

$$R = P[i(1+i)^n] / [(1+i)^n - 1] \quad (2)$$

Net profit (N) is

Net profit (N) = Return profit (R) - Depreciation cost (6-10% of investment cost)

Gross profit (G) is the profit a company makes after deducting the costs associated with making and selling its products, or the costs associated with providing its services. Considering governmental income tax is from 25 to 50% of net profit (here is assumed 50% governmental income tax)

$$\text{Gross profit (G)} = 2 \times \text{Net profit (N)} \quad (3)$$

Sales (S) is calculate as;

Sales (S) =Gross profit (G) + total annual operating cost

Selling price of oxygen ($ / ton of oxygen) = Sales (S) / annual production of oxygen

Now, it can back calculate to find out Net profit (N) of oxygen sales in a year

Total Sales (S) = annual oxygen production (t/y)× selling price of oxygen ($ / ton of oxygen)

Gross profit (G) = Total Sales (S) - total annual operating cost

Net profit (N) = Total Sales (S) - total annual operating cost - Gross profit (G) - Income tax revenue

Total positive cash flow (F) = depreciation cost (6-10% of investment cost) + Net profit (N)

Operating cash flow is important because it indicates whether a company is able to generate sufficient positive cash flow to maintain and grow its operations, otherwise it may require external financing.

There are alternative methodologies that can supplement the discounted cash flow (DCF) approach to analyze the projected economic situation.

9. Safety Aspects

ASU plant operation has some hazards that are associated with gases being ventilated into the atmosphere, such as:

-
- Asphyxiation (nitrogen and argon)
- Enhanced fire risk (oxygen)
- Cold and low visibility (cryogenic gases and liquids)
- Hot gases (e.g., compressor inter-stage relief/discharge gas vents)

These hazards must be controlled at the plant site. The gas exit velocity of warmed gases is also important at the warm-end of an ASU. Noise and odor levels should be at permitted acceptable levels.

10. Conclusion

Although oxygen production by cryogenic distillation of air is a commercially matured process, there have been many improvements over the time that has resulted in significant reduction in the specific oxygen production power and the trend is expected to continue in the future. ESCO has planned to have a cryogenic ASU oxygen of 25000 Nm^3/h capacity for its future plant development. This is about 36 ton/h (864 ton/d). The most important performance parameter is the overall oxygen specific energy which is the ratio of total power consumption in kW to total oxygen production Nm^3/hr. The overall oxygen specific energy is considered to be 0.38 for a refurbish cryogenic ASU plant which match oxygen requirement. It is estimated the oxygen production cost per ton will turn up to be about $15.83. Cryogenic ASUs become cost effective at the level of about 200-300 tons/d oxygen. Most efficient and reliable unit are above 500 to over 2,000 ton /d. Refurbish cryogenic ASU mechanical characteristic should be able to accommodate system efficiency variation with system flexibility in acceptable range. Ambient temperature and pressure and temperature fluctuations are major source of instability in ASU plant caused by front end of cleaning system sequencing. Design for high peak efficiency in ASU plant may easily scarify flow rates change ability in compressor and expander. Therefore for an excellent paper design efficiency, one must run the plant on single point. It becomes extremely difficult to accommodate pressure and temperature fluctuation in such plant therefore ASU plant should always run below paper design efficiency in order to accommodate pressure and temperature fluctuation.

11. References

[1] A. K. Firat, W. L. Woon, and S. Madnick, "Technological forecasting-A review," Massachusetts Institute of Technology, Cambridge, USA, Working Paper CISL# 2008-15.

[2] Air Products (2005b). Gases and equipment online fact book, http://www. airproducts. com/Products/fast facts/factbook.htm

[3] Air Separation Unit (Engineering Design Guidelines) KLM TECHNOLOGY GROUP, Jan 2013.

[4] The Basic Oxygen Steelmaking (BOS) Process, John Stubbles, Steel Industry Consultant, STEELWORKS, American Iron and Steel Institute.

[5] Xiao-bin Zhang, Jian-ye Cheng, Lei Yao, Yong-hua Huang, Xue-jun Zhang, Li-min Qiu, Research and development of large-scale cryogenic air separation in China, Journal of Zhejiang University-SCIENCE A (Apply Physic & Eng.), vol. 15(5) (2014), 309-322.

[6] Cryogenics and Ceramic Membranes: Current and Future Technologies for Oxygen Supply in Gasification Systems, Gasification for the Future, 4th European Gasification Conference, April, Noordwijk, Netherlands,

2000.

[7] Cryogenic Air Separation: History and technological progress, http:// www.linde-engineering.com.

[8] A. R. Smith, J. Klosek: A review of air separation technologies and their integration with energy conversion processes, Fuel Processing Technology, vol. 70(2001), 115 -134.

[9] S. S. Amarkhail: Air Separation (diploma work), in the frame work of the project No. SAMRS 2009/09/02, Slovak University of Technology, Bratislava 2010.

[10] W. F. Castle, "Air separation and liquefaction: Recent developments and prospects for the beginning of the new millennium," International Journal of Refrigeration, vol. 25 (2002), pp. 158-172.

[11] I. Pfaff and A. Kather, Comparative Thermodynamic analysis and integration issues of CCS steam power plants based on oxy-combustion with cryogenic or membrane based air separation," Energy Procedia Journal, vol. 1 (2009), pp. 495-502.

[12] D. R. Vinson, "Air separation control technology," Computers and Chemical Engineering, vol. 30 (2006), pp. 1436-1446.

JOURNAL OF GAS TECHNOLOGY

Volume 5 / Issue 1 / Summer 2020 / Pages 42-51

Journal Homepage: http://jgt.irangi.org

Intensification of liquid fuel production using Nano Fe Catalyst in GTL process

Mohammad Irani[1*], Asghar Alizadehdakhel[2] , Yahya Zamani[1]

1. Research Institute of Petroleum Industry (RIPI), Tehran, Iran
2. Rasht Branch, Islamic Azad, Rasht, Iran

ARTICLE INFO

ORIGINAL RESEARCH ARTICLE

Article History:
Received: 24 April 2020
Revised: 23 June 2020
Accepted: 11 August 2020

Keywords:
Fischer-Tropsch Synthesis
GTL
Fixed bed reactor
Nano Fe Catalyst
CFD

ABSTRACT

An experimental and computational fluid dynamic (CFD) investigation was carried out to intensify the production of gasoline in a bench-scale Fischer-Tropsch Synthesis (FTS) process. A cylindrical reactor with one preheating and one reaction zone was employed. The reactor temperature was controlled using a heat jacket around the reactor's wall and dilution of the catalyst in the entrance of the reaction zone. An axi-symmetric CFD model was developed and the non-ideality of the gas mixture was considered using Peng-Robinson equation of state. A kinetic model based on 25 chemical species and 23 reactions was utilized. The model validated against experimental measurements and the validated model employed to investigate the effects of operating conditions on the performance of the reactor. The optimum values of operating conditions including pressure, reactor temperature, GHSV and H_2/CO ratio were determined for maximum reactor performance.

DOR: 20.1001.1.25885596.2020.5.1.4.4

How to cite this article
M. Irani, A. Alizadehdakhel, Y. Zamani. Intensification of liquid fuel production using Nano Fe Catalyst in GTL process. Journal of Gas Technology. 2020; 5(1): 42 -51. (http://www.jgt.irangi.org/article_251659.html)

*Corresponding author.
E-mail address: iranim@ripi.ir (M. Irani)

Available online 20 September 2020

1. Introduction

The conversion of syngas (CO + H_2 mixtures) into liquid fuels via Fischer-Tropsch synthesis (FTS) has attracted much attention in the recent years. The increase in global energy demand, existence of numerous gas reservoirs in remote areas and the high price of crude oil in comparison with natural gas, are the main reasons of the increasing attention to FTS. In addition, converting of associated gases is appealing due to economic and environmental reasons. Also, GTL products are almost free of sulfur and aromatic hydrocarbons. Composition of the obtained products depends on the employed catalysts and operating conditions [1,2]. Numerous researches have been carried out to understand, model and optimize this process. Butt et al. [3] prepared and characterized Fe and Fe-Co catalysts on ZSM-5 support for FTS. Schulz et al [4] investigated the selective conversion of syngas to gasoline on iron/HZSM5 catalysts. The effects of temperature, space velocity, CO/H_2 feed ratio and pressure on the activity of a Co/HZSM5 zeolite bifunctional catalyst were experimentally investigated by Calleja et al [5]. The fixed-bed FT process, is one of the most competing reactor technologies and occupies a special position in FTS industrial processes [6]. Liu et al [7] developed a two-dimensional heterogeneous model for simulation of steady and unsteady behavior of a fixed bed FTS reactor. They also reported [8] the effects of feed temperature, flow rate and wall temperature on the steady state behavior of the reactor. Wang et al [9] developed a one-dimensional heterogeneous model to predict the performance of fixed-bed Fischer-Tropsch reactors. Rahimpour et al [10] proposed a novel combination of fixed-bed and slurry bubble column membrane reactor for Fischer-Tropsch synthesis. In the first catalyst bed, the synthesis gas was partially converted to hydrocarbons in a water-cooled fixed bed reactor. In the second bed which was a membrane assisted slurry bubble column reactor, the heat of reaction was used to preheat the feed synthesis gas to the first reactor. The membrane concept was suggested to control hydrogen addition. They utilized a one-dimensional packed-bed model for simulation of fixed-bed reactor. A one-dimensional model with plug flow pattern for gas phase and an axial dispersion pattern for liquid-solid suspension was used for modeling of slurry bubble column reactor. They claimed that their proposed reactor system gives favorable temperature profile and higher, gasoline yield, H_2 and CO conversion as well as selectivity. However, they admitted that experimental proof of concept is needed to establish the validity and safe operation of the proposed reactor. Nakhaei Pour et al [11] developed a kinetic model for water-gas-shift (WGS) reaction over a Fe/Cu/La/Si catalyst under Fischer-Tropsch synthesis (FTS) reaction condition. By comparing the results of four different models over a wide range of reaction conditions, they found that WGS rate expressions based on the format mechanism best fit the experimental data. Although the reaction scheme has been studied and used for a long time, its study today is still of interest because of the high pressure on hydrocarbons prices all over the planet. In the recent years, by the high speed of computational calculations, Computational Fluid Dynamics (CFD) techniques have become a useful tool for simulation and analysis of variety of industrial problems that deal with fluid flow [12-14], heat and mass transfer [15,16] and chemical reactions[17, 18]. By predicting a system's performance in various conditions, CFD can potentially be used to improve the efficiency of existing units as well as the design of new systems. It can help to shorten product and process development cycles, optimize processes in order to improve energy efficiency and environmental performance, and solve problems as they arise in plant operations. However, it is essential to validate the CFD results against data obtained from real operating systems. Krishna and Van Baten [19 and 20] employed CFD technique for describing hydrodynamics of bubble column reactors and its effects on scaling up this type

of reactors. Jiang et al [21] used a CFD approach for obtaining the detailed flow field and bubble behaviors in a novel two-stage fluidized bed reactor which was designed to produce diethyl oxalate from carbon monoxide based on the catalytic coupling reaction. A FTS microchannel reactor was modeled in three-dimensions by Arzamendi et al [22]. They utilize a CFD model to analyze the effects of feed and cooling water flow rates and pressure on the performance of the reactor. In our previous work, FTS fixed bed reactor based on Iron-zeolite catalyst was studied and the use of saturated water for absorbing the heat of reaction was investigated. It was concluded that the temperature run away was controlled by utilizing saturated water, and the maximum temperature rising within the catalyst bed was 16K [23]. In the present work, a CFD model was developed to model FTS in a fixed bed nano-iron catalyst reactor. The catalyst bed was diluted in the entrance region of the bed in order to prevent hot spots. Thermodynamics properties of the gas mixture were calculated using Peng-Robinson equation of state [24]. The model predictions were validated with measured data and the effect of operating conditions on performance of the reactor were analyzed.

2. Material and Methods

2.1. Process description

The employed reactor was a 1.2 cm diameter cylindrical reactor which was placed inside a heating jacket (Figure 1). The reactor included a preheating zone with 30cm height following by a reaction zone with 50cm height. It was designed and constructed by the Research Institute of Petroleum Industry, National Iranian Oil Company (RIPI-NIOC) in 2010 [25]. The reactor was packed with cylindrical Fe-Sio2 catalysts (atomic ratios: 100Fe/5.64Cu/2La/19Si) with average diameter and length of 0.3 mm and 0.9 mm, respectively. Particle and bulk densities of the catalyst were 1290 and 730 kg/m^3, respectively. Entrance region of the reaction section was diluted using ceramic particles in order to prevent the creation of hot spot.

Figure 1. FTS fixed-bed reactor used for experiments

The experiments were run at different conditions of feed temperature, pressure, GHSV and H_2/CO ratio as given in table 1.a

Table1. Operating conditions

Feed Temperature(K)	543,563, 583 and 603
Reactor pressure(bar)	13,17,21 and 25
GHSV(hr $^{-1}$)	1800, 5500,11000 and 15000
H_2/CO molar ratio	0.5, 1,1.5 and 2

2.2. CFD Modeling

2.2.1. Geometry and solution strategy

The reactor was modeled using a 1.2 cm × 80 cm axi-symmetric model. The computational domain was divided into 22,016 rectangular meshes and the predicted profiles of temperature and species mole fractions were checked to be independent of the mesh size. The packed bed was considered as a porous

media due to the large value of tube to catalyst diameter ratio (N>12) [26].

The entrance region of the reaction zone was considered as diluted reaction zone and the reaction rates in this zone were multiplied by catalyst/ (catalyst + ceramic) ratio. Mass-flow-inlet and pressure-outlet boundary conditions were used for reactor inlet and outlet, respectively. Constant temperature and no-slip conditions were employed for the reactor walls. The finite volume method was used to discretize the partial differential equations of the model. The SIMPLE algorithm was employed for pressure-velocity coupling. The convergence criterion was based on the residual value of the calculated variables, namely mass, velocity components, energy and species mass fractions. In the present calculations, the numerical computation was considered to be converged when the scaled residuals of the different variables were lower than 10^{-4} for continuity and momentum equations and 10^{-7} for the other variables.

2.2.2. Conservation equations

The mass conservation, momentum, energy and species, can be expressed as:

Mass: $\nabla.(\vec{v}\rho\ ) = 0$ (1)

Momentum: $\nabla.(\rho\vec{v}\vec{v}) = -\nabla P + \nabla.\left[\mu\left(\nabla\vec{v} + \nabla\vec{v}^{T}\right)\right] + \rho g + S$ (2)

Energy: $\nabla.(\vec{v}(\rho\ H\ + P)) + \nabla.(\sum_{i=1}^{n} h_i j_i) = -\nabla.(q) + S_R$ (3)

Species: $\nabla.(\vec{v}C_i - D_i\nabla C_i) = R_i$ (4)

Where, ρ represents mixture density, $\vec{v}$ is velocity vector, H and hi are total enthalpy and enthalpy of species, respectively. P is the static pressure and C_i stands for concentration of chemical species. The porous media of the reaction zone was modeled by addition of a momentum source term:

$$S = -\left(\sum_{j=1}^{2} D_{ij}\mu v_j + \sum_{j=1}^{2} C_{ij}\frac{1}{2}\rho|v|v_j\right) \quad (5)$$

The first term on the right-hand side of equation 5 is the viscous loss term and the second term is the inertial loss term. $|v|$ is the magnitude of the velocity and D and C are prescribed matrices. In this work, flow in the reactor is laminar; therefore, the inertial term was ignored [27]. (FLUENT 6 User manual). S_R in equation (3) is the source of energy due to chemical reaction:

$$S_R = -\left(\sum_j \frac{h_j^0}{M_j} R_j\right) \quad (6)$$

2.2.3. Physical properties

Peng-Robinson equation of state was used to predict the non-ideality [16]of the gas mixture:

$$\ln\tilde{\varphi}_i = (Z-1)\frac{b_i}{b_m} - \ln(Z-beta) - I\bar{q}_i \ ,\ q = \frac{a}{bRT} \ ,\ \bar{q}_i = q\left(2.\times\frac{\frac{\partial a}{\partial x_i}}{a} - \frac{b_i[i]}{b}\right)$$

$$I = \frac{1}{\varepsilon_1 - \varepsilon_2}\ln\left(\frac{Z+\varepsilon_1\times beta}{Z+\varepsilon_2\times beta}\right) \ ,\ beta = \frac{bP}{RT} \ ,\ f_i = \tilde{\varphi}_i\times P\times y_i \quad (7)$$

Where, f_i is species fugacity, R is the universal gas constant, MG is the molecular weight of gas mixture and P is the operating pressure (taken to be 17 bar). Z is the compressibility factor for calculation of the mixture density:

$$\rho = \frac{PM}{Z\,R\,T} \quad (8)$$

The parameters of equation (7) are listed in table 2. The specific heat of each species was defined as piecewise-polynomial function of temperature. Other thermal properties of the mixture such as molecular viscosity, thermal conductivity and diffusivity coefficient were calculated from Poling et al [28].

Table 2. Parameters of Peng-Robinson EOS

ε_1	ε_2	Ω	Ψ
$1+\sqrt{2}$	$1-\sqrt{2}$	0.07779	0.45724

$$Z^3-(1-B)Z^2+(A-2B-3B^2)Z-(AB-B^2-B^3)=0$$

$$A=\frac{aP}{(RT)^2}\ ,B=\frac{bP}{RT}$$

$$a=\sum_{i=1}^{n}\sum_{j=1}^{n}x_i x_j(a_i a_j)^{0.5}(1-k_{ij})\ ,\quad b=\sum_{i=1}^{n}x_i b_i$$

$$a_i=a_{ci}\alpha_i\ ,\ a_{ci}=\Psi\frac{(RT_{Ci})^2}{P_{Ci}}\ ,\ b_i=\Omega\frac{(RT_{Ci})}{P_{Ci}}$$

$$\alpha_i=\left[1+(0.37464+1.54226\omega-0.26992\omega^2)(1-T_r)^{0.5}\right]^2$$

2.2.4. Reaction rate expressions

The considered reactions with 25 chemical species including CO, H_2, CO_2, H_2O and C_1-C_{21} are listed in Table 3. The general form of rate equations [25] for production of C_i is expressed as:

$$R_{C_1}=.001518*f_{H2}^{\ 0.241}/f_{CO}^{0.241} \tag{10}$$

$$R_{C_2}=.01819*f_{H2}^{\ 0.045}/f_{CO}^{0.045} \tag{11}$$

$$R_{C_3}=0.025f_{H2}^{0.1}f_{CO}^{-0.8} \tag{12}$$

$$R_{C_i}=\frac{0.025f_{H2}^{0.1}f_{CO}^{-0.8}}{(2.03-0.14f_{H2}f_{CO}^{-1})^{i-1}}\quad i=4\text{-}9 \tag{13}$$

$$R_{C_{10}}=5e-5f_{H2}^{1.8}f_{CO}^{-1.1} \tag{14}$$

$$R_{C_i}=\frac{5e-5f_{H2}^{1.8}f_{CO}^{-1.1}}{(1.16-0.089f_{H2}f_{CO}^{-1})^{i-1}}\quad i=11\text{-}22 \tag{15}$$

Table 3. list of FTS reactions

Reaction Number	Reaction Stoichiometry
1-22	$nCO+(n+1)H_2\rightarrow C_nH_{2n+2}+nH_2O$, n = 1-22
23	$CO+H_2O\rightarrow CO_2+H_2$

Reaction (23) is known as water-gas-shift (WGS) reaction and its rate [11] can be expressed as:

$$R_{WGS}=\frac{k_w\left(f_{CO}f_{H2O}-f_{CO_2}f_{H2}/K_{WGS}\right)}{(1+K_1f_{CO}+K_2f_{H2O})^2} \tag{16}$$

The kinetic parameters of WGS reaction rate are given in table 4 where, K_{WGS} is the equilibrium constant and can be calculated as follows:

$$\log K_{WGS}=\left(\frac{2073}{T}-2.029\right) \tag{17}$$

Table 4. Rates parameters for WGS reaction

Parameter	Value
kw (mmol.grcat^{-1}.s^{-1}.bar^{-2})	0.77
k_1 (bar^{-1})	0.39
k_2 (bar^{-1})	3.54

3. Results and Discussion

Compressibility factor of the gas mixture is a criterion of its deviation from the ideal behavior. A contour plot of the predicted compressibility

factor along the reactor is shown in (Figure2). The figure shows that formation of heavy hydrocarbons causes the compressibility factor to descend to a value of about 0.9. Therefore, it is necessary to consider the mixture's non-ideality in calculation of density.

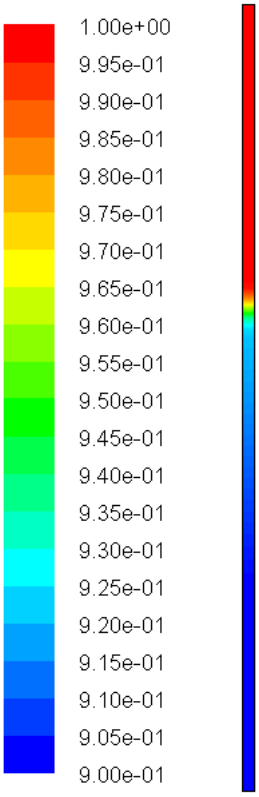

Figure 2. Gas mixture compressibility factor (Z) contour along the reactor
(T=573, P=17 bar, GHSV=5500 hr -1 and CO/H_2=1)

A comparison between the predicted and measured values of C_{5+} selectivity, CO conversion and temperature at three points (at the beginning, middle and end of the catalytic bed) along the reactor for two different operating conditions are given in table 5. The values in this table demonstrate that the error values are less than 4% for all of the compared variables. That is to say, the model in this work can successfully predict the performance of the fixed-bed FT process. Contour plots of temperature inside the reactor shown in (Figure 3) demonstrates that there is a temperature raise of about 17K in the beginning of the catalytic bed due to the high partial pressure of the reactants and the high rate of exothermic reactions in this region.

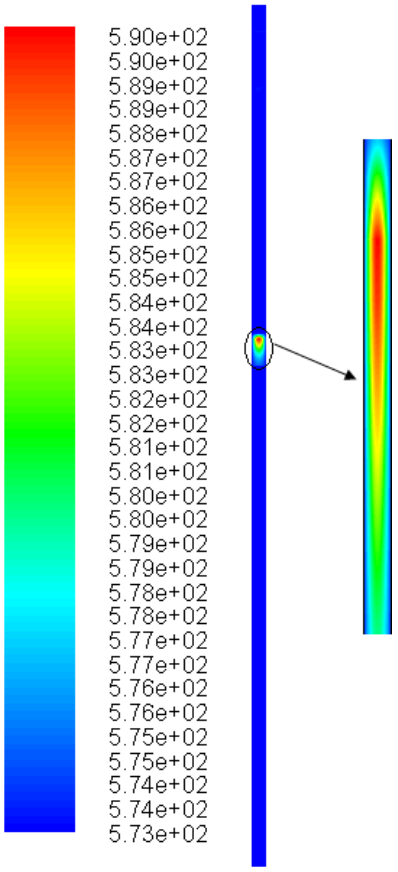

Figure 3. Contour of temperature
(T=573, P=17 bar, GHSV=5500 hr -1 and CO/H_2=1)

However, this amount of temperature raise is tolerable for this process and it could be claimed that the reactor was well controlled at the desired inlet temperature by dilution of the catalyst at the entrance of the reaction zone. Profiles of species mass fraction along the reactor are plotted in (Figure 4). Concentrations of the reactants (CO and H_2) are reduced due to their consumption along the reactor.

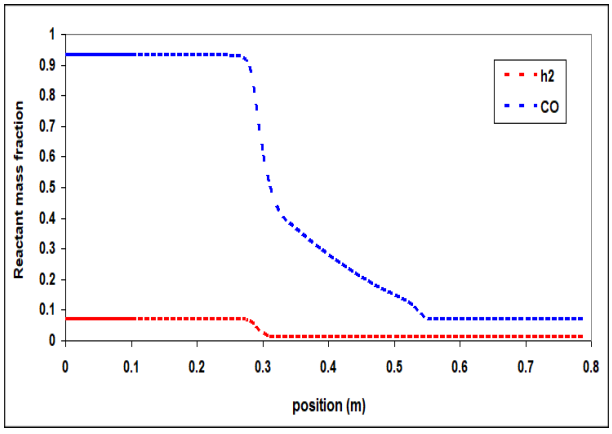

(a) Reactants

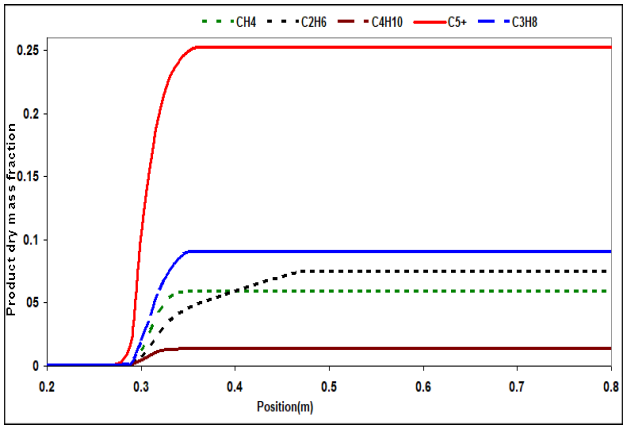

(b) Products

Figure 4. Mass fraction of species along the reactor length (T=573, p=17 bar, CO/H_2=1 and GHSV=5500 hr -1)

Therefore, the reaction rates are reduced and consequently the slopes of species concentration curves along the reactor are decreased. The figure shows that the main changes in the concentrations of reactants and products occur in the beginning of the catalytic zone except for CO and ethane. Ethane acts as a monomer or building block during the FTS. Readsorption of ethane will result in a decrease of the ethane yield and an increase of higher hydrocarbons [29 , 30]. This effect was included in ethane production rate (the power of CO and H_2 concentration in equation (11) is much less than that in other rate equations). The difference between the style of CO concentration profile and that of the other species can also be related to this effect. (Figure 5) interprets the mixture density along the reactor.

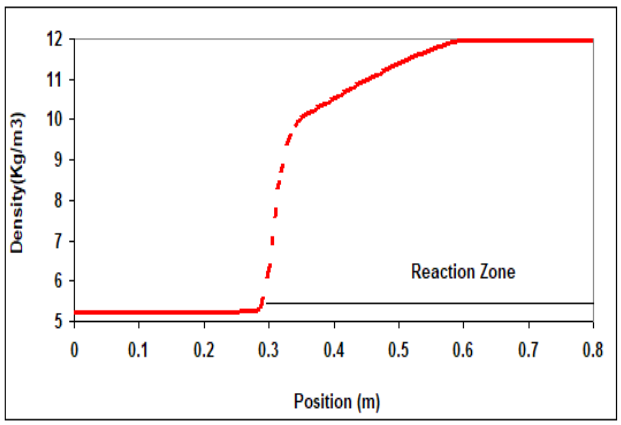

Figure 5. Profile of density
(T=573, P=17 bar, GHSV=5500 hr -1 and CO/H_2=1)

As expected, the mixture density increases along the reactor due to the formation of heavier hydrocarbons. The same reason can be used to describe the velocity reduction along the reactor as shown in (Figure 6). The parabolic radial velocity distribution (in the preheating zone) and zero velocity near the walls due to the no-slip wall boundary condition are also observed in this figure. In addition, pressure drop in the porous region causes the gas velocity to become almost uniform in the radial direction.

The reactor model was run at four different levels of each operating parameters (temperature, GHSV, pressure and H_2/CO ratio) and the effects of these parameters on the performance of the reactor were investigated. In all cases, one parameter was changed and the other parameters were kept constant.

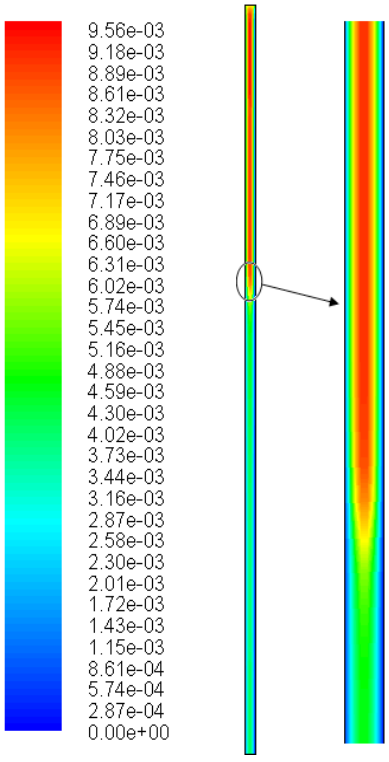

Figure 6. Contour of velocity
T=573, P=17 bar, GHSV=5500 hr -1 and CO/H_2= 1)

The effect of inlet temperature on C_{5+} selectivity (gr C_{5+}/gr converted feed) is shown in (Figure 7). This figure represents that increasing the temperature from 543 to 563 K increases the C_{5+} selectivity. However, further increasing

of the temperature to 583K decreases C_{5+} selectivity. Increasing the reactor temperature has two opposite effects: it increases the rate of reactions and on the other hand, it shifts the WGS equilibrium reaction into consumption of CO to produce CO_2. When the reactor inlet temperature increases from 563 to 583K, the second effect is dominant and the production of C_{5+} reduces due to the reduction in the concentration of available CO.

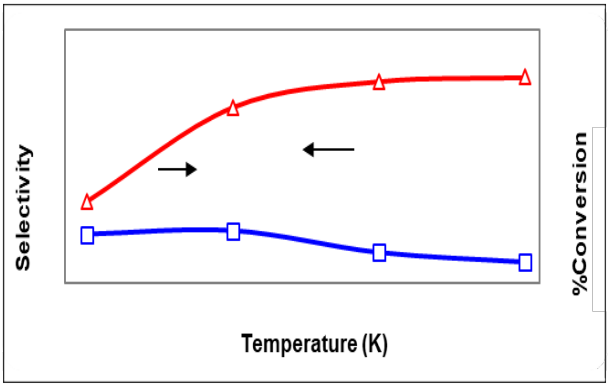

Figure 7. Selectivity of C_{5+} and CO conversion at different temperatures
(P=17 bar, GHSV=5500 hr $^{-1}$ and CO/H_2=1)

(Figure 8) shows that the increase in GHSV, causes a descending trend in the C_{5+} selectivity due to reducing the residence time.

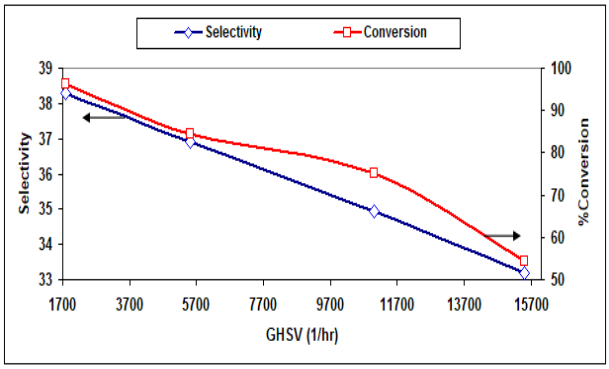

Figure 8. Selectivity of C_{5+} and CO conversion at different GHSVs (T=573, P=17 bar and CO/H_2=1)

The effects of H_2/CO molar ratio on C_{5+} selectivity are presented in (Figure 9). The figure interprets that although increasing the H_2/CO ratio, raises the conversion of CO, but production of heavy hydrocarbons is reduced.

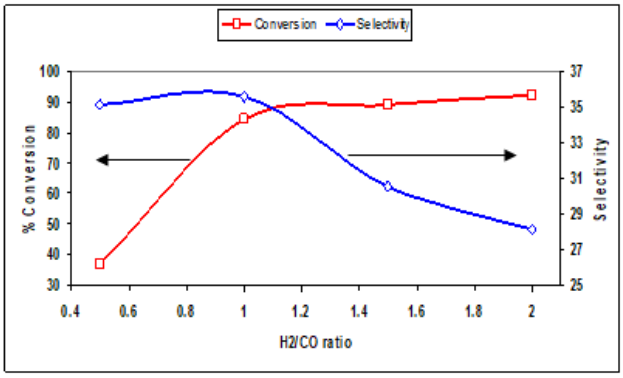

Figure 9. Selectivity of C_{5+} and CO conversion at different H_2/CO molar:
(T=573, P=17 bar and GHSV= 5500 hr -1)

The former effect can be related to the fact that hydrogen can participate in termination steps of polymerization reactions [29, 31]. The effect of pressure as another important affecting parameter on this process is investigated in (Figure11). According to this figure, the C_{5+} selectivity increases by increasing total pressure to reach a maximum at a pressure of about 13 bar and thereafter, it takes a descending style. This can be explained by the fact that by increasing the total pressure, the partial pressures of reactants increase which results in increase of C_{5+} and water as products. The presence of water more than a threshold concentration, has a negative effect on C_{5+} selectivity [32].

4. Conclusions

Production of gasoline from Fischer-Tropsch Synthesis (FTS) process in a bench scale fixed-bed reactor was investigated using experiment and CFD modeling. Peng-Robinson equation of state was utilized to model the non-ideality of the gas mixture. The temperature raise at the beginning of catalytic bed was controlled by dilution of catalyst bed with ceramic particles. The simulation results were compared against the experimental data and good agreements were observed. The effects of operating conditions such as temperature, pressure, GHSV and H_2/CO ratio on reactor performance were studied using the validated model. The approximate values of optimum operating conditions were

obtained in order to reach the maximum yield. The optimum values of temperature, pressure, H_2/CO molar ratio were predicted as 563K, 21bar and 1, respectively. The results showed that the C_{5+} selectivity increases by increasing of GHSV. However, economic considerations are needed to obtain the optimum value of GHSV. Since the model has proven to be in good agreement with the experimental data, it could be used in further studies.

Nomenclature

H	Total enthalpy, $kJ.kg^{-1}.s^{-1}$
h	Enthalpy of species, $kJ.kg^{-1}.s^{-1}$
j	Mass flux, $kg.m^{-2}.s^{-1}$
q	Heat flux, $kJ.m^{-2}.s^{-1}$
S	Momentum source term,
D_{ij}	Diffusivity coefficient,
C_i	Concentration, $kmol.m^3$
Z	Compressibility Factor
T	Temperature, K
f	fugacity, bar
k_i	Kinetic Constant, $mol.hr^{-1}.gr^{-1}.bar^{-1}$
E_i	Activation Energy, $kJ.kmol^{-1}$
R	Global Gas Factor, $kJ.kmol^{-1}.K^{-1}$
M_i	Molecular Weight, $kg.kmol^{-1}$
V	Volume, m^3
x_i	Mass Fraction
D	Total Diffusivity Coefficient, $m^2.s^{-1}$
k_m	Thermal Conductivity, $kJ.m^{-1}.K^{-1}$

Greek Letters

ρ	Density, $kg.m^{-3}$
μ	Viscosity, $kg.m^{-1}.s^{-1}$
φi	Fugacity coefficient

Subscript

i	species number
j	second species number
m	mixture

5. References

[1] H. Schulz, Short history and present trends of Fischer-Tropsch synthesis, Appl. Catal. A-Gen.186 (1999) 3-12.

[2] M.E. Dry, The Fischer-Tropsch process: 1950-2000. Catal. Today .71 (2002) 227-241.

[3] J.B. Butt, T. Lin, L.H. Schwartz, Iron alloy Fischer-Tropsch catalysts, VI. FeCo on ZSM-5, J. Catal.97 (1986)261-263.

[4] H. Schulz, H.L. Niederberger, M. Kneip, F. Weil, Synthesis Gas Conversion on Fischer-Tropsch Iron/HZSM5 Composite Catalysts, Stud. Surf. Sci Catal.61 (1991) 313-323.

[5] G. Calleja, A.D. Lucas, R.V. Grieken, Co/HZSM-5 catalyst for syngas conversion: influence of process variables, Fuel.74 (1995) 445-451.

[6] A.P. Steynberg, M.E. Dry, B.H. Havis, B.B. Berman, Chapter 2 Fischer-Tropsch Reactors, Stud. Surf. Sci Catal.152 (2004) 64.

[7] Q.S. Liu, Z.X. Zhang, J.L. Zhou, Steady state and dynamic behavior of fixed bed catalytic reactor for Fischer-Tropsch synthesis. I. mathematical model and numerical method, J. Nat.Gas .Chem, 8 (1999) 137-180.

[8] Q.S. Liu, Z.X. Zhang, , J.L. Zhou, Steady state and dynamic behavior of fixed bed catalytic reactor for Fischer-Tropsch synthesis. II. Steady state and dynamic simulation results, J.Nat.Gas .Chem, 8 (1999) 238-265.

[9] Y. Wang, Y. Xu, Y. Li, Y. Zhao, B. Zhang, Heterogeneous modeling for fixed-bed Fischer-Tropsch synthesis: Reactor model and its applications, Chem. Eng. Sci. 58 (2003) 867-875.

[10] M.R. Rahimpour, S.M. Jokar, Z. Jamshidnejad, A novel slurry bubble column membrane reactor concept forFischer-Tropsch synthesis in GTL technology, Chem. Eng. Res. Des. (2011) In Press.

[11] A. Nakhaei Pour, M.R. Housaindokht, S.F. Tayyari, J. Zarkesh, S.M Kamali Shahri, Water-gas-shift kinetic over nano-structured iron catalyst in FischereTropsch, J. Nat.Gas. Sci. Eng. 2(2010) 79-85.

[12] X.G. Li, D. X. Liuc, S.M Xu, H. Li, CFD simulation of hydrodynamics of valve tray, Chem. Eng. Process. 48 (2009) 145-151.

[13] S. Vashisth, K.D.P. Nigam, Prediction of flow

profiles and interfacial phenomena for

two-phase flow in coiled tubes, Chem. Eng. Process. 48 (2009) 452-463.

[14] A.I. Stamou, Improving the hydraulic efficiency of water process tanks using CFD models, Chem. Eng. Process. 47 (2008) 1179-1189.

[15] M. Rahimi, S.R. Shabanian, A.A. Alsairafi , Experimental and CFD studies on heat transfer and friction factor characteristics of a tube equipped with modified twisted tape inserts , Chem. Eng. Process. 48 (2009) 762-770.

[16] M. Irani, R.B. Bouzarjomehri, M.R. Pishvaei, Impact of thermodynamic non-idealities and mass transfer on multi-phase hydrodynamics, Scientia Iranica 17 (2010) 55-64.

[17] M. Irani, A. Alizadehdakhel, A. Nakhaei Pour, N. Hoseini, M. Adinehnia , CFD modeling of hydrogen production using steam reforming of methane in monolith reactors: Surface or volume-base reaction model? Int. J. Hydrogen. Energy. 36 (2011) 15602-15610.

[18] B. Chalermsinsuwan, P. Kuchonthara, P. Piumsomboon, Effect of circulating fluidized bed reactor riser geometries on chemical reaction rates by using CFD simulations, Chem. Eng. Process. 48 (2009) 165-177.

[19] R. Krishna, J.M. Van Baten, Scaling up bubble column reactors with the aid of CFD, Chem. Eng. Res. Des. 79 (2001) 283-309.

[20] J.M. Van Baten, R. Krishna, Scale Effects on the Hydrodynamics of Bubble Columns Operating in the Heterogeneous Flow Regime, Chem. Eng. Res. Des. 82 (2004) 1043-1053.

[21] C.W. Jiang, Z.W. Zheng, Y.P. Zhu, Z.H. Luo , Design of a two-stage fluidized bed reactor for preparation of diethyl oxalate from carbon monoxide, Chem. Eng. Res. Des. (2011) In press.

[22] G. Arzamendi, P.M. Diéguez, M. Montes , J.A. Odriozola, E.F. Sousa-Aguiar, L.M. Gandía, Computational fluid dynamics study of heat transfer in a microchannel reactor for low-temperature Fischer-Tropsch synthesis, Chem. Eng J. 160 (2010) 915-922.

[23] M. Irani, A. Alizadehdakhel, A. Nakhaeipour, P. Prolx, A.Tavassoli , An investigation on the performance of a FTS fixed-bed reactor using CFD methods, Int. Commun. Heat. Mass. 38 (2011) 1119-1124.

[24] M. Irani, R.B. Bozorgmehry, M.R. Pishvaie, A. Tavasoli , Investigating the Effects of Mass Transfer and Mixture Non-Ideality on Multiphase Flow Hydrodynamics using CFD Methods, Iran. J. Chem. Eng. 29 (2010) 51-60.

[25] A. Nakhaei Pour, M.R. Housaindokht, S. F. Tayyari, J. Zarkesh, Effect of nano-particle size on product distribution and kinetic parameters of Fe/Cu/La catalyst in Fischer-Tropsch synthesis, J. Nat.Gas. Chem. 19 (2010)107-116.

[26] E. A. Foumeny, H. A. Moallemi, C. Mcgreavy, J. A. A. Castro, Elucidation of mean voidage in packed beds, Can. J. Chem. Eng, 69 (2010) 1010-1015.

[27] Fluent, Incorporated: FLUENT 6 USER Manual, Lebanon (NH): Fluent Inc., 2001.

[28] B.E. Poling, J.M. Prausnitz, J.P. O'Connell, The properties of gases & liquids, 5th ed .McGraw-Hill, New York, 2000.

[29] S. Novak, R. J. Madon , and H. Suhl, Secondary effects in the Fischer-Tropsch synthesis, J. Catal. 77 (1982) 141.

[30] B. Sarup and B.W. Wojciechowski, Studies of the Fischer-Tropsch synthesis on a cobalt catalyst i. evaluation of product distribution parameters from experimental data, Can. J. Chem. Eng. 66 (1988) 831.

[31] G.P. Van der Laan, A. A. C. M. Beenackers, Kinetics and Selectivity of the Fischer-Tropsch Synthesis: A Literature Review, Catalysis Reviews, CATAL. REV. SCI. ENG. 41(1999) 255-318.

[32] S. Krishnamoorthy, A. Li, E. Iglesia, Pathways for CO_2 Formation and Conversion During Fischer-Tropsch Synthesis on Iron-Based Catalysts, Catal. Lett. 80 (2002) 77-86.

JOURNAL OF GAS TECHNOLOGY

Volume 5 / Issue 1 / Summer 2020 / Pages 52-56

Journal Homepage: http://jgt.irangi.org

The Effect of Intermolecular Interactions on the Properties of Poly(chlorobutyl) / Graphene Oxide and Nanoclay Nanocomposites

Majid Safajou-Jahankhanemlou[1*], Mehdi Eskandarzade[2], Jamal Movassagh[3]

1. Department of Chemical Engineering, University of Mohaghegh Ardabili, Ardabil, Iran
2. Department of Mechanical Engineering, University of Mohaghegh Ardabili, Ardabil, Iran
3. Production Consultant of Artawheel Tire Company, Ardabil, Iran

ARTICLE INFO

ORIGINAL RESEARCH ARTICLE

Article History:
Received: 14 May 2020
Revised: 26 June 2020
Accepted: 12 August 2020

Keywords:
Chlorobutyl
Graphite
Graphene oxide
Nanoclay
Nanocomposite

ABSTRACT

Nano composites of graphene oxide and modified nanoclay (Cloisite 15A) were produced based on 80 phr chlorobutyl and 20 phr natural rubber according to inner liner recipe. The results show modified nano fillers have remarkable change in dispersion in the matrix. Subsequently Improved cured products properties. Exfoliation of graphen oxide and Cloisite 15A was confirmed by XRD and TEM. In the case of graphite intercalation has happened. Also physical and mechanical properties of this composite was studied.

DOR: 20.1001.1.25885596.2020.5.1.5.5

How to cite this article
M. Safajou-Jahankhanemlou, M. Eskandarzade2, J. Movassagh. The Effect of Intermolecular Interactions on the Properties of Poly(chlorobutyl) / Graphene Oxide and Nanoclay Nanocomposites. Journal of Gas Technology. 2020; 5(1): 52 -56. (http://www.jgt.irangi.org/article_251660.html)

*Corresponding author.
E-mail address: m.safajou@uma.ac.ir (M. Safajou-Jahankhanemlou)

Available online 03 20 September 2020

1. Introduction

Since 1984, when the Japanese research team of Toyota developed polyamide 6/nanoclay, nanocomposites became one of the important issues [1]. The high aspect ratios, high surface area, and enhancement of significant nanoparticle properties compared to conventional fillers have attracted the attention of many researchers to the development, identification and modeling of polymer nanocomposites [2-3]. The key issue in nanocomposite production is to achieve the highest inter-surface compatibility and complete dispersion of filler in the matrix. Single-layered layers of two-dimensional nanosheets have a higher aspect ratio than their microscopic aggregates. Therefore, nanoscale lamination is required to achieve the highest nanocomposite efficiency [4-10]. Due to the high contact surface and the amount of interactions with the polymer matrix in unit volume, the nanoclay has a significant increase in physical-mechanical properties and decreases in gas permeability in elastomeric nanocomposites [4-5]. The amount of dispersion of modified nanoclay in the rubber matrix depends essentially on the nature of the clay cluster structure [5], the mixing condition [6], (shear rates of mixing and temperature), and the polarity of the rubber matrix [6]. The elastomers exhibit high viscosity during the mixing process due to their high molecular weight, which causes the shear stress required to delaminate the silicate layers of nanocaly [4,6].

In addition to clay nanocomposites, many researchers are working on improving the mechanical, electrical, and barrierity properties of rubber / graphene nanocomposites [6-10]. Graphene is a two-dimensional layer consisting of carbon atoms with sp2 hybrid that are arranged in the structure of the honeycomb that placed on each other [7]. Graphene has an electrical conductivity, mechanical flexibility, optical clarity, excellent thermal conductivity and a small coefficient of thermal expansion, which has made it an excellent attraction among researchers and industrials. Due to its exceptional properties, graphene has been used as an ideal material for the electronics industry, such as battery connections, superstructures, solar cells, sensors, composites, gas separation membranes, hydrogen storage, and biological sensors. Graphene has similar properties in comparison to nanotubes, but its larger surface area can be considered as open-ended nanotubes. In addition, the cost of producing graphene sheets is very low compared to nanotube costs and can be as a cheap alternative to apply in nanocomposites [8-9]. Sheets of graphene oxide can easily be dissipated in water because it has hydroxyl groups. The use of graphene oxide in reinforced composites is one of its applications, it can greatly improve the mechanical and thermal properties of polymer matrix. Zachariah et al. [4] reported improvements in the properties of natural rubber and Chlorobutyl composites by increasing the different nanoparticles of modified clay and provided a mechanism for the of dispersion of these nanoparticles. Tiwari et al. investigated the rheological properties of increasing the graphite nanoparticles to chlorobutyl matrix in the range of -100 °C to 100°C to investigate the effect of the glass transition temperature on the particle dispersion [6]. Another report from the same group concentrates on the effect of nano graphite particles enhancement on the physical mechanical properties of chlorobutyl matrix [7]. In other papers, the same group studied the effect of multi wall carbon nanotubes on chlorobutyl rubber and the distribution of these particles in high percentages by scanning electron microscopy [8-9].

The properties of the chlorobutyl rubber and the butyl rubber properties are very similar to each other. An increase of about 2.1% by weight of chlorine to butyl rubber to increase the reaction of butyl groups in polymer without changing the number of them to enhance the possibilities of vulcanization, and thus the presence of double bond and chlorine in these rubber present different way of vulcanization. The most important consumption of chlorobutyl rubber is in the manufacture of inner liner of tire and is also used in the manufacture of rubber and rubber products, as well as non-toxic vulcanization, it is also used in the

manufacture of medical and food applications. It also used in glue coatings, bunker parts and heat resistant parts up to 150 °C Chlorobutyl rubber reinforced with nano fillers has been shown to be remarkably improved. in physical-mechanical properties [4,7] and reduction of gas permeability have been reported in the references [10]. These properties increase due to the entry of nano-fillers with an impermeable sheet structure. So produce nanocomposites that cover a wide range of products from packaging, pharmaceuticals and automotive industries.

Many researchers have done extensive research on the use of conventional nano-fillers, but the comparison of the properties of these additives has not been studied at the same time. In this report, a comparison was made between graphite nanoparticles, graphene oxide and nanoclay (Cloisite 15A) as nanofillers and chlorobutyl rubber as matrix using X-ray diffraction techniques, transition electron microscopy (TEM) and tensile analysis.

2. Experimental Section

2.1. Materials

Chlorobutyl rubber produced by Langus Company of Belgium and Natural Rubber (SMR20) from Malaysia, the Cloisite 15A clay from Southern, graphite, sulfuric acid, sodium nitrate, potassium permanganate, polymeric sulfur (S8), n oxyethylene 2 -benzothiazole Sulfenamide, zinc oxide and stearic acid were purchased from Merck.

2.2. Production of Graphene Oxide

Based on the Hummers & Offeman method [11], 3 g of graphite with 3 g of sodium nitrate and 200 ml of sulfuric acid (98%) were mixed in 1000 ml balloons in an ice bath equipped with a circulator. Then 9 g of potassium permanganate was added to the above mixture. The solution was kept at 35 °C for 18 hours. The mixer was used for uniformity throughout the reaction. At the end of the reaction, the solution was washed with oxygenated water and distilled water then mixture centrifuged and dried.

2.3. Nanocomposites production

In order to improve the mixing of compound 20phr of natural rubber (SMR20) was used. A two-liter banbury mixer was used to mix the compounds. Compositions of the compounds were shown in Table 1. The rheometer (ODR2000-alpha) was used to obtain optimal curing conditions (scorch time) for each of the compounds. Specimens for tensile test were prepared by compression molding of produced compounds and cutting them in dumbbell shaped specimens with 2mm thickness. (Figurer1) shows four samples prepared for the tensile test.

Table 1. Compositions of the compounds.

LNG HE Name	CIIR/NR-C 15A	CIIR/NR-graphen oxide	CIIR/NR-graphite	CIIR/NR
Ingredients (phr)				
CIIR	80	80	80	**80**
NR	20	20	20	**20**
Graphite	-	-	5	**-**
Graphene-oxide	-	1	-	**-**
Cloisite 15A	4	-	-	**-**
ZnO	3	3	3	**3**
stearic acid	2	2	2	**2**
S8	3	3	3	**3**
N-oxydiethylene-2-benzothiazole sulfonamide	2	2	2	**2**

Figure 1. Cured samples from left, CIIR/NR, CIIR/NR-graphite, CIIR/NR-graphen oxide, CIIR/NR-C 15A

2.4. Characterization

Dumbbell-shaped specimens were prepared from the cured compounds then tensile analysis were done by INSTRON machine at a speed of 10 mm / min. The X-ray diffusion test was carried out using an X-ray diffraction device manufactured by PHILIPS with a copper anode and λ=1/541 at ambient temperature. To analyze quality of nanoparticles distribution in the matrix, the TEM observations were carried out using a Zeiss -EM 900 (80 keV) electron microscopy.

3. Results and Discussion

The XRD spectra obtained from graphene nanocomposites and clay 15A clay exhibit a good distribution of nanoplates (Figurer 2), while in the case of CIRR / NR-graphite composite, delaminating state did not occur, However, the peak has been moved to lower 2θs and has not been eliminated due to the intercalation of graphite layers. Therefore, it is possible to clearly observe the effect of the compatibility of clay and graphene nanoparticles. In order to verify delaminating of CIIR / NR-graphene oxide sample, electron microscopic images were used (Figurer 3).

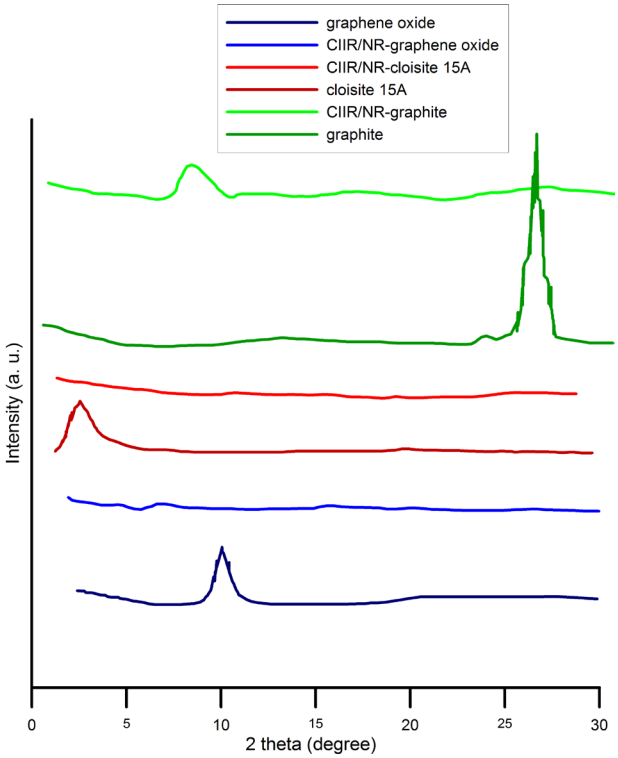

Figure 2. X-ray diffraction of prepared samples.

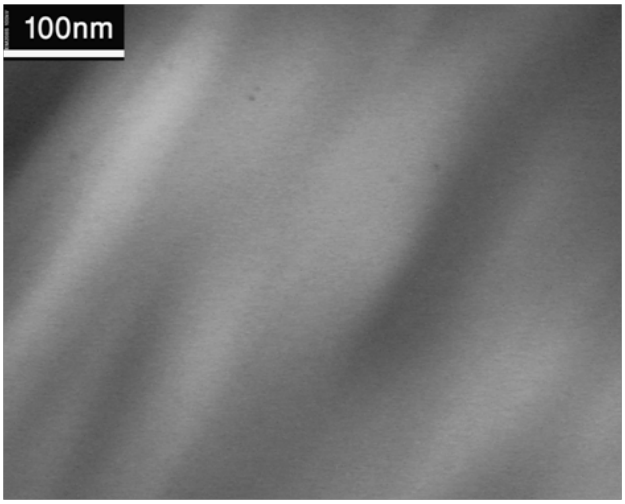

Figure 3. TEM images of CIIR/NA-graphene oxide.

(Figurer 4) also shows the results of the tensile test, as is clear, approximately the reinforcement effect of 4 phr graphite with 1 phr graphene oxide is equal, which is due, firstly, to the proper dispersion (exfoliation) of the nanoparticles of the graphene oxide in the matrix and Secondly, due to the polarization of graphene oxide, it results in greater compatibility between the matrix and the nanofiller compare with graphite.

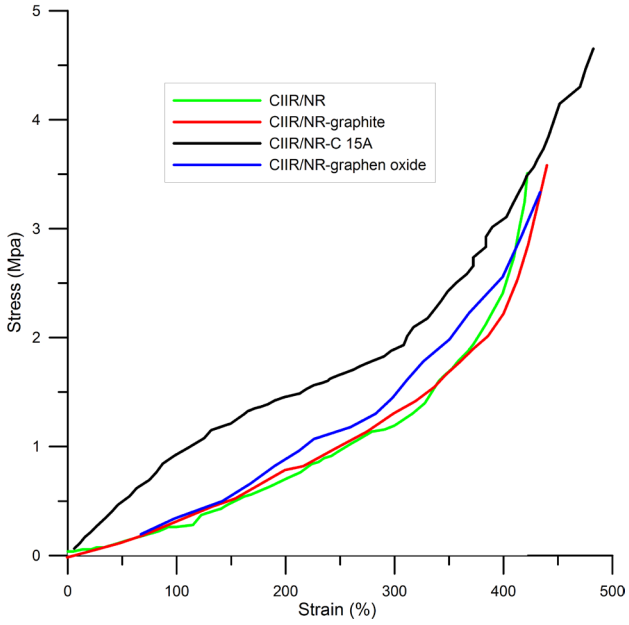

Figure 4. Tensile test results for prepared samples.

4. Conclusion

Enhancing nanoparticles will result in improved properties if they exfoliated in the polymer matrix, and the surface modification of these particles increases matrix-filler compatibility and thus improves dispersion. In the case of graphite and graphene oxide, clearly showed 1 phr of the graphene oxide has more increase properties than 5 phr graphite. The same applies to nanoclay, so that the increased 4 phr modified nanoclay provides high mechanical properties along with proper particle dispersion.

4. References

[1] Kamigaito O, Fukushima Y, Doi H (1984) Composite material composed of clay mineral and organic high polymer and method for producing the same. US patent 4,472,538.

[2] Kojima Y, Usuki A, Kawasumi M, Okada A, Fukushima Y, Kurauchi T, Kamigaito O (1993) Mechanical properties of nylon 6-clay hybrid. J Mater Res 8:1185-1189

[3] Kojima Y, Usuki A, Kawasumi M, Okada A, Kurauchi T, Kamigaito O (1993) Sorption of water in nylon 6-clay hybrid. J Appl Polym Sci 49:1259-1264

[4] Zachariah, A. K., Geethamma, V. G., Chandra, A. K., Mohammed, P. K., & Thomas, S. (2014). Rheological behaviour of clay incorporated natural rubber and chlorobutyl rubber nanocomposites. RSC Advances, 4(101), 58047-58058.

[5] Saritha, A., & Joseph, K. (2014). Effect of nano clay on the constrained polymer volume of chlorobutyl rubber nanocomposites. Polymer Composites. doi: 10.1002/pc.23124

[6] Tiwari, S. K., Choudhary, R. N. P., & Mahapatra, S. P. (2014). Dynamic mechanical and dielectric relaxation studies of chlorobutyl elastomer nanocomposites effect of nanographite loading and temperature. High Performance Polymers, 0954008314545137.

[7] Tiwari, S. K., Sahoo, B. P., & Mahapatra, S. P. (2014). Physico-mechanical and dynamic mechanical studies of nanographite reinforced chlorobutyl nanocomposites. Plastics, Rubber and Composites.

[8] Tiwari, S. K., Choudhary, R. N. P., & Mahapatra, S. P. (2014). Effect of multiwalled carbon nanotube and temperature on dielectric and impedance spectroscopy of chlorobutyl elastomer nanocomposites. Journal of Elastomers and Plastics, 0095244314526742.

[9] Tiwari, S. K., Sahoo, B. P., & Mahapatra, S. P. (2014). Morphology, mechanical, bound rubber, swelling, and dynamic mechanical studies of chlorobutyl elastomer nanocomposites: effect of multiwalled carbon nanotube and solvent. Journal of Polymer Engineering, 34(1), 41-52.

[10] Saritha, A., & Joseph, K. (2014). Role of solvent interaction parameters in tailoring the properties of chlorobutyl rubber nanocomposites. Polymer Composites. doi: 10.1002/pc.23187

[11] Hummers, W.S Offeman, R.E.Preparation of Graphitic Oxide. J. Am. Chem. Soc. 1958, 80, 1339.

JOURNAL OF GAS TECHNOLOGY

Volume 5 / Issue 1 / Summer 2020 / Pages 57-69

Journal Homepage: http://jgt.irangi.org

Application of CFD for Troubleshooting and Hydrodynamic Analysis in an Industrial Three-Phase Gravity Separator

Zohreh Khalifat[1], Mortaza Zivdar[2*], Rahbar Rahimi[3]

1. Ph.D student, Chem. Eng. Dept., Faculty of Eng., University of Sistan and Baluchestan, Zahedan, Iran
2. Corresponding Author: Chem. Eng. Dept., Faculty of Eng., University of Sistan and Baluchestan, Zahedan, Iran
3. Chem. Eng. Dept., Faculty of Eng., University of Sistan and Baluchestan, Zahedan, Iran

ARTICLE INFO

ORIGINAL RESEARCH ARTICLE

Article History:
Received: 26 May 2020
Revised: 22 August 2020
Accepted: 03 September 2020

Keywords:
Three phase gravity separator
Volume of fluid
Dispersed phase model
Troubleshooting
Hydrodynamic analysis

DOR: 20.1001.1.25885596.2020.5.1.6.6

ABSTRACT

Multiphase separation in gravity separators is one of the important processes in different industries. This study presents a computational fluid dynamics (CFD) simulation of an industrial three-phase boot separator applying a coupled volume of fluid (VOF)-dispersed phase model (DPM) method for hydrodynamic analysis and troubleshooting of the separation process. Noted that despite the wide application of the boot separator in different industries, no research has been performed on this type of separator to investigate the macroscopic and microscopic behavior of the separation process. The results of numerical calculations based on three-phase flow profile, secondary phase behavior, separator performance, and size distribution of the droplets were investigated in this research. Results showed that the CFD model is well capable of estimating the separation behavior in a three-phase boot separator. Troubleshooting of the studied separator was also investigated to detect the parameters that might decrease the separation performance. Based on the results, it is concluded that the separator suffers from the type of the inlet diverter, lack of an efficient mist extractor at the gas outlet and also lack of an appropriate vortex breaker at the oil outlet. The effect of increasing the inlet water flow rate on the separator performance was another parameter that was studied in this research. Results demonstrated that increasing the inlet water flow rate from 11823-47295 kg/hr caused an increase in the mass of droplets at the gas outlet from 0.09 to 1.6 kg/hr, but this increase did not lead to a significant decrease in the separation efficiency.

How to cite this article
Z. Khalifat, M. Zivdar, R. Rahimi. Application of CFD for Troubleshooting and Hydrodynamic Analysis in an Industrial Three-Phase Gravity Separator. Journal of Gas Technology. 2020; 5(1): 57 -69. (http://www.jgt.irangi.org/article_251661.html)

*Corresponding author.
E-mail address: mzivdar@eng.usb.ac.ir (M. Zivdar)

Available online 20 September 2020

1. Introduction

Three-phase gravity separators are one of the initial and important process equipment used for separating phases with different densities (oil, water, and gas) in different industries. Inappropriate design of such apparatus leads to a decrease in the separation efficiency of the separators and also causes the downstream equipment which is placed after the separators to be damaged. For example, the presence of liquid droplets with gas or bubble gas with liquids reduces the pump and compressor efficiency. The presence of water in oil phases also causes corrosion in tubes and requires the high cost for repair and maintenance of the equipment. So, appropriate design for such separators leads the industry's performance to be more efficient and economical. These separators are used in two horizontal and vertical types which the horizontal types are more common in Iran and can be categorized in two common types, i.e., weir type (when the water fraction is substantial) and boot type (when the water fraction is not substantial). Generally, semi-empirical methods which are based on the droplet settling theory are used to design the separators (Pourahmadi et al, 2012). Although these methods provide useful guidelines, simplified assumptions used in these methods such as considering a single droplet size with constant velocity in the droplet settling theory and also not considering the effects of turbulence and separator internals lead these approaches not to be completely acceptable (Monnery and Svrcek, 1994; Bothamley, 2013a, b; Ghafarkhah et al, 2017,2018). So, semi-empirical methods need to be improved. One reliable method to overcome the problems in semi-empirical methods is performing experimental studies. Noted that, because of the high-performance cost and technical problems in measuring the internal flow behavior using experimental studies, applying a more complete and economical method such as computational fluid dynamics (CFD) in analyzing the quality and quantity of the separation process and also debottlenecking of the separators is necessary (Ghafarkhah et al, 2018).

Eulerian-Eulerian (E-E) and Eulerian-Lagrangian (E-L) approaches are two common methods used in CFD simulation of multi-phase flows. In the E-E approach which includes the volume of fluid (VOF), mixture and Eulerian models, all the phases are considered as continuous phases which interact with each other. The Navier-Stokes equations are solved in this approach. In the dispersed phase model (DPM) which belongs to the E-L approach, one continuous phase and two or more discrete phases are considered. In this approach, the Navier-Stokes equation and the Newton second's law are solved for the continuous and discrete phase, respectively (Pourahmadi et al, 2012). Although CFD simulations of gravity separators were the subject of several types of researches, most of them were pertinent to the simulation of two-phase separators and limited works studied three-phase separators due to the complicated behavior and also the high calculation time in simulating three-phase flows. Noted that among the studies performed on three-phase separators, most of them used the E-E approach in evaluating the separation process.

Ahmed et al. (2017) used VOF and Eulerian models separately to simulate one pilot plant three-phase separator with a weir. The k-Ɛ model was used to consider the turbulent flow in this research. Because of the assumptions such as considering a single average diameter for liquid droplets, and not considering the interaction between liquid droplets in Eulerian model and also due to not considering suitable grid cell number for tracking the interfaces between phases in the VOF model, a high simulation error (30-50%) relative to field data were observed.

Kharoua et al. (2013 a) used Eulerian with the k-Ɛ model to investigate the flow behavior and separation performance in one three-phase

industrial separator equipped with a weir. Because of considering liquid droplets with a fixed diameter, neglecting coalescence and breakup of the droplets and also the weakness of this model in the exact tracking of the interfaces between phases, unreliable results such as existing more water in the oil outlet were observed which were not in agreement with the field data.

In another study performed by Kharoua et al. (2013b) population balance model (PBM) was coupled with the Eulerian model to overcome the problems in their previous work. In this study, the droplet size distribution of the liquid droplets and also the coalescence and breakup of the droplets were taken into account. Although the results were in a better agreement with the field data, due to the limitation in this model pertinent to considering the droplet size distribution for just one secondary phase, the difference between simulation and industrial data were not negligible.

Considering the results of the studies on the models in the E-E approach showed that these models were not successful in exact estimating of the separator performance. Noted that among the models in the E-E approach, the VOF model is suitable in tracking the interfaces between phases and also the interfaces between the droplets and the continuous phase, but this model needs to track free surface around each droplet for the exact estimating of the droplet behavior and also the separator performance. So, a very fine grid is obligatory to achieve the exact simulation results which are not economical to be used in industrial scales. Using the DPM model is a solution to the problem encountered in the VOF model in which the droplets in the DPM model are treated as source terms that move into the domain (Cloete et al, 2009; Kirveski et al, 2013). It is noted that the coalescence and breakup and also the droplet size distribution of all the secondary phases can be considered in this model, but two continuous phases (oil and water) in three-phase separators which accumulate at the bottom of the separator are neglected in this model and just one gas phase as continuous phase and oil and water droplets as dispersed phases are modeled which leads to unreliable results in simulating three-phase separators (Pour Ahmadi et al, 2011). Therefore, DPM model needs three phases at the background to consider all three continuous phases and also to be available for droplets to interact with them. Because of the exact tracking of the interfaces between phases in the VOF model, it is a good candidate to be coupled with the DPM model for modeling three phases at the background (Pourahmadi et al, 2011; Qarot et al, 2014). Although the coupled VOF-DPM model is completely acceptable in simulating multiphase flow (Cloete et al, 2009a, b), very limited researches were performed on simulating industrial three-phase separators using this model.

Pourahmadi et al. (2011, 2012) used VOF-DPM with k-ε turbulence model to simulate an industrial three-phase (oil, water, and gas) separator with a weir to improve its performance. The droplet size distribution of the secondary phases and also coalescence and breakup were taken into account in this study. Results showed that this model was good at estimating the separator performance to debottleneck the separator.

In another study performed by Ghafarkhah et al. (2017,2018), two different semi-empirical methods were used to design a pilot plant three-phase separator with a weir using VOF-DPM- k-ε model to show which method is more realistic. Results demonstrated that the mentioned coupled model was successful in estimating the best dimension of the separator.

As it was mentioned before, in spite of different studies performed on the CFD simulation of multiphase separators, most of them considered the simulation of two-phase separators and limited works studied three-phase separators in industrial scales due to the complicated behavior and also the high

calculation time in simulating three-phase flows in industrial scales. Three-phase boot separators are one of the important types of separators used when the volume fraction of water is very low relative to the other phases, but among the studies performed on three-phase separators, no research has been carried out on the CFD simulation of these types of separators to investigate their performance. So, the main object of this research is using a CFD model for investigating the hydrodynamic analysis to consider the microscopic and macroscopic treatments of the separation process in one industrial three-phase boot separator. Noted that the studied industrial separator is located in the Borzoye petrochemical Company in the south of Iran. Troubleshooting of the mentioned industrial separator was another important parameter which was considered in this research to detect the factors that might decrease the separation efficiency. Results highlighted the need for changing or adding some internals in the industrial separator to achieve better separation. To simulate the intended separator, a coupled VOF-DPM model because of its advantages over the other models mentioned in the introduction, was chosen and the commercial CFD package, Ansys Fluent 16.2 was selected for this purpose. The VOF model in this study was used to show the total fluid flow profile at the background (continuous oil, gas and water phases) and the DPM model was used to consider the behavior of the droplets in the separator. The k-Ɛ model was selected as the turbulence model in this study. Three-phase flow profile, secondary phase behavior, separator performance, and the size distribution of the droplets were the results of the numerical calculations. Results expressed that the VOF-DPM model is successful at estimating the separation behavior of the three-phase boot separator. It is noted that the effect of increasing the inlet water flow rate on the separator performance, due to the need to change the inlet water flow rate in the industry, was also investigated in this research.

2. Mathematical Modeling

The model used in this study is the combination of the VOF model to simulate three continuous phases at the background to track the interfaces between phases and also the DPM model to track the dispersed phases while interacting with the continuous phases.

1.2. VOF Model

The VOF model is used when tracking the interfaces between phases is important. In this model, one continuity equation for each phase to track the volume fraction of phases and also one momentum equation with a shared velocity field for all the phases are solved. The continuity equation for each phase is as (Cloete et al, 2009b; Xu et al, 2013).

$$\frac{\partial}{\partial t}(\alpha_m \rho_m) + \nabla \cdot (\alpha_m \rho_m \vec{u}_m) = 0 \quad (1)$$

Where the subscript m is denoted as phase m. In this equation, $\vec{u}$, α and ρ are the average velocity, volume fraction and density of the continuous phase, respectively. The momentum equation is expressed as (Ansys Fluent, 2016; Bracill et al, 1992):

$$\frac{\partial}{\partial t}(\rho \vec{u}) + \nabla \cdot (\rho \vec{u}.\vec{u}) = -\nabla P + \nabla \tau + \rho g + \vec{F} \quad (2)$$

Where τ is the shear stress, P is pressure and $\vec{F}$ is a source term denoted as the surface tension force between phases by applying the continuum surface force model proposed by Brackbill et al (Ansys Fluent, 2016; Bracill et al, 1992).

2.2. DPM Model

In this model, tracking of droplets in the E-L approach is predicted by implementing the Newton second's law on each droplet. The particle acceleration in this equation is because of the drag, gravity and additional forces that

are exerted on the droplets due to the existing of the continuous phase. This equation is shown as (Xu et al, 2013; Ansys Fluent, 2016):

$$\frac{d\overrightarrow{u_p}}{dt} = F_D\left(\vec{u} - \overrightarrow{u_p}\right) + \frac{g\left(\rho_p - \rho\right)}{\rho_p} + \vec{f} \qquad (3)$$

Where the subscript p represents the particles. The additional forces $(\overrightarrow{f})$ in this equation are mainly virtual mass, Brownian and thermophoretic forces (Xu et al, 2013; Ansys Fluent, 2016).

F_D is the drag force which is shown as (Xu et al, 2013):

$$F_D = \frac{18\mu C_D\, Re}{24\rho_p {d_p}^2} \qquad (4)$$

μ, d_p and ρ_p are the molecular viscosity, the diameter, and density of the particles, respectively. C_D is the drag coefficient which is calculated based on the Morsi and Alexander for spherical particles (Xu et al, 2013).

3-2. Turbulence Equation

The multiphase model in this work is coupled with the k-Ɛ model to consider the effect of turbulence on the separation process. Two different equations are solved using the k-Ɛ model for calculating turbulent kinetic energy (k) and turbulent dissipation rate (Ɛ) (Ghafarkhah,2017; Ansys Fluent, 2016):

$$\frac{\partial(\rho k)}{\partial t} + \frac{\partial(u_i \rho k)}{\partial x_i} = \frac{\partial}{\partial x_j}\left[\left(\mu + \mu_t\right)\frac{\partial k}{\partial x_j}\right] - \rho\varepsilon + \beta \qquad (5)$$

$$\frac{\partial}{\partial t}(\rho\varepsilon) + \frac{\partial}{\partial x_i}(u_i \rho\varepsilon) = \frac{\partial}{\partial j}\left[\left(\mu + \frac{\mu_t}{\sigma\varepsilon}\right)\frac{\partial \varepsilon}{\partial x_j}\right] + \beta C_1 \frac{\varepsilon}{k} - \rho C_2 \frac{\varepsilon^2}{k} \qquad (6)$$

β, is the kinetic energy production term due to velocity gradient, σ is the surface tension and μ_t, is the turbulent viscosity which is calculated by equation 7 (Ghafarkhah et al, 2017).

$$\mu_T = \rho C_M \frac{k^2}{\varepsilon} \qquad (7)$$

The constants in equations 6 and 7 are as (Ansys Fluent, 2016):

$$C_1 = 1.44\ ,\ C_2 = 1.92\ ,\ C_M = 0.09\ ,\ \sigma_k = 1\ ,\ \sigma_\varepsilon = 1.3 \qquad (8)$$

3. Fluid Properties

To show the separation process in this research, data of one industrial three-phase boot separator located in the Borzoye petrochemical Company were used. The mentioned separator operates at a temperature of 47°C and a pressure of 19 bar. To calculate the volume percentage and physical properties of each phase, the separator was simulated using Aspen Hysys V.9 (Khalifat et al, 1396) and the results were used to perform the present CFD simulation. The results of the Hysys simulation showed that the densities of the gas, oil, and water phases were 3.28, 692.6 and 991.1 kg/m^3, and their corresponding viscosities were 9.332e-6, 3.685e-4, and 5.783e-4 (kg/m.s), respectively. It should be noted that the volume percentages of each phase at the inlet mixture were 83.59%, 15.86%, and 0.56%, respectively.

The droplet size distributions of the secondary phases in the DPM model were estimated using logarithmic Rosin-Rammler equation as (Pourahmadi, 2010):

$$Y_{(d)} = 1 - exp\left(\frac{-d}{\bar{d}}\right)^n \qquad (9)$$

Where $Y_{(d)}$ is the mass fraction of particles, n is the spread parameter and d is the particle diameter (Pourahmadi et al, 2010).

The maximum and mean of droplet sizes were calculated based on one equation taken from a comprehensive study that considers all the physical properties of the fluid, which is shown as (Pourahmadi , 2010):

$$d_{max} = 1.38\left(\frac{\sigma^{0.6}}{{\rho_c}^{0.3}{\rho_d}^{0.2}{\mu_c}^{0.1}}\right)\left(\frac{D^{0.5}}{{u_c}^{1.1}}\right) \times \qquad (10)$$

$$\left(1 + 0.5975\left[\frac{\mu_d({\mu_c}^{0.25}{u_c}^{2.75}{\rho_c}^{-0.25}D^{-1.25}{d_{max}})^{\frac{1}{3}}}{\sigma}\right]\sqrt{\frac{\rho_c}{\rho_d}}\right)^{0.6}$$

$$d_{mean} = 0.4\, d_{max} \quad (11)$$

The subscripts c and d are denoted as continuous and dispersed phases. D is the internal diameter of the tube which flow passes through it. The max and mean in the above equations are the representative of the maximum and mean of the droplets.

4. Physical Modeling and Grid Generation

Three-dimensional (3-D) modeling of the intended boot separator, which is shown in (Figure1), is performed in Gambit 2.4.6. The separator is equipped with one slopped inlet diverter at the entrance and one boot vessel to store the water at the bottom. As it was mentioned before, these separators are used when the amount of water is negligible compared to the other phases (water flow rate should be less than 20% of the total mass flow rate). Generally, the inlet diverters at the entrance are used to change the velocity and flow direction to help the bulk of liquids separate from the gas phase and move towards the bottom of the separators. At the next zone, some liquid droplets which were not separated in the first zone, have the opportunity to be separated from the gas phase due to gravity. It should be noted that the two continuous oil and water phases that accumulate at the bottom of the separator provide the required time to separate the gas phase from the liquid and also one liquid from the other liquid phase. Unlike the weir separators, water collects at the boot, not at the main vessel. So, the main vessel diameter of the boot separator is smaller than the weir separators (Pourahmadi, 2010). The length, main body diameter and the boot diameter of the studied separator are 11.9 m, 3.6m, and 1.5 m, respectively. To generate the grid for the geometry, the vessel was divided into different volumes, and a tetrahedral/hybrid scheme was used. The quality of the produced mesh based on the skew factor is shown in (Figure 2). Based on the results, only a few percentages of the cells (0.1%) have skew factor more than 0.8 which shows that the studied grid is of high quality. The mesh independence test in this study was performed by increasing the cell number until the same results were observed. In this study, the separator with 1,182,305 cells was selected as the case with the optimum cell number.

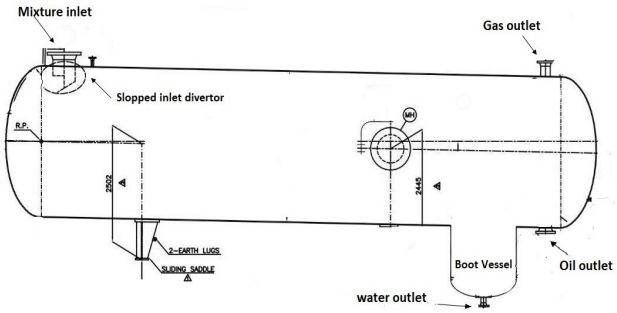

Figure 1. Schematic of the industrial boot separator.

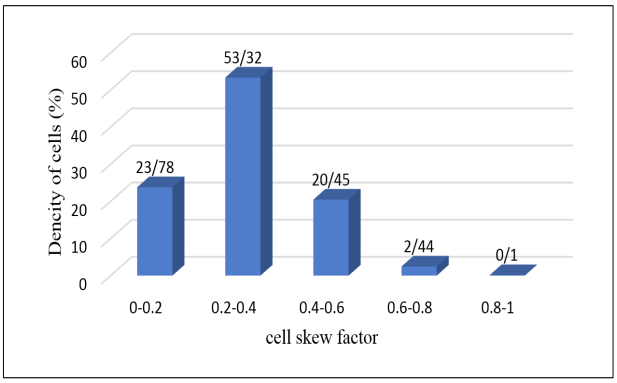

Figure 2. The quality of the produced mesh.

5. Boundary Condition

A velocity inlet for the inlet mixture and the pressure outlet for the gas phase were selected as the boundary condition types in the VOF model. For the liquids at the outlets, the velocity boundary type was utilized to control the interfaces between phases (Ghafarkhah et al 2017,2018; Pourahmadi et al 2011,2012). For the DPM model, the escape zone boundary condition was selected for the inlet and the outlets. In this model, the droplets which reach the wall surrounded by the liquid phases are assumed to be trapped, and those which reach the walls in the gas zone reflect and lose

their momentum (Ghafarkhah et al 2017,2018; Pourahmadi et al 2011,2012).

6. Discretization and Numerical Methods

The equations used in the modeling of the separators were discretized using the finite volume method. The simple algorithm (Ghafarkhah et al 2017,2018; Ansys Fluent, 2016), was used in the Navier Stokes equation to couple the pressure and velocity. Turbulent kinetic energy parameters and the momentum equation were discretized using the second order upwind method. To interpolate the pressure at the numerical cell faces, the presto scheme due to the accordance with the VOF model was utilized (Ghafarkhah et al, 2017; Xu et al, 2016; Ansys Fluent, 2016).

7. Results and Discussion

In this research, the VOF model was used to show the total fluid flow profile on the macroscopic scale. To make a realistic simulation, the DPM model was coupled with the VOF model to track the droplets and investigate the microscopic behavior. So, to consider both the macroscopic and microscopic features of the separation process, the governing equations for both continuous and dispersed phases were solved simultaneously. The assumptions used in this study were, considering constant physical properties, 3-D model simulation, and turbulent flow. The simulation results based on three-phase fluid flow profiles, secondary phase behavior, separator performance, and droplet size distribution of the secondary phases and also the result for troubleshooting of the separation performance are as follows:

1.7. Three-phase fluid flow profiles

The CFD simulation results based on pressure, volume fraction contours and velocity vector are depicted in (Figures 3 to 5) to show the total fluid flow behavior. The simulation results based on the pressure contour in (Figure 3) show that the separator works at constant pressure (except for the variation due to the levels of the liquids) which this result is in a complete agreement with the industrial behavior (Pourahmadi et al, 2011; Mohammadi Ghaleni et al,2012). The oil volume fraction contour in (Figure 4), reveals that all the phases have been separated from each other by a clear interface because of the gravity force. The almost stratified gas-oil and oil-water interfaces predicted by the numerical calculations show the low foaming tendency in the studied separator.

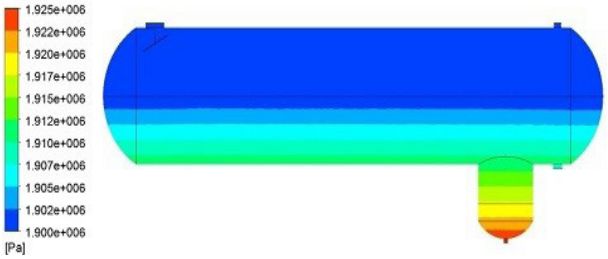

Figure 3. Contour of pressure in the separator.

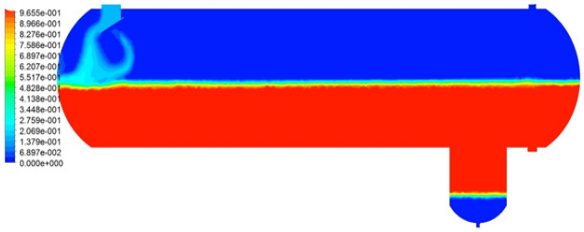

Figure 4. Contour of oil volume fraction.

The velocity vectors are drawn in (Figure 5). Based on (Figure 5-a), the velocity magnitude in the middle of the separator is much lower than the inlet and outlets. As it is more evident in (Figure 5.b), the flow direction changed and the velocity magnitude decreased by passing from the inlet diverter which shows the reduction in momentum flow. As it was mentioned, the main role of an inlet diverter is changing the flow direction and reducing the velocity magnitude to have a good separator performance (Pourahmadi, 2010), so the trend demonstrated in (Figure 5.b) shows that the used CFD model

can appropriately predict the flow behavior by hitting the inlet diverter. To show the velocity magnitude along the separator with a high resolution, multiple vertical planes which are shown in (Figure 6), were modeled and the average velocity was recorded at each plane. The results of the velocity profile along the separator are illustrated in (Figure 7). In fact, the gas phase velocity should be decreased sufficiently from the inlet to the outlet (mostly at the first zone due to the existence of the inlet diverter) to help the droplets settle out by gravity easier due to more retention time of gas caused by low gas velocity along the separator (Ghafarkhah et al, 2017,2018; Pourahmadi, 2010). Thus, the decreasing trend in the velocity magnitude observed in (Figures 5 and 7) shows that the studied CFD model is good at evaluating the fluid flow profile in separators.

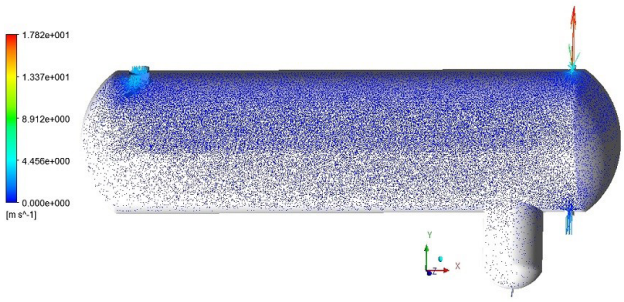

(5.a)

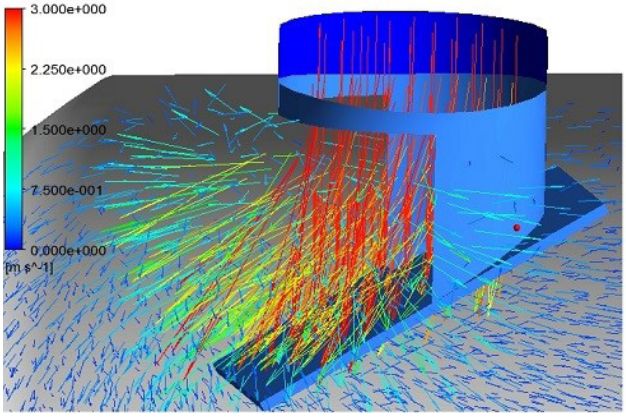

(5.b)

Figure 5. Velocity vector at (a): the separator (b): the entrance.

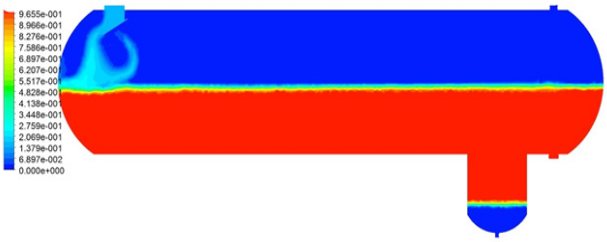

Figure 6. The planes which are modeled at the horizontal direction (x).

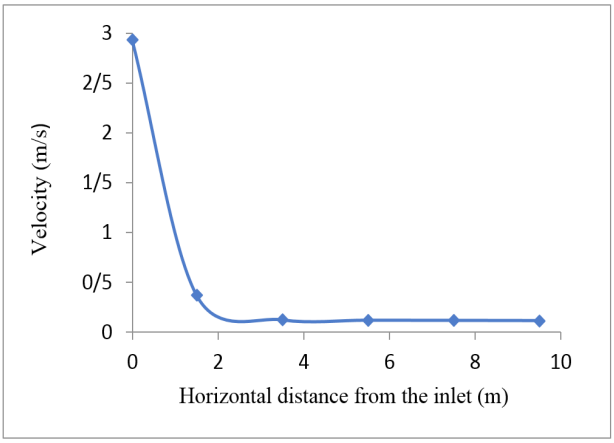

Figure 7. Velocity profile along the separator.

2.7. Secondary phase behavior

Kinetic energy which is completely related to the motion of the particles is a concept that can be used to evaluate the microscopic feature of the discrete phases in the separator. This feature can be investigated by tracking the droplets applying the DPM model (Ghafarkhah et al, 2017). The kinetic energy of the oil droplets in the gas-rich zone of the studied boot separator is presented in (Figure 8). In fact, in a separator, the kinetic energy of the droplets should be decreased from the inlet towards the outlet to let the droplets separate easier and have a good separator performance so that the presence of the liquid at the gas outlet be at the minimum amount (Ghafarkhah et al, 2017). As it is illustrated in (Figure 8), the kinetic energy of the droplets in the intended boot separator decreased from the inlet to the outlet and shows that the CFD model with a decreasing trend in the kinetic energy along the separator, is applicable of good estimating of the separator performance.

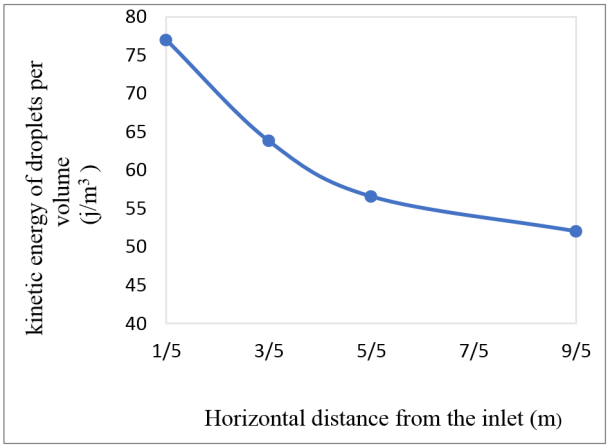

Figure 8. Kinetic energy of oil droplets.

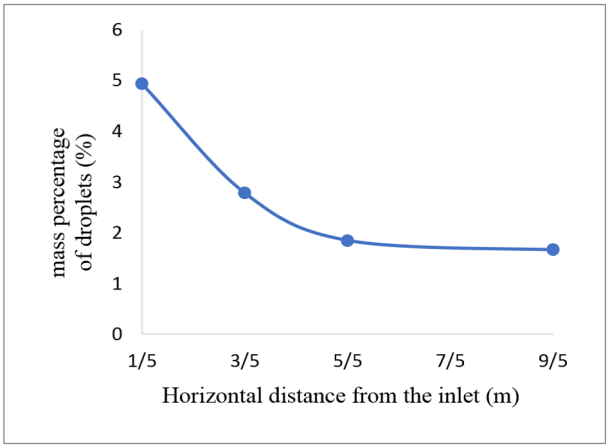

Figure 9. Mass percentage of oil droplets along the separator.

3.7. Separation Performance

To validate the simulation results, the performance of the mentioned separator based on the presence of the oil droplets along the separator was considered. Noted that, due to the sufficient retention time of water in the boot, no problem can be seen in the liquid-liquid separation, and the main problem is the gas-liquid separation (Pourahmadi, 2010). Generally, the mass of liquid droplets should be decreased from the inlet to the outlet to have a good gas-liquid separation performance (Ghafarkhah et al, 2017). (Figure 9) illustrates the mass percentage of the oil droplets along the separator which is calculated by tracking the droplets using the DPM model. In fact, different vertical planes were modeled along the gas-rich zone (Figure.6) and the mass percentage of the droplets (mass of liquid droplets that reach each plane per total mass of the droplets at the inlet) was recorded at each plane. As it is seen, the mass percentage of the oil droplets along the separator decreased. The descending trend shown in (Figure 9), is in complete accordance with (Figure 8), i.e., decreasing the kinetic energy of the droplets. As mentioned earlier, decreasing the kinetic energy of the droplets let the droplets separate easier and reduce the mass of the liquid droplets from the inlet towards the outlet (Ghafarkhah et al, 2017). So, the complete accordance between (Figures 8 and 9), validates the use of the CFD model at estimating the quality of the separation.

4.7. Droplet Size Distribution of the Secondary Phases

One of the important parameters to achieve the best quality of the separation process, except existing the minimum amount of liquid droplet mass at the gas outlet, is the appropriate droplet size distribution of the liquid droplets at the gas outlet. Appearing droplet size more than 100 μm shows that the separator does not work properly and suffers from the appropriate design (Arnold and Stewart, 2008; Pourahmadi, 2010). Tables 1 and 2 show the droplet size distribution of oil and water droplets at the gas outlet. As presented in Tables 1 and 2, the most percentage of both oil and water droplets have diameters less than 100 μm using the model.

Table 1. Droplet size distribution of oil droplets in the gas outlet

droplet size (μm)	25	45	63	83	102	122	141	160	179
Mass percentage of oil droplets (%)	5	30	30	19	8	4	2	1	1

Table 2. Droplet size distribution of water droplets in the gas outlet

droplet size (μm)	25	44	62	80	98	116	134
Mass percentage of water droplets (%)	12	45	20	16	3.5	2.5	1

5.7. Troubleshooting of the Separation Performance

As it was mentioned previously, CFD simulation has the priority over the experimental studies in that the internal flow behavior can't be investigated at each point using experimental works due to the technical problem in measuring the internal flow features and also because of the high experimental cost. So, the CFD simulation can be an economical method in investigating the internal flow to detect the imperfections of the separation process. Troubleshooting of the intended separator was investigated in this research by considering the fluid flow behavior using the CFD model. Considering the inlet diverter zone in the volume fraction contour shown in (Figure 4), revealed that the mixture flow (mostly the liquid phases which reached the interface) had a backward direction towards the gas-rich zone. This behavior shows that the momentum of the flow had not been sufficiently decreased by the used inlet diverter. So, the bulk of liquid can't effectively be separated at the first zone of the separator (the inlet diverter zone) and the performance of this zone will be reduced. Thus, changing the type of inlet diverter will be suggested. By a closer look at the oil outlet which is magnified and shown in (Figure 10), a small vortex is detected. A vortex can suck some gas from the gas rich-zone and re-entrain it in the oil outlet (Arnold and Stewart, 2008). So, the separator performance will be reduced by this phenomenon and causes the downstream equipment to encounter many problems. This problem can be overcome by implementing an appropriate vortex breaker.

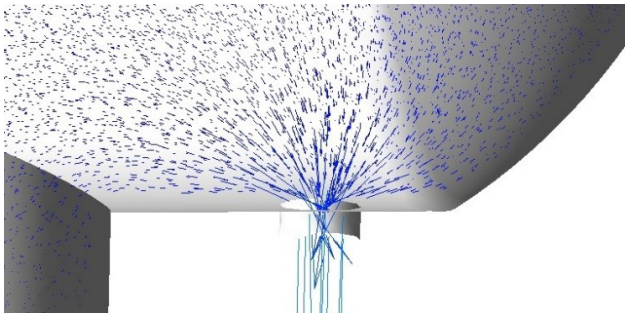

Figure 10. The velocity vector at the oil outlet.

Since the appropriate diameter distribution of the liquid droplet in the gas outlet is one of the key parameters which shows that the separator works properly, it should be investigated at each study to check the performance of the studied separator. In fact, appearing droplet size more than 100 μm shows that the separator does not work properly and suffers from the appropriate design (Arnold and Stewart, 2008; Pourahmadi, 2010) but droplets less than 100 μm in the gas outlet can be separated by applying an appropriate mist eliminator to improve the separation performance (Ghafarkhah et al, 2018; Pourahmadi, 2010). It should be noted that appearing droplets with diameter greater than 100μm might cause a flood in mist eliminator and damage it (Arnold and Stewart, 2008; Ghafarkhah et al, 2018). Based on the results of Tables 1 and 2, most of both oil and water droplets have a diameter less than 100 μm using the model. Thus, its performance might increase by applying an appropriate mist eliminator to reduce the liquid droplets at the gas outlet.

6.7. Effect of Altering the Inlet Water Flow Rate on the Separator Performance

AChanging the inlet flow rate is one of the important parameters which has been paid less attention while designing a separator. Totally, a separator should be designed so that changing the inlet flow rate (in a limited range based on the field experience) doesn't lead to a significant reduction in the separator efficiency. But generally, this is a problem in the industry which requires the separator to have a new design while changing the flow rate, which leads to paying the high cost (Ghafarkhah et al,2017,2018; Pourahmadi, 2010). In this section, the inlet flow rate of the water in the boot separator was changed to see its effect on the separator performance. The water flow rate was increased in the range of 11823-47295 kg/hr based on the field experience (until the water flow rate is less than 20% of the total mass flow rate in a boot separator). (Figure 11) shows the effect of increasing the water flow rate on the

separation of the water droplets from the gas phase. It is depicted that increasing the inlet flow rate leads to an increase in the liquid droplets at the gas outlet which causes a decrease in the separation efficiency. In fact, Increasing the flow rate decreases the required retention time for separating the droplets from the gas phase, so an increase in the mass of liquid droplets at the gas outlet will be achieved (Mohammadi Ghaleni, 2012). Noted that although the increase in the water flow rate in the present separator leads to an increase in the liquid droplet mass at the gas outlet, the droplet mass at the maximum flow rate is just 1.6 kg/hr which doesn't significantly decrease the separator efficiency.

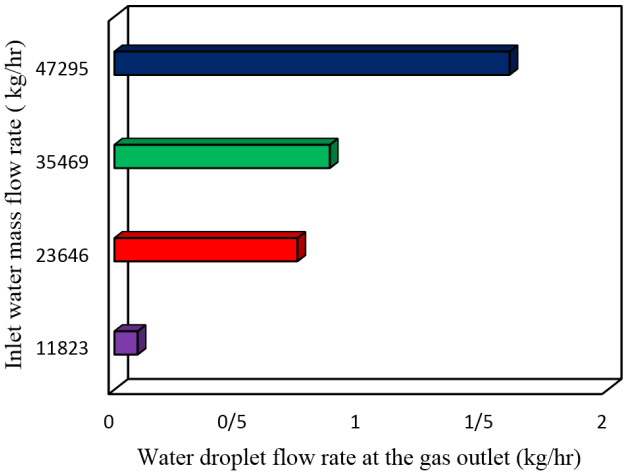

Figure 11. Effect of inlet water flow rate on the separator performance.

8. Conclusion

A 3-D VOF-DPM model was used in this research to show the macroscopic and microscopic features of the separation process in one industrial three-phase boot separator. The results of the fluid flow profiles in the macroscopic scale using the VOF model show that the separator works at constant pressure with a decrease in velocity magnitude by passing from the slopped inlet diverter towards the outlet. The results in the microscopic scale reveal the decrease in the kinetic energy of the droplets and also the decrease in the presence of liquid droplets from the inlet to the outlet. Results of the fluid flow profile and the complete agreement between the trends of the kinetic energy and the mass percentage of liquid droplets along the separator show that the CFD model is successful at good estimating of the separation process in the separator. Troubleshooting of the mentioned separator was another work that was considered in this research. Results demonstrated that due to the backward flow at the entrance and also because of the vortex detected at the oil outlet, the separator suffers from an appropriate design. So, applying an appropriate inlet diverter at the entrance and also a proper vortex breaker at the oil outlet were the suggestions at this research. The droplet size distribution of liquids at the gas outlet showed that the average diameter of both oil and water were less than 100 μm that requires an appropriate mist eliminator to increase the separator efficiency by omitting the liquid droplets at the gas outlet. The effect of increasing the water flow rate on the separator efficiency was also considered in this research. It is concluded that increasing the water flow rate from 11823-47295 kg/hr causes the increase in the water droplet mass at the gas outlet from 0.09 to 1.6 kg/hr, due to the reduction in the required retention time for separating droplets from the gas phase. Results demonstrate that although the increase in the water flow rate increases the water droplet mass at the gas outlet, due to less amount of water droplet mass at the gas outlet even at the maximum inlet water flow rate, a significant decrease in the efficiency can't be observed. So, the intended separator has the ability to change the inlet water flow rate in the range of 11823-47295 kg/hr without a significant decrease in the separation efficiency.

Nomenclature

C_D	Drag coefficient [-]
D	Pipe diameter of the flow [m]
dp	Particle diameter [m]
d_{max}	Maximum diameter [m]
d, d_{mean}	Mean of diameter [m]
F_D	Drag force [N]
$\vec{F}$	Source term force [N/m^2]
$\vec{f}$	Additional force per particle mass [m/s^2]
g	Gravity acceleration [m/s^2]
k	Turbulent kinetic energy [m^2/s^2]
P	Pressure [N/m^2]
$\vec{u}$	Velocity of fluid [m/s]
$\vec{u}_m$	Velocity of phase m [m/s]
u_p	Particle velocity [m/s]
α_m	Volume fraction of phase m [-]
ε	Turbulent dissipation rate [m^2/s^2]
μ	Molecular viscosity [pa.s]
μ_c	Molecular viscosity of continuous phase [pa.s]
μ_d	Molecular viscosity of dispersed phase [pa.s]
ρ	Density [kg.m^{-3}]
ρ_c	Density of continuous phase [kg/m^3]
ρ_d	Density of dispersed phase [kg/m^3]
ρ_p	Density of particle [kg/m^3]
μ_m	Density of phase m [kg/m^3]

Acknowledgements

The authors thank the Borzoyeh Petrochemical Company for providing all the required data in this research.

9. References

[1] Ahmed, T., Hamed, F., Russell, P.A., 2017. The use of CFD simulation to compare and evaluate different sizing algorithm for three - phase separator. OTC offshore technology conference. Brazil, 24-26.

[2] ANSYS Fluent version 16.2, 2016, Fluent Theory Guide.

[3] Arnold, K., Stewart, M., 2008. Surface production operations: design of oil handling systems and facilities. Amsterdam: Elsevier.

[4] Bothamley, M., 2013a. Gas/liquid separators: quantifying separation performance-part 1. Oil and Gas. Fac., 2 (4), 21-29.

[5] Bothamley, M. 2013b. Gas/liquid separators: quantifying separation performance-part 2. Oil and Gas. Fac., 2 (5), 35-47.

[6] Bracill, J.u., Kothe, D.B., Zemach, c., 1992. A continuum method for modeling surface tension. J.Comput.Phys., 100, 335-356.

[7] Cloete, S., Eksteen, J.J., Bradshaw, S.M., 2009 a. A mathematical modelling study of fluid flow and mixing in full scale gas stirred ladles. Computational Fluid Dynamics, 9(6), 345-356.

[8] Cloete, S., Olsen, J.E., Skjetne, P. 2009b. CFD modeling of plume and free surface behavior resulting from a sub-sea gas release. Applied Ocean Research. 31, 220-225.

[9] Ghafarkhah, A., Shahrabi, M.A., Moraveji, M.K., Eslami, H., 2017. Application of CFD for designing conventional three phase oilfield separator. Egypt. J. Pet., 26 (2), 413-420.

[10] Ghafarkhah, A., Shahrabi, M.A., Moraveji, M.K., Eslami, H., 2018. 3D Computational-Fluid-Dynamics Modeling of Horizontal Three-Phase Separators: An Approach for Estimating the Optimal Dimensions. Oil and Gas. Fac., 33 (4), 1-17.

[11] Khalifat, Z., Zivdar, M., Rahimi, R., 1396. Simulation of three-phase separator in Borzoye petrochemical company, the first conference in science and engineering, Mashhad, in Persian.

[12] Kharoua, N., Khezzar, L., Saadawi, H., 2013b. CFD simulation of three-phase separator: effects of size distribution. ASME FEDSM. Nevada, USA.

[13] Kharoua, N., Khezzar, L., Saadawi, H., 2013a. CFD Modelling of a Horizontal Three-Phase Separator: A Population Balance Approach. Am. J. Fluid Dyn., 3 (4), 101-118.

[14] Kirveski, L., 2016. Design of Horizontal three-phase separator using computational fluid dynamics. MSC Dissertation, Alato university school of chemical technology.

[15] Mohammadi Ghaleni, M., Zivdar, M., Nemati, M.R., 2012. Hydrodynamic Analysis of two-phase separator by computational fluid dynamic (CFD). 6th international conference on Advanced Computational Engineering and Experimenting. Istanbul, Turkey.

[16] Monnery, W.D., Svrcek, W.Y., 1994. Successfully specify 3-phase separators. Chem. Eng. Prog, 90 (6), 29-40.

[17] Pourahmadi Laleh, A., 2010. CFD Simulation of Multiphase Separators. Ph.D. Dissertation, University of Calgary, Canada.

[18] Pourahmadi Laleh, A., Svrcek, W.Y., Monnery, W.D., 2011. Computational Fluid Dynamics Simulation of Pilot Plant-Scale Two-Phase Separators. Chem.Eng.Tech., 34 (2), 296-306.

[19] Pourahmadi Laleh, A., Svrcek, W.Y., Monnery, W.D., 2012. Computational Fluid Dynamics-Based Study of an Oilfield Separator--Part I: A Realistic Simulation. Oil and Gas Fac., 1(6), 57-68.

[20] Qarot, Y.F., Kharoua, N., Khezzar L., 2014. Discrete phase modeling of oil droplets in the gas compartment of a production separator. ASME International Mechanical Engineering Congress and Exhibition, Canada.

[21] Xu, Y., Liu, M., Tang, C., 2013. Three-dimensional CFD-VOF-DPM simulations of effects of low-holdup particles on single-nozzle bubbling behavior in gas-liquid-solid systems. Chem.Eng, 222, 292-306.

طراحی ساختار کنترلی و شبیه‌سازی دینامیک فرآیند مبرد آمیخته چند مرحله‌ای مایع‌سازی گاز طبیعی

- طلیعه رمضانی[۱]، زهرا نرگسی[۱]، علی پالیزدار[۱]، علی وطنی[۱*]

۱. انستیتو گاز طبیعی مایع (I-LNG)، دانشکده مهندسی شیمی، دانشکده فنی، دانشگاه تهران، تهران، ایران

(ایمیل نویسنده مسئول: avatani@ut.ac.ir)

چکیـــــــده

در این مقاله سامانه کنترلی فرآیند مبرد آمیخته چند مرحله‌ای مایع‌سازی گاز طبیعی طراحی شده و بررسی گردیده است. مصرف ویژه انرژی (SEC) این فرآیند برابر با ۰/۲۶۴۷ kWh/kg LNG می‌باشد. پس از شبیه‌سازی استاتیک (پایا) فرآیند مذکور و تعیین اندازه تجهیزات موجود در آن، به‌منظور کنترل کل فرآیند یک ساختار کنترلی طراحی گردید. علاوه بر این، شبیه‌سازی دینامیک (پویا) فرآیند انجام شد و عملکرد کنترلرها مورد بررسی قرار گرفت. با شبیه‌سازی دینامیک، مقدار مصرف ویژه انرژی فرآیند به ۰/۲۵۷۴ kWh/kg LNG کاهش یافت؛ که این موضوع نشان دهنده آن است که ساختار کنترلی طراحی شده می‌تواند فرآیند را به‌صورت پایدار و صحیح کنترل نماید. به‌منظور اعتبارسنجی عملکرد و پایداری ساختار کنترلی، تغییرات در دبی جریان و دمای خوراک گازی به‌عنوان اغتشاش به فرآیند وارد گردید.

واژگان کلیدی: گاز طبیعی مایع (LNG)، فرآیند MFC، کنترل فرآیند، شبیه‌سازی دینامیک

طلیعه رمضانی، زهرا نرگسی، علی پالیزدار: کارشناس ارشد تحقیق و توسعه (مهندس فرآیند)، انستیتو گاز طبیعی مایع (I-LNG)، دانشگاه تهران

علی وطنی: دکترای مهندسی شیمی، استاد دانشکده مهندسی شیمی، دانشگاه تهران

کاربرد مفهوم واحدهای جریانی هیدرولیکی برای محاسبه تراوایی در یکی از مخازن گازی ایران، مطالعه موردی

- اصغر گندم کار[1*]

۱. گروه مهندسی شیمی و نفت، دانشکده مهندسی شیمی و مواد، واحد شیراز، دانشگاه آزاد اسلامی، شیراز، ایران

(ایمیل نویسنده مسئول: agandomkar@shirazu.ac.ir)

چکیـــــــده

تخمین تراوایی در چاه‌های فاقد مغزه یکی از چالش‌های مهندسین مخازن است. در این مطالعه، از داده‌های آنالیز متداول مغزه به همراه داده‌های چاه پیمایی یکی از مخازن گازی جنوب غرب ایران به منظور تعیین مدل تراوایی با استفاده از مفهوم واحد جریان هیدرولیکی استفاده شده است. روش‌های آنالیز خوشه بندی شامل آنالیز هیستوگرام و نمودار احتمال نرمال جهت تعیین تعداد گروه‌های سنگی مورد استفاده قرار گرفت. همچنین، روش خطای حداقل مربعات جهت تعیین تعداد بهینه گروه‌های سنگی در نظر گرفته شده است. داده‌های تراوایی از طریق آنالیز چاه آزمایی، مغزه و چاه پیمایی به دست می‌آید. با این وجود استفاده از داده‌های چاه پیمایی از ارزان‌ترین روش‌ها است. اهمیت تراوایی سازند در تکمیل چاه، تحریک سازند و مدیریت مخزن تاثیر می‌گذارد. نتایج نشان می‌دهد که ۶ واحد جریان هیدرولیکی وجود دارد که هرکدام شاخص ناحیه جریانی مربوط به خود را دارد. علاوه براین، یک معادله تجربی بر اساس داده‌های مغزه و چاه پیمایی جهت تخمین تراوایی با دقت ۰/۶۰ ارایه گردید. همچنین، نمودار لرنز نشان می‌دهد که واحد جریانی ۳ و ۶ دارای تراوایی و تخلخل قابل توجهی هستند.

واژگان کلیدی: شاخص ناحیه جریانی، واحد های جریانی هیدرولیکی، مخازن گازی، آنالیز هیستوگرام، نمودار احتمال، خطای حداقل مربعات

نکات کلیدی در طراحی واحد جداسازی برودتی هوا برای ذوب آهن اصفهان

- فریدون علیخانی حصاری[1*]، عبدالله عبدالله[2]، امید چهره گشا[3]

۱. پژوهشگاه مواد و انرژی، صندوق پستی ۶۱۳/۷۸۷۱۳ کرج، ایران

۲. شرکت 3Acinegoyrc EZF، صندوق پستی ۱۷۲۲۴ شارجه، دبی

۳. دانشکده برق، دانشگاه شریف، صندوق پستی ۵۵۱۱۱-۵۶۳۱۱ تهران، ایران

(ایمیل نویسنده مسئول: f-a-hesari@merc.ac.ir)

چکیـــــــده

واحد جداسازی برودتی هوا جزء لاینفک بیشتر صنایع فولاد، شیشه، شیمیایی و پتروشیمی است که همواره مقدار متنابهی اکسیژن، ازت و ارگون مایع با خلوص بالا مورد نیاز است. برای صنایع، کیفیت (خلوص) اکسیژن، ازت و ارگون، هزینه تفکیک و مایع کردن اجزاء هوا و مصرف انرژی از عوامل تاثیرگذار بر انتخاب و طراحی واحدهای جداسازی برودتی هوا هستند. در این مقاله اثرگذاری این عوامل بر روی طراحی واحد جداسازی برودتی هوا مورد بررسی قرار گرفته است. طراحی موجود با در نظر گرفتن پیش نیازهای لازم برای یک واحد جداسازی برودتی هوا برای ذوب اهن اصفهان است. خلوص مورد نیاز اکسیژن، ازت و ارگون مایع از نکات کلیدی در طراحی است. کنترل مستعمر و موثر تغییرات فشار و درجه حرارت در برج تقطییر واحد جداسازی برودتی هوا برای ماندن در ناحیه تعادلی لازم بسیار مهم است. تولید سالانه ذوب اهن در حدود ۲/۵ میلیون است و در نظر است میزان تولید را به ۳/۲ میلیون تن در سال برسانند. در حال حاضر برای این میزان تولید در حدود ۳۰۰×۱۰^{۶} مترمکعب در سال اکسیژن مایع استفاده میکند و در حدود ۸۶×۱۰^{۶} متر مکعب در سال مازاد بر مقدار فعلی نیاز دارد.

واژگان کلیدی: جداسازی برودتی هوا، نکات طراحی، خلوص، شدت جریان

افزایش راندمان تولید سوخت مایع با استفاده از کاتالیست نانو آهن در فرآیند تبدیل گازطبیعی به مایع

- محمد ایرانی[1*] ،اصغر علیزاده داخل[2]، یحیی زمانی[1]

۱. پژوهشگاه صنعت نفت، تهران، ایران

۲. گروه شیمی و مهندسی شیمی، واحد رشت، دانشگاه آزاد اسلامی، رشت، ایران

(ایمیل نویسنده مسئول: iranim@ripi.ir)

چکیـــــــده

در این مقاله یک بررسی تجربی و مطالعه CFD با هدف افزایش تولید بنزین با استفاده از فرآیند فیشر- تروپش در یک رآکتور در مقیاس رومیزی (بنچ) انجام گرفت. یک رآکتور استوانه ای با یک منطقه پیش گرم کن و یک منطقه واکنش بکار گرفته شد. دمای رآکتور با استفاده از یک گرمکن کمربندی دور رآکتور، کنترل گردید. همچنین یک مدل CFD با تقارن ودر نظرگرفتن غیر ایده آلی مخلوط گازی با استفاده از معادله حالت پنگ - رابینسون ، توسعه داده شد. تعداد واکنشهای به کار گرفته شده برای این مدل ۲۳ مورد بود. مدل توسعه داده شده با اطلاعات تجربی اعتبارسنجی گردید. مدل تایید شده برای بررسی اثر شرایط عملیاتی روی کارکرد رآکتور استفاده شد. مقادیر بهینه شرایط عملیاتی شامل فشار ، دما، GHSV ونسبت خوراک برای کارکرد بهینه رآکتور بدست آمدند.

واژگان کلیدی: سنتز فیشر-تروپش، جی تی ال، رآکتور بستر ثابت، کاتالیست نانو آهن، سی اف دی

خواص نانوکامپوزیت‌های پلی‌کلروبوتیل/گرافن اکساید و نانوخاک‌رس از نظر برهمکنش‌های بین پرکننده‌ها

- مجید صفاجوجهانخانملو[1*]، مهدی اسکندرزاده[2]، جمال موثق[3]

۱. گروه مهندسی شیمی، دانشکده فنی و مهندسی، دانشگاه محقق اردبیلی، اردبیل، ایران

۲. گروه مهندسی مکانیک، دانشکده فنی و مهندسی، دانشگاه محقق اردبیلی، اردبیل، ایران

۳. مشاور تولید شرکت آرتاویل تایر، اردبیل، ایران

(ایمیل نویسنده مسئول: M.Safajou@uma.ac.ir)

چکیـــــــده

نانوکامپوزیت‌های نانو خاک‌رس اصلاح شده (Cloisite 15A) و گرافن اکساید با لاستیک کلروبوتیل و لاستیک طبیعی SMR20 با موفقیت تهیه شدند. اصلاح سطح نانوذرات باعث بهبود در پراکنش داخل ماتریس لاستیکی شده و خواص قطعه پخت شده مطابق با فرمولاسیون اینرلاینر بهبود قابل توجهی پیدا کرد. ورقه‌ورقه‌شدن ذرات گرافن اکساید و نانو خاک‌رس اصلاح شده توسط آنالیز پراکنش اشعه ایکس و میکروسکوپی الکترونی عبوری (TEM) اثبات گردید، اما در مورد کامپوزیت گرافیت، بین لایه‌ای شدن اتفاق افتاد. مطالعه خواص فیزیکی حاصل از این نانوذرات نشان داد کامپوزیت‌های حاوی نانوذرات اصلاح شده خواص بهبود یافته‌ای از خود نشان می‌دهند.

واژگان کلیدی: پلی‌کلروبوتیل، گرافیت، گرافن اکساید، خاک‌رس نانو و نانوکامپوزیت

کاربرد دینامیک سیالات محاسباتی به منظور عیب یابی و تحلیل رفتار هیدرودینامیکی در یک جداکننده گرانشی سه فازه صنعتی

- زهره خلیفات[1]، مرتضی زیودار[2*]، رهبر رحیمی[3]

۱. دانشجوی دکتری مهندسی شیمی، گروه مهندسی شیمی، دانشگاه سیستان و بلوچستان، زاهدان، ایران

۲. دانشیار گروه مهندسی شیمی، دانشگاه سیستان و بلوچستان، زاهدان، ایران

۳. استاد گروه مهندسی شیمی، دانشگاه سیستان و بلوچستان، زاهدان، ایران

(ایمیل نویسنده مسئول: mzivdar@eng.usb.ac.ir)

چکیـــــــده

جدایش جریان چند فازی در جداکننده های گرانشی یکی از فرایند های مهم در صنایع مختلف به شمار می رود. در این مطالعه از یک شبیه سازی دینامیک سیالات محاسباتی (CFD) با استفاده از یک مدل ترکیبی VOF-DPM برای عیب یابی و تحلیل رفتار هیدرودینامیکی فرایند جدایش در یک جداکننده سه فازی صنعتی دارای بوت، استفاده شده است. لازم به ذکر است که با وجود کاربرد گسترده جداکننده های بوت در صنایع مختلف تاکنون هیچ پژوهشی روی این نوع از جداسازها برای بررسی رفتار ماکروسکوپی و میکروسکوپی فرایند جدایش ارائه نشده است. در این پژوهش، نتایج محاسبات عددی بر حسب پروفایل های جریان سه فازی، رفتار فازهای ثانویه ، بازده جداکننده و توزیع اندازه قطرات مورد بررسی قرار گرفته است. نتایج نشان داد که مدل CFD مورد نظر قادر به تخمین خوبی از رفتار جدایش در یک جداکننده سه فاز دارای بوت است. عیب یابی فرایند جدایش در جداکننده مورد نظر برای تشخیص پارامترهایی که منجر به کاهش راندمان جداکننده می شود نیز مورد بررسی قرار گرفته است. نتایج نشان دهنده کاربرد نامناسب نوع هدایت کننده ورودی، نیاز به وجود نم گیر مناسب در خروجی گاز و همچنین نیاز به یک گرداب شکن در خروجی مایع بوده است. اثر افزایش میزان دبی آب ورودی روی عملکرد جداساز، یکی از پارامترهای مهم دیگری است که در این مطالعه مورد بررسی قرار گرفته است. نتایج نشان داد که افزایش دبی آب ورودی در محدوده kg/hr ۴۷۲۹۵-۱۱۸۲۳ منجر به افزایش میزان جرم آب در خروجی گاز از ۰/۰۹ به kg/hr ۱/۶ شده است ولی این مقدارافزایش باعث کاهش چشمگیری در عملکرد جدایش در جداساز مورد نظر نشده است.

واژگان کلیدی: جدا کننده گرانشی سه فازی، مدل حجم سیال ، مدل فاز ناپیوسته، عیب یابی، تحلیل هیدرودینامی

JOURNAL OF GAS TECHNOLOGY
VOLUME 5 • ISSUE 1 • SUMMER 2020
EISSN: 2588-5596

Contents